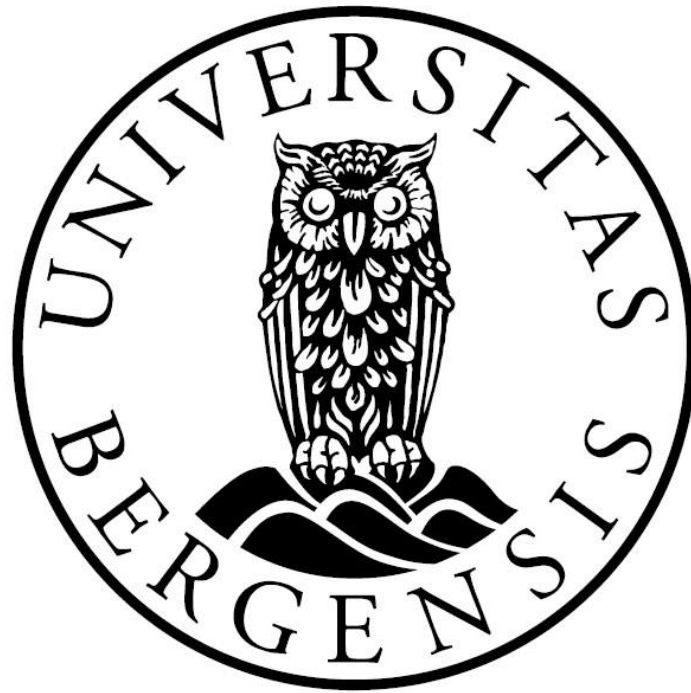# Experimental and Numerical Modeling Investigation of CO$_2$ Foam Mobility Control

Master Thesis in Reservoir Physics

By

Maren Soland

Department of Physics and Technology

University of Bergen

June 2021

Summary

CO_2 enhanced oil recovery (EOR) is widely recognized as an efficient technique to mobilize residual oil and can offset the costs of carbon capture and storage (CCS). However, due to severe viscosity and density differences between CO_2 and reservoir fluids, challenges such as gravity override, early gas breakthrough, viscous fingering, and reservoir heterogeneity can result in poor volumetric sweep efficiency and a limited recovery. The sweep efficiency and mobility ratio can be improved by foaming the CO_2 to effectively reduce its relative permeability and increase its viscosity.

CO_2 foam is a field tested technique to improve CO_2 sweep efficiency and stabilize the displacement front for increasing oil recovery and CO_2 storage potential. However, some field tests report difficulties with injectivity and attributing additional production specifically to CO_2 foam. Therefore, the foam formulations must be optimally designed and thoroughly evaluated in the laboratory and through numerical simulation for successful field design and interpretation.

This work is part of an international research program, led by the University of Bergen, which aims to optimize and field test CO_2 foam systems for CO_2 mobility control in EOR and CO_2 storage. The main objective for this thesis was to experimentally evaluate foam generation, strength, and stability of unsteady-state CO_2 foam in porous media at reservoir conditions to determine which injection rates, surfactant concentrations and gas fractions were suitable for generating strong and stable foam. A secondary objective was to design a laboratory methodology representative of the unsteady-state foam flow to assist in the interpretation of the field pilot test.

Foam was generated in all core-scale surfactant alternating gas (SAG) injections. Injections with a gas fraction of 0.60 and 0.70 generated strong and stable foam, suggesting that these gas fractions may be suitable for field testing. Surfactant concentrations of 2500 ppm and 5000 ppm had a negligible difference, suggesting a lower concentration can be used in the field, thus, improving the economic aspects of new pilot projects. The tested injection rates also gave negligible difference where both generated strong and stable foam. A laboratory methodology representative of unsteady-state flow was designed and utilized for core-flooding which allowed for analysis of unsteady-state foam flow.

Field-scale numerical modeling was also performed with the aim of evaluating foam generation, CO_2 foam mobility reduction, and sweep efficiency of different experimentally derived foam models. In addition, the effect of residual oil on foam was evaluated. Results showed that foam models with higher values for reference gas mobility-reduction factor (*fmmob*) generated stronger foam with a higher reduction of CO_2 mobility and an improved volumetric sweep. A higher reference oil saturation for foam collapse factor (*fmoil*) also resulted in stronger foam generation with a higher CO_2 mobility reduction and a better volumetric sweep.

Acknowledgements

Bergen, June 2021

Maren Soland

Table of Contents

Part I. Introduction and Theory

1. Introduction

Despite the need to dramatically reduce fossil fuel consumption in the coming years, it is still not possible to cut completely due to a constant demand for fuel and in industries with no other options (IEA, 2021b). Global energy demand in 2021 has already been estimated to surpass pre-Covid19 levels with an increase of 4.6% (IEA, 2021a). The total energy supply and demand in the next 20 years will increase by 30% worldwide, where emerging markets and developing economies will be a big part of the continuing increase (IEA, 2021b). Despite the change in consumption from fossil to renewable and clean energy there will still be CO_2 emissions that must be mitigated.

A known technology for mitigating industrial CO_2 emissions is carbon capture and storage (CCS). CCS involves capturing anthropogenic CO_2 and storing it permanently in a subsurface geological formation. CCS is considered a safe, long-term storage method and has been utilized since the 1970s (IPCC, 2005). Although CCS contributes to reduce CO_2 emissions, the process and technology is currently too expensive and not profitable. A possible solution for increasing the profit of CCS is to utilize the CO_2 before it is stored, in a process called carbon capture, utilization and storage (CCUS) (IPCC, 2005). CCUS involves capturing anthropogenic CO_2, transporting it by ship or pipeline, and injecting it into a subsurface reservoir for CO_2 enhanced oil recovery (EOR) and subsequent storage.

CO_2 EOR is a method used by the oil industry which has been widely recognized as an efficient EOR technique for over 50 years (Merchant, 2010). However, due to severe viscosity and density differences between CO_2 and the reservoir fluids, challenges such as gravity override, early gas breakthrough, viscous fingering, and reservoir heterogeneity can result in poor volumetric sweep efficiency and limited recovery (Dooley et al., 2010; Gozalpour et al., 2005; Kovscek & Radke, 1993). The sweep efficiency and mobility ratio can be improved by foaming the CO_2 to effectively reduce its relative permeability and increase its viscosity (Lee & Kam, 2013). Foam is capable of stabilizing the displacement front to increase oil recovery and CO_2 storage potential (Enick et al., 2012; Suffridge et al., 1989).

CO_2 foam is a field tested and proven technique to improve CO_2 sweep efficiency (Enick et al., 2012; Heller et al., 1985; Ocampo et al., 2013; Schramm & Wassmuth, 1994). However, some field tests report difficulties attributing additional production specifically to CO_2 foam (Chou et al., 1992; Martin et al., 1992; Martin et al., 1995; Stephenson et al., 1993). Therefore, the foam formulations must be optimally designed and evaluated in the laboratory and through numerical simulation for successful field implementation.

This work is part of an international research program, led by the University of Bergen, which aims to optimize and field test CO_2 foam systems for CO_2 mobility control in EOR and CO_2 storage. The main objective for this thesis was evaluating generation, strength, and stability of CO_2 foam experimentally in porous media at reservoir conditions to determine which injection rates, surfactant concentrations and gas fractions were suitable for generating strong and stable foam. A secondary objective was to design a laboratory methodology representative of the unsteady-state foam flow to assist in the interpretation of the field pilot test. Numerical work was also performed with the aim of testing CO_2 foam mobility reduction performance for generation and strength of experimentally derived foam models in a numerical reservoir simulation model. In addition, the effect of residual oil on foam was evaluated numerically.

2. Fundamentals of Reservoir Engineering

This chapter outlines the fundamental concepts of reservoir engineering essential for describing fluid flow in porous media central to this thesis.

2.1 Porosity

Porosity is defined as the volume of the void in a porous media, divided by the total bulk volume and expressed as a percentage of the mediums bulk volume.

$$\phi = \frac{V_p}{V_t} \cdot 100\%$$
2.1

Where V_p is the pore volume and V_t is the total bulk volume. It is called the total porosity and is the porosity value most logging methods measure (Lien, 2004).

The total porosity also includes pores which are not connected and therefore cannot contribute to the flow in reservoirs. When working with the actual contributing porosity, it is referred to the effective porosity which is the residual porosity subtracted from the total porosity (Jenkins, 1966).

$$\phi_{eff} = \phi_{tot} - \phi_{res}$$
2.2

Where ϕ_{tot} is the total porosity and ϕ_{res} is the residual porosity. The variation in porosity in different rock types is caused by the variation in grain type, shape and sorting (Lien, 2004).

2.2 Saturation

If the void space in a porous media is filled with multiple immiscible fluids, the volume can be expressed as the sum of the volumes of the individual fluids.

$$V_p = \sum_{i}^{n} V_i$$
2.3

Where V_p is the total pore volume and V_i is the volume of the fluid phase i. The saturation for each individual fluid, S_i, can be expressed as the volume of the individual fluid, V_i, divided by the total pore volume, V_p.

$$S_i = \frac{V_i}{V_p}$$
2.4

The relative saturation is the measured fraction of the total fluid saturation in a multiphase system, and always a value between 0 and 1.

2.3 Permeability, Relative Permeability and Wettability

Permeability is defined as the capacity of a porous media to transmit fluids through its interconnected pore network (Warner, 2015; Zolotuchin & Ursin, 2000). In ideal cases with a single incompressible fluid flowing, the permeability can be calculated with the empirically derived Darcy equation:

$$Q = \frac{K \cdot A}{\mu} \cdot \frac{\Delta p}{L}$$
2.5

Where Q is the volumetric flow, K is the absolute permeability, A is the cross-sectional area, μ is the viscosity of the fluid, Δp is the differential pressure across the media and L is the length of the media (Hubbert, 1956; Lien, 2004).

If the porous media contains two or more immiscible fluids, the flow is affected by the distribution of each of the fluids, the wettability, and the saturation history. In these cases, the relative permeability is required to be measured and calculated for the individual fluid phases to determine the system's ability to conduct multiple fluids simultaneously (Anderson, 1987b; Warner, 2015). The relative permeability, K_{ri}, is defined as the effective permeability, K_i, for each individual fluid, divided by the absolute permeability, K. The relative permeability is always lower than the absolute permeability due to the individual fluid phase only occupying a fraction of the total pore volume (Warner, 2015; Zolotuchin & Ursin, 2000).

$$K_{ri} = \frac{K_i}{K} \qquad\qquad 2.6$$

The relative permeability is a function of the fluid mobility at a given saturation. Essentially, the relative permeability increases for a fluid when the saturation of that fluid is increased (Anderson, 1987b). As can be seen in Figure 2.1, the relative permeability is also highly dependent on the wettability of the system where graph (a) is a water wet system, and graph (b) is an oil wet system.
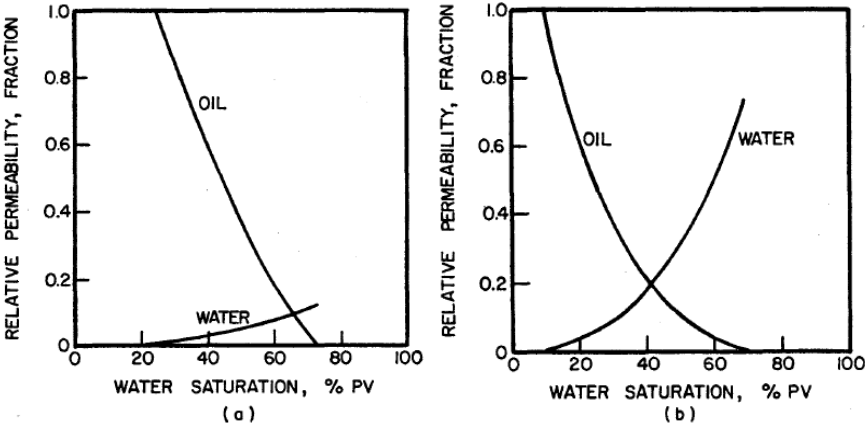
Figure 2.1 Relative permeability curves for a strongly water wet (a) and a strongly oil wet (b) system plotted against increasing water saturation (Craig, 1971).

Wettability is the tendency of a single fluid in the presence of another immiscible fluid to spread over a solid surface. If two immiscible fluids are near a solid surface, the cohesive force for one of the fluids will be stronger than the other and is thereby the wetting fluid phase of the two. For a brine/oil/rock system, the rock is the deciding factor for the wettability where it either has a preference to water or oil. If the rock is water-wet, the water will fill the smaller pores and flow along the pore walls, and the oil will occupy the center of the bigger pores. For an oil-wet system, the location of the fluids will be reversed (Anderson, 1986a). Figure 2.1 illustrates the relative permeability with increasing water saturation for the oil and water phase in a water-wet and an oil-wet system. It can be seen that the non-wetting phase has a higher relative permeability compared to the wetting phase due to its location in the pore system (Anderson, 1987b). Wettability also has a substantial influence on capillary pressure, electrical properties, waterflood behavior and residual saturation after tertiary recovery (Anderson, 1986a).

2.4 Capillary Pressure

Capillary pressure (P_c) is the pressure difference between two immiscible fluids obtained from the interfacial tension (IFT) between the fluid surfaces (Anderson, 1987b). Capillary pressure is defined as:

$$P_c = p_{nw} - p_w \qquad\qquad 2.7$$

6

Where p_{nw} is the pressure of the non-wetting fluid and p_w is the pressure of the wetting fluid. When the pressure of the non-wetting fluid is increased, the capillary pressure rises accordingly. This process is called drainage and the non-wetting fluid displaces the wetting fluid. The reversed process is called imbibition, the pressure of the wetting phase is then increased to a level where the wetting phase can displace the non-wetting phase (Anderson, 1987a).

On a microscopic pore-scale, the capillary pressure can be expressed as a relationship between the interfacial tension, fluid angle and the radius of the pore.

$$P_c = \frac{2 \cdot \sigma \cdot cos\theta}{r} \qquad 2.8$$

Where σ is the interfacial tension (IFT), θ is the angle between wetting and non-wetting fluid and r is the radius of the pore (Anderson, 1986b). By lowering the interfacial tension or increasing the pore radius, the capillary pressure will decrease. Wettability will also have an impact on the capillary pressure, depending on the fluids present and the fluid preference in the system (Anderson, 1987a).

2.5 Stages of Oil Recovery

Oil recovery can in general be divided into three stages: primary, secondary, and tertiary recovery. Primary recovery is the recovery solely based on the natural energy drive initially in the reservoir. This includes fluid and rock expansion, solution gas, gas cap, water drive and gravity drainage (Romero-Zerón, 2012; Sheng, 2010). Secondary recovery involves introducing sources of artificial energy into the system like injection of water and/or gas in the reservoir. Those recovery processes are usually immiscible with the reservoir oil. The goal is to maintain the pressure in the system and displace oil towards the production well (Romero-Zerón, 2012). Primary and secondary recovery combined produce on average 25 to 35 % of the original oil in place (OOIP) in the reservoir (Zekri & Jerbi, 2002). The reason for the low recovery during the conventional production stages, is pressure loss in the reservoir during primary production, and low volumetric sweep efficiency and high fraction of water in the production during secondary production. The unfavorable mobility ratio between the injected fluids and the reservoir oil is also a part of the problem (Alagorni et al., 2015; Zolotuchin & Ursin, 2000). When secondary recovery is no longer economical, the recovery can be improved by initiating enhanced oil recovery (EOR) or tertiary recovery (Alagorni et al., 2015).

EOR is the production process where fluids and energy originally not present in the reservoir are introduced and injected. They are implemented to increase the production of hydrocarbons from mature fields after conventional recovery has been performed (Romero-Zerón, 2012). EOR technology has played a central role in hydrocarbon production due to fewer discoveries of new fields, continuing maturation of currently producing oil fields and an ever-increasing demand for energy globally (Aladasani & Bai, 2010).

The primary objective of EOR techniques is to improve the overall efficiency of oil displacement by increasing the macroscopic and microscopic displacement efficiency (Romero-Zerón, 2012). Macroscopic displacement efficiency expresses the effectiveness of the volumetric sweep by the displacing phase and the capability of the fluid to move the displaced oil to the production well. While the microscopic efficiency, describes the mobilization of the reservoir oil at pore scale. When reducing the capillary forces, one improves the interfacial tension (IFT) between the displacing fluids and the oil, as well as the viscosity ratio between them. The alteration reduces the volume of residual oil and improves the microscopic recovery efficiency. Generating a favorable ratio for the mobility of the displacing fluids and the oil, also improves the sweep efficiency and the macroscopic displacement (Green & Willhite, 1998; Satter, 2008).

EOR methods are typically divided into groups: solvent, thermal, and chemical processes. For solvent processes, the objective is to inject gas to get a transfer of mass between the injected fluid and the reservoir oil to develop miscibility. Different gasses can be used for this type of injection, but CO_2 is the most common. The main functions of mass transfer are extraction, vaporization, dissolution, condensation and solubilization which all contributes to developing miscibility between the reservoir oil and solvent. Thermal methods are the supplement of thermal energy though steamdrive or steam soak injections to reduce the viscosity of the reservoir oil and raise the efficiency of the overall displacement (Lake et al., 2014). Chemical EOR is injection of chemicals like surfactants, polymers or alkaline to change the composition and behavior of the reservoir and injection fluids. Surfactant flooding reduce the interfacial tension (IFT) and improve the microscopic displacement efficiency through mobilizing residual oil. Polymer injections increase water viscosity and decrease the water-oil mobility ratio. Alkaline flooding is injection of alkaline agents to produce in situ surfactants. The effect will therefore be the same as for surfactant flooding (Abidin et al., 2012; Ragab & Mansour, 2021). The methods mentioned are usually implemented and combined to serve specific reservoirs and their needs. In this thesis, miscible CO_2 flooding with mobility control trough CO_2 EOR foam has been tested.

3. CO$_2$ for Enhanced Oil Recovery

For over 60 years, the injection of CO$_2$ for enhanced oil recovery (EOR) has been performed with commercial success. Due to the low cost and availability of CO$_2$, CO$_2$ flooding in onshore U.S. oil fields is especially widespread, where CO$_2$ EOR contributes approximately 5% of the domestic production of crude oil. Because of the dense, supercritical state at typical reservoir conditions, CO$_2$ can compress and achieve miscibility with most reservoir crude oils, thus it is a preferred choice for gas injection for EOR purposes (Enick et al., 2012; Lee & Kam, 2013). This chapter includes descriptions of the physical properties of CO$_2$, the mechanisms behind miscible displacement of oil, and the issues regarding gas flooding which results in a poor macroscopic sweep efficiency.

3.1 Physical Properties of CO$_2$

It is essential to recognize the physical properties of CO$_2$ at different pressure and temperature regimes to successfully utilize CO$_2$ for EOR projects. At ambient conditions, CO$_2$ remains a gas, but as pressure increases, the gas will compress and condensate into a liquid (Figure 3.1). Furthermore, if the temperature increases beyond the critical point of 31.1°C and 73.9 bar, the liquid will become supercritical (Freund, 2005). At typical reservoir conditions with high temperature and pressure, the supercritical carbon dioxide will both have a higher viscosity and density compared to other gasses. Both of which have more beneficial properties when displacing reservoir oil compared to injecting pure gas (Holm & Josendal, 1974; Lee & Kam, 2013).
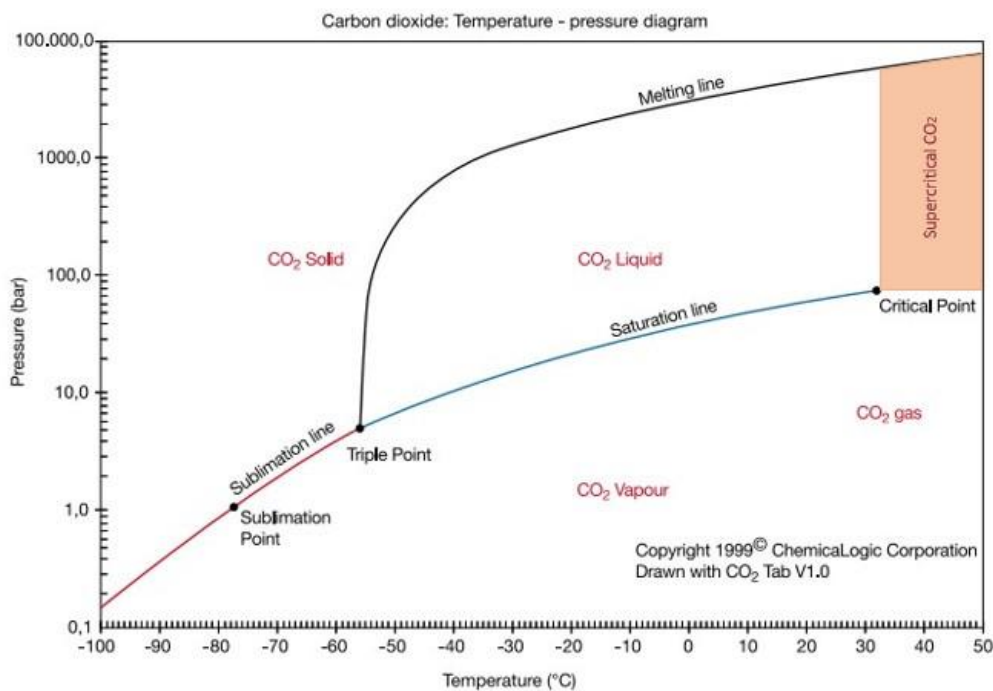
Figure 3.1 CO$_2$ phase diagram. CO$_2$ compressed to supercritical fluid above Pressure = 73.9 bar and Temperature = 31.1°C. Figure modified from (Freund, 2005).

3.2 Miscibility

In most CO$_2$ EOR projects, CO$_2$ achieves miscibility with the reservoir oil resulting in increased oil displacement (Holm & Josendal, 1974; Metcalfe & Yarborough, 1979). Miscibility can be defined as the physical condition at which two or more fluids form a single, homogenous phase when mixed in all proportions without an interface between them. If the fluids separate into phases spontaneously or when the concentration of one of the fluids is increased, they are immiscible. The interfacial tension (IFT) is above zero for immiscible fluid mixes and an interface exists between the phases

9

(Holm, 1986). Instabilities in a miscible displacement front results in a substantial amount of residual reservoir oil left behind in unswept areas due to water blocking, viscous fingers, and local heterogeneities in the reservoir (Muller & Lake, 1991). Thus, the performance of conventional CO_2 EOR projects may suffer. Despite this, CO_2 EOR may accomplish approximately a 5 to 20% increase in recovered oil compared to conventional recovery (Enick et al., 2012).

There are two different types of miscible displacements: first- and multi-contact miscible displacement. First-contact miscibility is accomplished if any measure of solvent phase can be added to the reservoir oil, and they will form one single phase. Most hydrocarbons with low molecular weight like liquefied petroleum gas (LPG), propane or butane can be injected as first-contact miscible solvents, but they are not a beneficial solution economically due to their high costs (Al-Wahaibi & Grattoni, 2008; Holm, 1986). The mechanism of multi-contact miscibility is achieved by vaporization- and condensing-gas drive, both of which require transmission of hydrocarbon components between the displacing and the displaced fluid (Holm, 1986; Metcalfe & Yarborough, 1979). Throughout CO_2 injection, the CO_2 achieves miscibility during vaporizing-gas drive. Intermediate components in the reservoir oil are vaporized over in the gas which results in miscibility between the enriched gas and the reservoir oil. In comparison to injections of other lean gases, supercritical CO_2 obtains miscibility at lower pressures by deriving heavier hydrocarbons from the reservoir oil (Holm, 1986; Rathmell et al., 1971).

3.3 Minimum Miscibility Pressure (MMP)

For two immiscible fluids in a displacement process to obtain miscibility, the pressure must exceed a pressure minimum known as minimum miscibility pressure (MMP). The minimum pressure is dependent on the temperature and compositions in the reservoir as well as the properties of the injected gas, and it must be determined experimentally (Yellig & Metcalfe, 1980). A common method to determine MMP, is through slim tube experiments. For those experiments, a thin tube filled with oil and unconsolidated sand and gas is injected to measure the pressure during displacement. As can be seen in Figure 3.2, MMP is determined by plotting the experimentally measured recovery against pressure, where the shape of the graph forms a plateau when miscibility is achieved (Skarestad & Skauge, 2012; Yellig & Metcalfe, 1980).
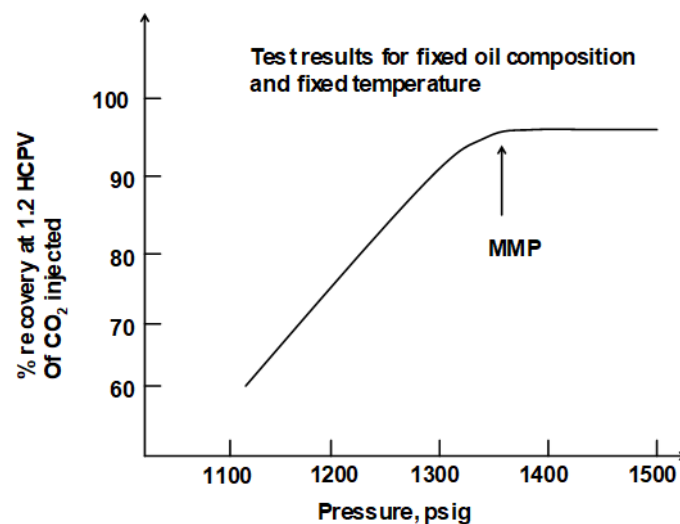

Figure 3.2 Graphical illustration of the determination of minimum miscibility pressure (MMP) in a slim tube experiment. MMP is characterized by the flattening of the curve (Skarestad & Skauge, 2012).

3.4 Diffusion and Dispersion

For miscible floods where CO_2 displaces oil, the phenomenon of dispersion must be considered. As a combined result of diffusion, mechanical mixing in pores and local velocity gradients, dispersion develops a mixing zone between the oil in the reservoir and the injected CO_2 (Skarestad & Skauge, 2012). During a recovery process with a miscible zone, there is a risk of losing miscibility though dissipating the miscible fluid or though channeling of viscous fingers in the miscible zone. Dispersion and diffusion are the mechanisms that generate the miscible flooding zone, but dispersion can also be the cause for generation of viscous fingers through damping-out phases from the mix. It is therefore important to know of these operations and their influence on the miscible flow to optimize the oil recovery (Perkins & Johnston, 1963).

The process of diffusion occurs when two miscible fluids with an interface at initial contact spontaneously mix and diffuse together. After some time, the sharp interface has become a mixing zone grading from one pure fluid over to the other (Perkins & Johnston, 1963). Molecular diffusion is the transport of molecules from areas with a high concentration to areas with a lower concentration in miscible fluid mixes and is continued until a state of equilibrium is achieved. This process can take place in gases, liquids and dense phases (Skjæveland & Kleppe, 1992). Another function of diffusion is the contribution to swelling of immobile oil in dead-end pores (illustrated in Figure 3.3) by diffusing gas through the blocking water and supplement the total recovery of hydrocarbons (Mirazimi et al., 2017).

Dispersion combines the effects of both diffusion and convection-induced mixing and causes reduction of the concentration gradients as CO_2 flows through the porous media. Factors such as density and viscosity variations, heterogeneity of the porous media as well as turbulence can all affect the dispersion (Perkins & Johnston, 1963). In general, dispersion is sorted after scale: microscopic pore scale, macroscopic core scale and megascopic field scale. The mechanisms for each scale differ. For the microscopic scale, molecular diffusion and single-pore flow dominates, while large-scale heterogeneities like high-permeability channels and stratification are central in the mixing at macro- and megascopic scale. For laboratory core scale experiments, the mixing mechanisms observed can be variations of all the mixing mechanisms, but for homogenous media the dominating mechanism is likely to be as those for microscopic systems such as single-pore flow and molecular diffusion (Skjæveland & Kleppe, 1992).

3.5 Oil Swelling

In a miscible CO_2/oil displacement, the injected CO_2 mixes and dissolves into the reservoir oil. This process of dissolution of CO_2 into the crude oil causes reduction in viscosity and swelling of the oil. As a result, the combined effect of swelling and pressure surge improves the flowing properties which gives an enhanced production (Lee & Kam, 2013; Yellig & Metcalfe, 1980). Influences such as temperature, pressure and oil composition influence the degree of oil swelling. The swelling factor and solubility of CO_2 increases with increasing pressure and decreases at high temperatures above the critical point (Mangalsingh & Jagai, 1996). The swelling of oil is a product of the solubility of CO_2 in crude oil. While dissolving into the oil, the CO_2 also displaces amounts of methane from the expanding oil. Due to it not being able to remove all the methane completely, the swelling depends on the amount of methane still in the oil. Higher amounts of residual methane will result in a poorer oil swelling efficiency (Mangalsingh & Jagai, 1996; Skjæveland & Kleppe, 1992).

The injection strategy also influences the effect of oil swelling. CO_2 is usually injected during tertiary displacement, after a secondary recovery waterflooding. At this point, the water saturation is high which blocks direct contact between the injected CO_2 and reservoir oil. This event is called water shielding and contributes to reducing the oil swelling and preventing miscibility between the phases,

which again affects the oil recovery (Grogan & Pinczewski, 1987; Stalkup, 1970). Experiments conducted by Campbell and Orr (Figure 3.3) demonstrated that given enough time, the CO_2 can diffuse through blocking water phase and swell trapped oil in a "dead end" pore, which with sufficient swelling will mobilize it and improve the oil recovery. Even though diffusing though blocking water is possible, the swelling is more effective and the production of oil is higher when CO_2 is injected during secondary displacement when the water saturation is lower (Campbell & Orr, 1985; Grogan & Pinczewski, 1987).
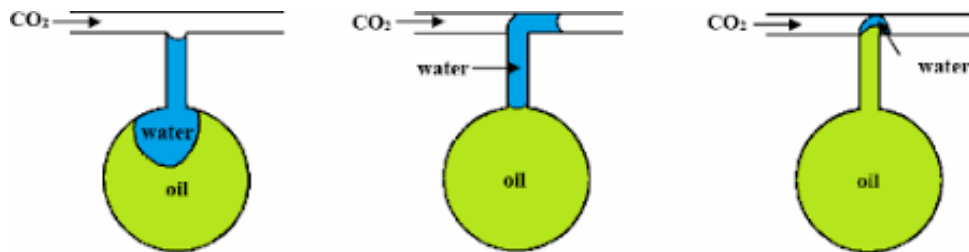
Figure 3.3 Oil swelling due to diffusion of CO_2 through blocking water in a dead-end pore. Modified from (Campbell & Orr, 1985).

3.6 CO_2 Injection Challenges

The microscopic sweep efficiency of CO_2 in EOR processes is generally high compared to its macroscopic sweep efficiency. High microscopic sweep is related to the swelling and mobilizing of trapped oil, but due to the unfavorable mobility ratio between the injected CO_2 and in-situ oil and reservoir heterogeneity, the macroscopic sweep efficiency can be poor for the field. Figure 3.4 illustrates the instabilities in the displacing front resulting in poor macroscopic sweep efficiency. Gravity override, viscous fingering and early gas breakthrough are direct consequences of the mobility ratio and they all contribute to lower oil recovery and a poor volumetric sweep (Kovscek & Radke, 1993; Mo et al., 2012). The density and viscosity of the injected CO_2 is much lower than of the reservoir oil, even at a supercritical state. Thus, the displacement front divides into fingers and channels that bypasses the reservoir oil and causes early gas breakthrough in the production well. Gravity override is also caused by the low density of gas which results in stronger buoyant forces for the gas. The buoyancy pulls the gas to the top of the reservoir thereby minimizing the volumetric sweep (Lee & Kam, 2013; Stone, 1982). The poor mobility relationship can be improved by foaming the CO_2 which gives more favorable properties to the front and improves the oil recovery (Enick et al., 2012).
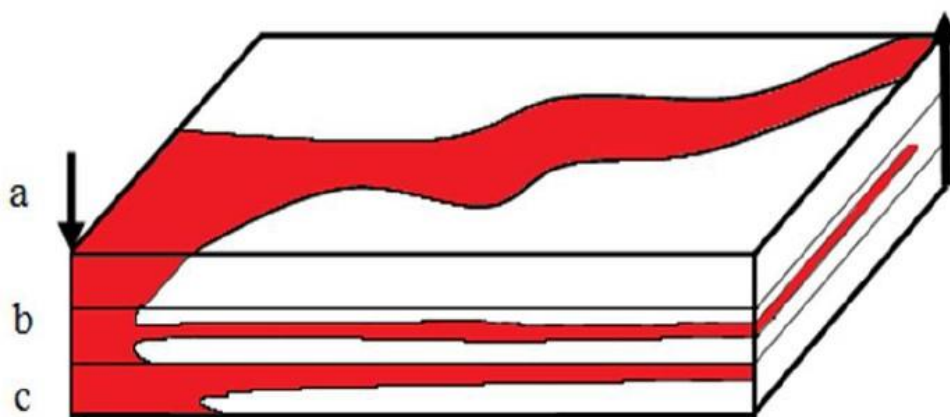
Figure 3.4 CO_2 flow in a reservoir, red represents the injected CO_2 and white is the reservoir matrix. Disadvantages with CO_2 flooding: (a) poor sweep efficiency, (b) gas channeling/viscous fingers, and (c) gravity override (J.E. Hanssen et al., 1994).

4. CO$_2$ Foam Mobility Control

This chapter presents the fundamentals for CO$_2$ foam mobility control.

4.1 Foam Characteristics

Foams are defined as agglomerations of gas bubbles separated by thin liquid films (Bikerman, 1973). For CO$_2$ EOR flooding, it effectively increases the CO$_2$ viscosity and reduce viscous fingering which leads to a reduced mobility ratio and an improved macroscopic sweep efficiency (Figure 4.1) (Chou, 1991; Gauglitz et al., 2002). In figure 4.1, the reservoir area to the left of the production well shows free-gas injection and an unfavorable mobility ratio between the displacing and displaced fluids, whereas the reservoir area to the right of the production well illustrates a foam stabilized displacing front with an improved mobility ratio.
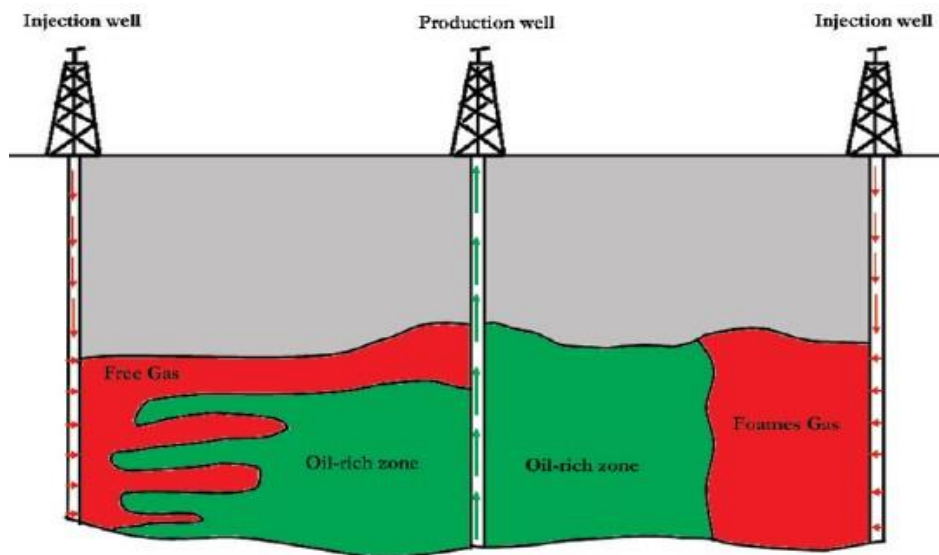
Figure 4.1 – Flooding of free gas (left) and flooding of foam (right). Modified from (Farajzadeh et al., 2010).

Foam is highly unstable and will collapse over time, therefore the liquid phase must be stabilized by a foaming agent. Surfactants are common foaming agents used to stabilize foam (Heller & Kuntamukkula, 1987; Kovscek & Radke, 1993). Foaming agents reduce the interfacial tension between the fluids and increase the interfacial viscosity of the lamellae to improve the mechanical resistance to thinning, bubble coalescence and rupturing of foam structure (Schramm & Wassmuth, 1994). Figure 4.2 illustrates a two-dimensional foam system. The gas phase is separated by lamellae which are thin, continuous liquid films. When three lamellae are connected at an angle, is called a Plateau border (Schramm & Wassmuth, 1994).
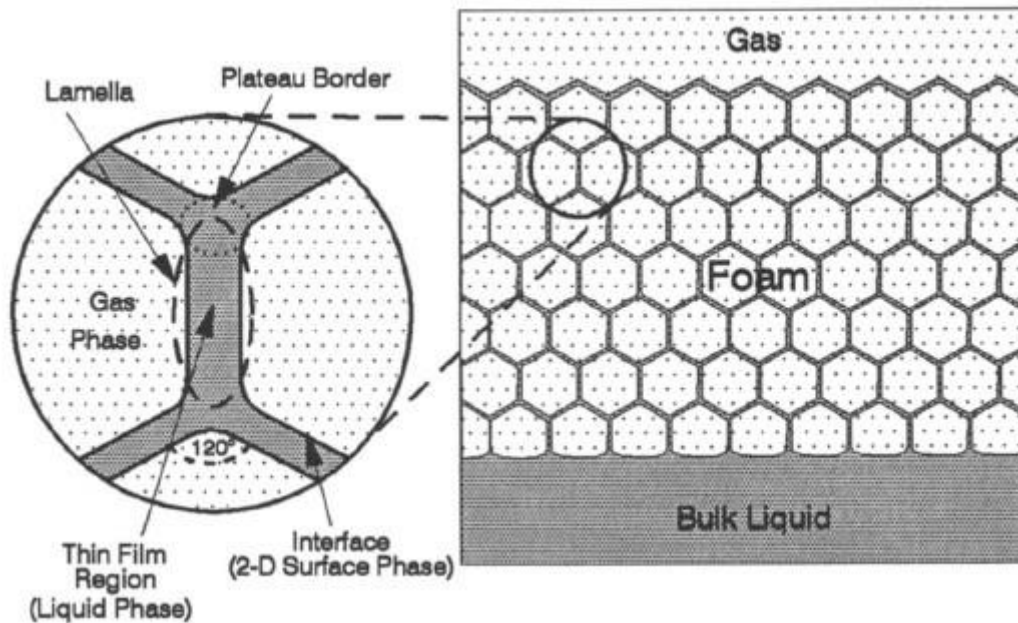
Figure 4.2 Generalized illustration of a two-dimensional intersection of a foam system (Schramm & Wassmuth, 1994).

Due to the thermodynamic instability of foam, lamellae generate and collapse constantly. The stability of foam in a flooding process is its ability to resist breakdown of bubbles due to coalescence or bubble collapse and is dependent on various factors such as temperature, pressure, and the presence of oil. In general, the strength of the foam improves with increased foam texture (bubble size, shape, and distribution within the foam matrix) (Chambers, 1994; Wasan et al., 1994). The foam stability in a porous media is also dependent on the reservoir properties such as the permeability, saturation of fluids and the properties of the foam lamella (Farajzadeh et al., 2012).

4.1.1 Effect of Permeability

The permeability of the porous media influences the strength and stability of the foam due to its relation to the pressure gradient. A minimum pressure gradient is required for generation of a fine-textured, strong foam. Increasing permeability gives a decreasing pressure gradient which again produces stronger and more stable foams. High-permeable zones are the ideal place for foam to generate (Gauglitz et al., 2002). Due to the heterogeneity in most reservoirs, foam flows into high-permeable zones which can result in pore blockage. The flow will therefore be diverted to zones with lower permeability, and it will enhance the oil recovery and sweep areas which previously have not been contacted (Farajzadeh et al., 2012; Veeningen et al., 1997).

4.1.2 Effect of Temperature and Pressure

The high pressure and temperature usually present in the reservoirs significantly influence the stability of foam. It is therefore important to understand how the foam performs in different environments. By increasing the temperature, the solubility of the surfactant in the liquid phase is increased which leads to less surfactant in the gas-liquid interface. Higher temperatures also increase liquid drainage, which also destabilizes the foam (Sheng, 2013; Wasan et al., 1994). By increasing the pressure in the system, however, the gas bubbles will compress, the liquid films will cover more due to the compression, and the liquid drainage slows down which all are factors that improve the stability of foam. Up until the pressure limit of a maximum system-specific value (limiting capillary pressure), the high pressure keeps stabilizing the foam. By exceeding this value, the bubbles will be prone to high stress which results in foam decay (Sheng, 2013).

4.1.3 Effect of Oil

It is vital to consider the interactions between the reservoir oil and the foam. The reservoir oil in contact with foam can spontaneously spread over the foam film and displace the original liquid in place with unstable oil film, which destabilizes the foam and coalesces the foam bubbles (Ross & McBain, 1944; Wasan et al., 1994). The liquid phase in the foam can emulsify spontaneously with the oil, resulting in depletion of the gas-liquid interface (Schramm, 1994). In addition, components from the reservoir oil may adsorb on the porous surface and alter the wettability making it harder for the foam to generate and regenerate. A saturation of oil in the reservoir higher than a system specific level has also been seen to contribute to a lower efficiency of foam generation (Friedmann & Jensen, 1986; Schramm, 1994).

When evaluating foam performance for CO_2 mobility control, estimation of different properties and mathematical relations can help quantify the effect of the flooding(Chang & Grigg, 1999). Parameters such as gas fraction, apparent viscosity and the mobility reduction factor are important parameters affecting the foam flow behavior.

4.1.4 Gas Fraction/Foam Quality

Gas fraction, or foam quality, is of high importance due to its direct relationship to foam strength. The gas fraction provides information on the transition from a low-quality foam to a high-quality foam regime. Gas fraction refers to the fraction of injected gas relative to the total liquid and gas injected and is defined as:

$$f_g = \frac{q_g}{q_g + q_{liq}} \qquad\qquad 4.1$$

Where q_g is the gas rate and q_{liq} is the flow rate for the liquid (Farajzadeh et al., 2012). The quality usually ranges from 75 to 90% and is essentially an expression of the fraction of gas in the foam (Farajzadeh et al., 2012; Sheng, 2013). By increasing the fraction of gas, the mobility will decrease up until the critical foam quality. By exceeding this limit of stability for the gas fraction, the mobility will no longer be effectively reduced and the foam will lose its stability (Chambers, 1994; Derikvand & Riazi, 2016). A foam quality scan can be conducted to determine the foam fraction at which this transition occurs. The scan is conducted by co-injecting gas and surfactant solution at steady state and testing different gas fractions (Kahrobaei et al., 2017).

4.1.5 Apparent Viscosity

The unfavorable mobility ratio of CO_2 to oil is a consequence of the low viscosity of the CO_2. The mobility ratio can be improved by increasing the effective viscosity of the CO_2 and thereby increasing the efficiency of the displacement process (Hirasaki & Lawson, 1985; Svorstøl et al., 1996). Foam apparent viscosity describes gas mobility reduction during foam flow and is used as an indicator for foam strength where a higher apparent viscosity represents stronger foams (Hirasaki & Lawson, 1985). The apparent viscosity of foam can be described by using Darcy's law:

$$\mu_{app} = \frac{K \cdot A \cdot \Delta P}{q_g \cdot L} \qquad\qquad 4.2$$

Where K is the absolute permeability of the porous media, A is the cross-sectional area, ΔP is the pressure gradient, q_g is the volumetric flow rate of the gas and L is the length (Svorstøl et al., 1996).

Mobility reduction factor (MRF) is a measure of the effectiveness of foam to reduce the apparent viscosity of pure gas. It is defined as the ratio between the apparent viscosity of foam and pure gas (Rosman & Kam, 2009; Svorstøl et al., 1996):

$$MRF = \frac{\mu_{app}(CO_2\ foam)}{\mu_{app}(CO_2)} \qquad\qquad 4.3$$

Where μ_{app} is the calculated apparent viscosity for foam and gas from Equation 4.2. An MRF value equal to 1 indicates that the viscosity for foam and gas are the exact same and the foam achieved no reduction in gas mobility. Higher values of MRF indicates stronger and more finely textured foams (Rosman & Kam, 2009).

4.2 Foam Generation

CO_2 foam is generated in a porous media either by injecting alternating slugs of gas and surfactant solution (surfactant-alternating gas) or by continuous co-injection of gas and surfactant solution (Farajzadeh et al., 2012). When surfactant and gas flows through the porous media, rapid shear strain occurs that leads to generation and stretching of bubbles in the pores. Throughout the life of the foam, lamellae form and collapse constantly. The rate of generation is proportional to the injection rate and depends on complexity and size of the pores (Heller, 1994). Mechanisms of foam generation determines the texture (bubble size and size distribution) of the foam, which affects both the apparent viscosity and flow properties of the foam. Understanding the foam generation mechanisms is important for predictions of the foam efficiency (Farajzadeh et al., 2012; Ransohoff & Radke, 1988). The main mechanisms for foam generation in a porous media are leave-behind, snap-off and lamella division (Figures 4.3-4.5) (Ransohoff & Radke, 1988).

Leave-behind (Figure 4.3) creates a lamella in the liquid filled pore throat between two neighboring pore bodies when gas enters from separate directions (Rossen, 1996). It does not generate separate bubbles, but a continuous gas flow path is established. When this process occurs on a frequent basis, large number of lamellae are generated and they block the gas pathway, thereby decreasing the relative permeability of the gas (Ransohoff & Radke, 1988).
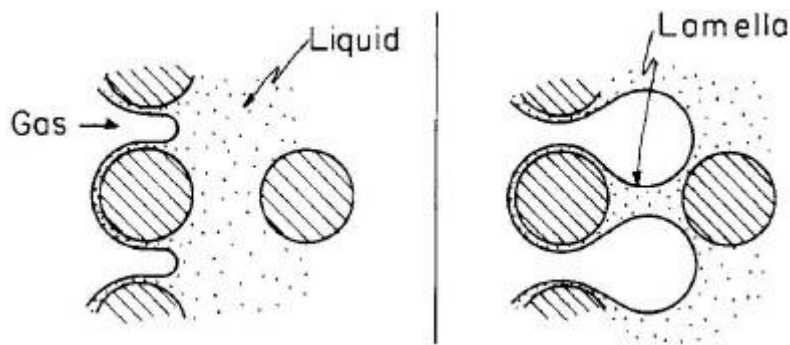
Figure 4.3 Leave-behind mechanism in a porous system (Ransohoff & Radke, 1988).

Snap-off (Figure 4.4) is significant in the generation of bubbles and occurs during multiphase flow regardless of the presence of foaming agents. The process involves gas fingers entering a fluid-saturated pore through a narrow pore throat. Due to the capillary pressure decrease in the downstream body of the pore, the liquid accumulates in the pore throat which separates the gas from the continuous phase (Kovscek & Radke, 1993). The snap-off mechanism is the primary source for forming strong foam due to the higher resistance in fine textured foams than in a continuous phase foam (Ransohoff & Radke, 1988).
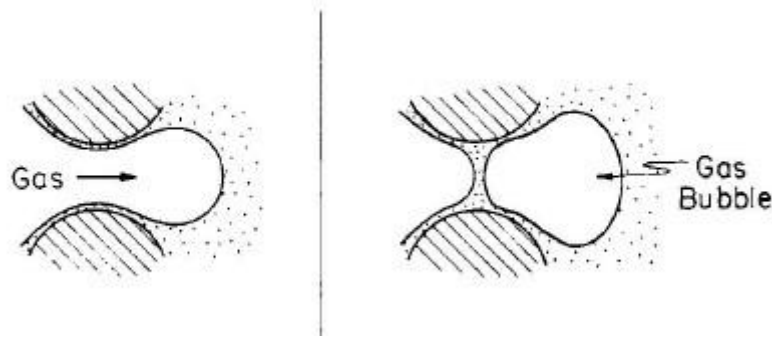
Figure 4.4 Snap-off mechanism in a porous system (Ransohoff & Radke, 1988).

Lamella division (Figure 4.5) occurs when a flow path splits into two and an existing bubble is split between the two paths and creates new lamellae without breaking (Falls et al., 1988; Rossen, 1996). This type of division only occurs if the bubble is larger than the pore body and it is a secondary foam generation mechanism due to the requirement for pre-existing lamellae. Lamella division also contributes to the production of strong foam by splitting the bubbles (Kovscek & Radke, 1993).
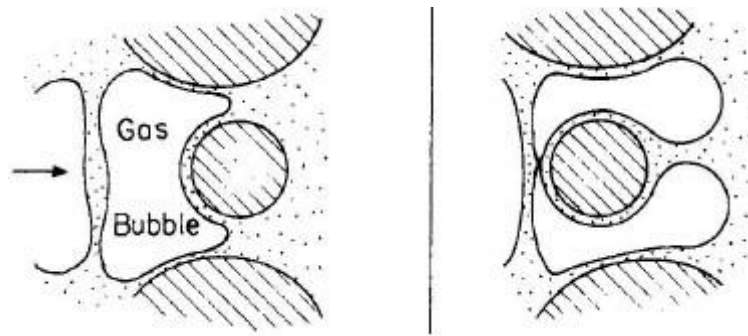
Figure 4.5 Lamella division mechanism in a porous system (Ransohoff & Radke, 1988).

Generation of foam also depends on the injection velocity, surfactant concentration and pressure gradient. It has been demonstrated that a minimum pressure gradient and injection velocity must be surpassed to generate foam, but the exact value depends on the gas fraction and system length. Generally, the minimum velocity of gas needed for foam generation increases with increasing quality of foam, and decreases with higher surfactant concentrations (Chou, 1991; Rossen, 1996).

4.3 Foaming Agent - Surfactants

Foam is highly unstable and easily breaks due to its thermodynamic instability. A foaming agent is typically used for stabilization of the foam (Sheng, 2013). For a field scale application, the foaming agent needs to be effective at a low cost, chemically stable and unaffected by contact with reservoir minerals or crude oil (Dellinger et al., 1984). Surfactants can be utilized with relatively low production costs and are therefore of high interest in CO_2 EOR (Enick et al., 2012; Zolotuchin & Ursin, 2000).

Surfactants, or surface-active agents, are injected to reduce the interfacial tension (IFT) between the injected phase and the crude oil in the reservoir and to generate and stabilize foam (Lake et al., 2014; Sheng, 2013). A single surfactant consists of a hydrophilic and a hydrophobic part which allows for the reduction of the IFT between immiscible fluids. The different polar-group identities of surfactants split them into four groups: Anionic, cationic, nonionic, and amphoteric. When dissolved in water, the anionic surfactant has a negative charge, cationic has a positive charge, nonionic has no charge and an amphoteric surfactant has both a positive and a negative charge (Heller et al., 1985; Lake et al., 2014). Anionic surfactants are both stable at high temperatures and can efficiently reduce the IFT

between reservoir fluids. Due to different charges in reservoirs, the anionic surfactant is not suitable for positively charged carbonate rock but can usually be quite effective in negatively charged sandstone reservoirs. Cationic surfactants on the other hand, are usually a much better fit for carbonate reservoirs due to its identical charge which minimize the loss of surfactant to adsorption (Enick et al., 2012; Zolotuchin & Ursin, 2000). Nonionic surfactants have been used in the experimental work performed in this thesis due to its low adsorption (Jian et al., 2016).

For generation of stable and strong foams, the chosen surfactant needs to be able to satisfy a few primary characteristics. It needs to have a strong molecular interaction with both the water and the oil in the reservoir to achieve a low IFT as well as remaining its stability at high temperatures. In general, surfactants have a good solubility in brines, but at increasing temperatures, the solubility, and the reduction of the IFT decreases. To keep the cost of surfactants to a minimum, the adsorption, trapping and retention of surfactants by the porous media must be considered. The surfactants must be screened for the specific fluids and charge of the system so that the concentration of surfactants is constant and thereby maintain the ability to reduce the IFT. Another factor that must be considered is that surfactants can form viscous structures and rigid interfaces which can easily disturb the flow through the pores (Heller & Kuntamukkula, 1987; Lake et al., 2014). The laboratory evaluation of what surfactant to use in specific systems at reservoir conditions is therefore vital for a successful field implementation.

5. Numerical Modeling

Numerical modeling is a tool important in reservoir engineering because it permits simulation of projects without the trial and error in real life fields (Schlumberger, 2016). Reservoir modeling is a necessity for obtaining accurate predictions of the desirable performance of production for hydrocarbon reservoirs under different conditions. By minimizing time spent and volume of injected fluids to recover oil, the cost of a project can be considerably lower and the profit higher. An effective flooding requires detailed planning where simulators are a key part of that process (Ertekin et al., 2001; Ramirez et al., 1984). Other factors which contribute to the cost risk are regional variations of the relative permeability and fluid properties, complexity of the reservoir caused by heterogeneous rock properties and intricacy with the mechanisms of hydrocarbon-recovery. These factors cannot be changed, but proper planning and model setup can minimize the risk and set up the best production scenario as possible (Ertekin et al., 2001).

In addition to experimental studies, CO_2 foam can be analyzed by numerical modeling where a reservoir model is made to quantify and interpret flooding behavior in the past or current time as well as predicting future performance (Schlumberger, 2007). Numerical modeling combines mathematics, physics, computer programming and reservoir engineering to develop models that can accurately predict reservoir performance for different conditions of operation (Batycky et al., 2007; Ertekin et al., 2001).

5.1 Governing Equations and Setup for Numerical Modeling

The governing equations central for numerical modeling when describing fluid flow in a porous and permeable media are Darcy's law and the material balance equation. The simulator solves a combination of the equations for each cell in the model at every time step throughout the simulation time of the model (Schlumberger, 2007). Darcy's law describes the volumetric flow of a fluid through a porous media and its relation to the differential pressure. The equation for a single-phase flow has been listed as Equation 2.5, but for the model, Darcy's law without the gravity term has been used (Schlumberger, 2007):

$$q = -\frac{k}{\mu}\nabla P \qquad\qquad 5.1$$

Where q is the volumetric flow, k is the permeability, μ is the viscosity and P is the pressure.

The equation for material balance describes the continuity of fluids in a system where the mass of hydrocarbons originally in place (M_i) is equal to the produced mass (ΔM) combined with the residual fluid mass (M) in the reservoir (Skarestad & Skauge, 2012).

$$M_i = \Delta M + M \qquad\qquad 5.2$$

For a reservoir model, the equation can be written as:

$$-\nabla M = \frac{\partial}{\partial t} \cdot (\phi \cdot \rho) + Q \qquad\qquad 5.3$$

Where ∇M is the mass flux, ϕ is the porosity, ρ is the fluid density and Q is the cumulative flow (Schlumberger, 2007).

To simulate flow, the reservoir model is divided into smaller, three dimensional units where the progression of fluids and reservoir properties are monitored through the individual grid cells in different steps. The three main areas of interest when simulating flow is the flow between grid cells, flow from grid cell to a well completion and flow within wells and surface network. The total flow is

influenced by the combination of transmissibility, mobility and potential difference (Figure 5.1) (Schlumberger, 2007).
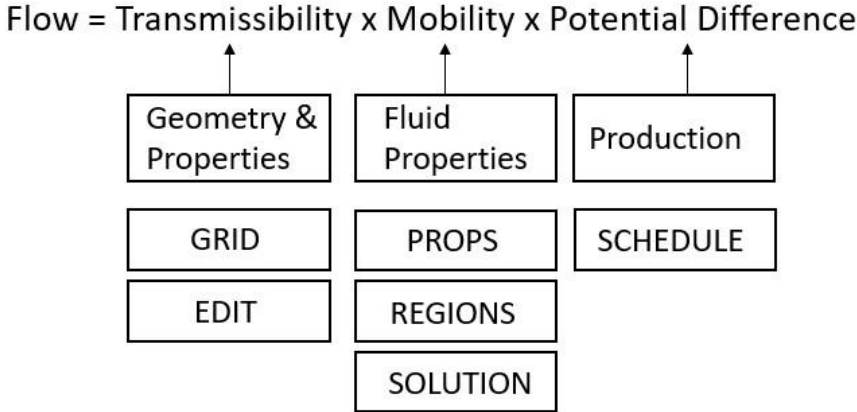
Figure 5.1 Input data in the reservoir model. Modified from (Schlumberger, 2007).

The ECLIPSE model consists of sections collected in a data file. Each section has its own function with keywords to identify input data, request output data or specify conditions for the model. The basic functions are listen in Figure 5.2 (Schlumberger, 2007). Figure 5.1 shows the relation between each section and the calculation and modeling of flow in the numerical model.

Figure 5.2 ECLIPSE model set up (Schlumberger, 2007).

5.2 Modeling of Fluids

The fluids in numerical modeling can be simulated by two different techniques in ECLIPSE. The first is the ECLIPSE Blackoil Simulator (E100) which assumes that oil and gas in the reservoir can be represented by a single component through time. The component can change its properties with the variation of temperature and pressure, but it will not change its composition. The other fluid model is the ECLIPSE Compositional Simulator (E300) which tracks each of the components in gas and oil in the reservoir. This method allows for compositional changes of the fluids near the critical points,

20

where changes in temperature and pressure can result in huge shifts in fluid behavior (Schlumberger, 2007).

Frequently used input data for numerical modeling includes petrophysical data and special core analysis (SCAL) experiments for rock data regarding reservoir properties, geometry and fluid properties for PVT data (Ertekin et al., 2001). PVT data comes from laboratory studies of reservoir fluids which are central in the model to describe the phase behavior at different stages of flooding. In addition, PVT data is used to calculate the different phase densities to set the initial conditions for the mass for each of the fluids in the grid blocks (Schlumberger, 2007). The calculation of saturation and pressure at initial conditions is also of high importance to determine the location and affiliated rates for the fluids. Production data for each of the different phases are used in the simulation to history match the model with the reservoir it is simulating. A reservoir simulation model can either be used to directly forecast the performance of a new project or be adjusted to historical behavior of an existing field which is called history-matching. Once history-matched, the model can be used to predict future production under different operational conditions. Results from this, combined with economic models are then used to make decisions regarding further operation in operating fields or for new projects (Kent Thomas, 2007; Schlumberger, 2007).

5.3 Foam Modeling

There are two approaches available to model foam: population balance model or a local equilibrium model. The population balance approach, models foam flow and by including mechanisms of generation and transport of foam on a pore level (Kovscek & Radke, 1993). For this thesis, the chosen foam model was the local equilibrium model in ECLIPSE. This model offers a simplified approach to reduction of computational effort. It assumes local equilibrium of foam generation and coalescence of gas bubbles and is an efficient and accurate tool for prediction of foam flow for field scale flooding.

For this foam model, the foam application was modeled in a functional form for the reservoir pilot, where the gas relative permeability modification from foam ($k_{r,foam}$), was estimated based on the relative permeability of CO_2 ($k_{r,g}$) and the mobility reduction factor (M_{rf}).

$$k_{r,foam} = k_{r,g} \cdot M_{rf} \qquad\qquad 5.4$$

Foam mobility reduction factor can be written as:

$$M_{rf} = \frac{1}{1 + (M_r \cdot F_s \cdot F_w \cdot F_o \cdot F_c)} \qquad\qquad 5.5$$

Where M_r is the reference mobility reduction factor and corresponds to the resistance normalized to flow for the minimum bubble size in the lack of factors to increase the bubble size. F_s is the mobility reduction factor caused by surfactant concentration, F_w is the mobility reduction factor caused by the water saturation, F_o is the mobility reduction factor caused by the oil saturation, and F_c is the mobility reduction factor caused by gas velocity (capillary number) which are all derived from laboratory experiments (Schlumberger, 2016).

Equation 5.6 expresses the individual reduction factor by the concentration of surfactants. It indicates that for low concentrations of surfactants and a correspondingly weak foam, contributes to a low reduction factor (F_s). Whereas a high concentration of surfactants results in a higher individual mobility reduction.

$$F_s = \left(\frac{C_s}{C_s^r}\right)^{e_s} \qquad\qquad 5.6$$

Where C_s is the effective surfactant concentration, C_s^r is the reference surfactant concentration, and e_s is an exponent which controls the steepness of the transition about the point $C_s = C_s^r$.

The reduction for gas mobility as a dependance upon water saturation is written as:

$$F_w = 0.5 + \frac{a\ tan[f_w(S_w - S_w^1)]}{\pi}$$

5.7

Where f_w is the weighting factor which controls the sharpness in the change in mobility, S_w is the water saturation, and S_w^1 is the limiting water saturation below which the foam ceases to be effective.

The reduction for gas mobility as a dependance upon oil saturation is written as:

$$F_o = \begin{cases} \left(\dfrac{S_o^m - S_o}{S_o^m}\right)^{e_o}, & if\ S_o \leq S_o^m \\ 0, & if\ S_o > S_o^m \end{cases}$$

5.8

Where S_o is the oil saturation, S_o^m is the maximum oil saturation above which the foam ceases to be effective and e_o is an exponent which controls the steepness of the transitions about the point $S_o = S_o^m$.

The reduction of gas mobility as a result of the capillary number is listed as:

$$F_c = \left(\frac{N_c^r}{N_c}\right)^{e_c}$$

5.9

Where N_c is the capillary number, N_c^r is the reference capillary number and e_c is an exponent which controls the steepness of the transition about the point $N_c = N_c^r$. The component sets the gas mobility for shear-thinning effect in low foam quality regions.

The capillary number is a dimensionless parameter and provides a measure of the ratio between capillary and viscous forces:

$$N_c = C_N \frac{\|K \cdot \nabla P\|}{\sigma_{wg}}$$

5.10

Where C_N is the conversion factor which depends upon the units used, K is the rock permeability, P is the pressure and σ_{wg} is the gas, water interfacial tension.

6. Field Pilot

This work is part of an international research program, led by the University of Bergen, which aims to optimize and field test CO_2 foam systems for CO_2 mobility control in EOR and CO_2 storage. A major part of the research program is a field pilot test in an onshore oil field in the Permian Basin of West Texas. The goal for the pilot was to evaluate the performance of CO_2 foam for EOR and CO_2 storage through upscaling the results from laboratory to field scale (Sharma, 2019).

The field selected for the project is the East Seminole Field (Figure 6.1). The field produces from the San Andres unit, a heterogeneous carbonate formation. The porosity of the reservoir has a range of 3 to 28% and it has a permeability range from 1 to 300 mD. The net pay zone is 110 ft with the reservoir top at a depth of 5300 ft under the surface. The field first started production in the 1940s and produced until the late 1960s where it had reached a production of 12% of the original oil in place (OOIP). In the 1970s, waterflooding was initiated, and throughout the 1980s an infill drilling program was implemented to reduce the well spacing to 40 acres. In 2013, the field saw a rapid decline in production, and the process of tertiary CO_2 injection was initialized. For a while, the production saw a great increase, but due to the reservoir heterogeneity and an unfavorable mobility ratio for the injected CO_2, the reservoir had a poor volumetric sweep and was identified as a good candidate for a CO_2 foam field pilot (Sharma, 2019). The residual oil saturation in the reservoir was found to be between 10 to 40% with an average of 31.7% (Sharma et al., 2017).

The pilot pattern was an inverted 40-acre five spot well area, with a central injection well and four surrounding production wells (Figure 6.1, gray shaded area) (Alcorn et al., 2020). The area pattern was selected due to rapid CO_2 breakthrough from historical CO_2 injection, high producing gas-oil-ratios (GOR), and short interwell distances. In addition, the geology in the area was representative for the whole field and there was good initial well injectivity which allowed for injection at desired rates while considering the flow resistance caused by foam generation in layers with high permeability (Sharma, 2019).

A surfactant-stabilized foam was used to control the CO_2 EOR challenges in the field. Measurements of surfactant adsorption and foam stability was performed on a laboratory scale to choose the correct surfactant for the pilot. Through foam quality scans, the Huntsman (L24-22) surfactant was recognized as the best fit for the reservoir system due its low adsorption on the reservoir rock (Jian et al., 2016). From laboratory tests, the recommended gas fraction was set to 0.70 and the surfactant concentration to 0.5wt% (Alcorn et al., 2018). The same setup and values for the pilot were used for all foam model sensitivity studies in this thesis.

Rapid SAG injections were chosen as the injection strategy due to its effectiveness and the fact that co-injection of surfactant solution and CO_2 as a CO_2 EOR method has been known to cause corrosion in standard oilfield pipelines and casings (Alcorn et al., 2018; Matthews, 1989). Different SAG injection scenarios such as single cycle SAG, multiple cycle SAG and rapid SAG were tested in the lab and in the numerical model to determine the most effective injection strategy. It was concluded that a rapid multiple cycle SAG was to be conducted for the pilot (Alcorn et al., 2018).

The pilot design consisted of 11 SAG cycles starting May 23, 2019. The SAG injection consisted of 10 days of surfactant solution injection, followed by 20 days of injection of CO_2 (Karakas et al., 2020). After SAG cycle 8, the field had a shutdown for 22 days. The same occurred at the end of SAG cycle 10, where the field was shut down for 60 days due to economic constraints for the operator. After starting back up, the last 3 days of surfactant slug 10 was injected to complete the slug. After the end of the pilot, water was injected for 14 days, before 14 days of CO_2, and then concluded with 30 days of water injection. The initial results of the pilot indicate that the infectivity of CO_2 was reduced by

70% when compared to the baseline CO_2 injection, indicating reduced mobility of CO_2 after each surfactant slug. The baseline and pilot injection showed an increased flow into the reservoir and a potential blocking of a high permeability layer (Alcorn et al., 2020).

Table 6.1 Reservoir and fluid properties of the San Andres unit for the East Seminole Field (Alcorn et al., 2020)

Reservoir Characteristic	Value
Depth	5200 ft
Permeability	1 to 250 mD (average: 13 mD)
Porosity	3 to 28% (average: 12%)
Pay thickness	110 ft
Reservoir pressure (initial)	2500 psig
Reservoir pressure (current)	3400 psig
Fracture pressure	3900 psig
Reservoir temperature	104°F
Oil gravity	31°API
Formation brine salinity	70,000 ppm
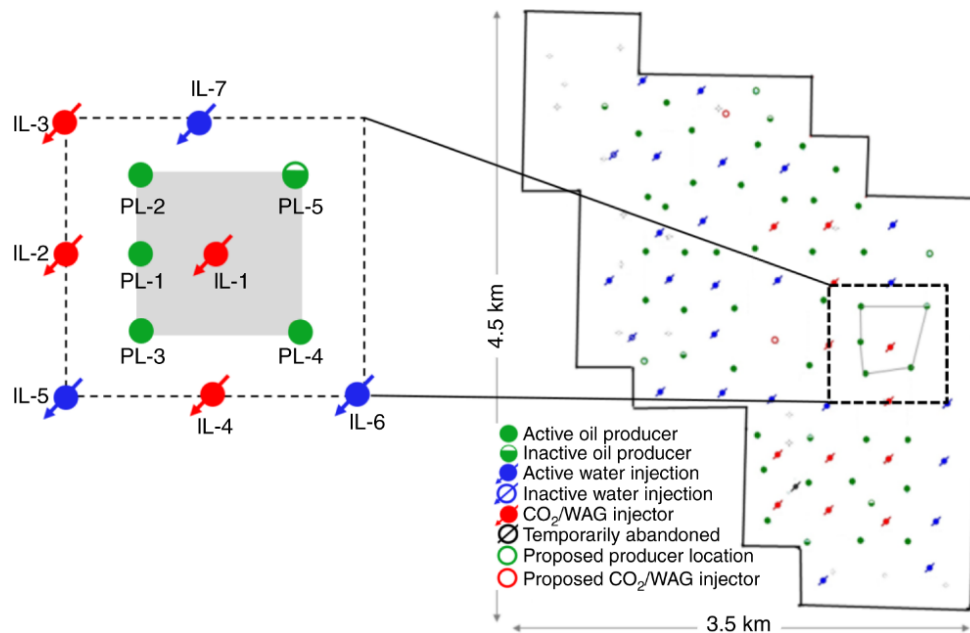
Figure 6.1 Outcrop of the chosen area for the pilot model of the East Seminole Field in the Permian Basin in West Texas. Cross-sectional model used in this thesis is a cut-out area between injection well IL-1 and production well PL-1 (Alcorn et al., 2019).

For this project, a high-resolution cross section of a full reservoir model built by Dr. Zachary Paul Alcorn and Dr. Mohan Sharma was utilized. The full model was based on a larger section of the East Seminole field in West Texas (Sharma, 2019). The sector reservoir model was validated by a history match of the historic waterflood and CO_2 injection periods before being used for CO_2 foam forecasting studies.

Part II. Experimental and Numerical Methods

7. Experimental Materials and Methods

In this chapter, the materials and methods used during the experimental work for this thesis are presented. All experiments were conducted at the Department of Physics and Technology at the University of Bergen in collaboration with fellow MSc candidate Hilde Halsøy. The main objective of the experimental work was to evaluate foam generation, strength, and stability during unsteady-state foam flow for SAG injections at different injection rates, gas fractions and surfactant concentrations. A secondary objective was to design a laboratory methodology representative of the unsteady-state foam flow to assist in the interpretation of the field pilot test. A total of 16 foam sensitivity experiments were conducted (Table 7.5).

7.1 Core Material and Preparation

All laboratory experiments were conducted on a single core plug. The core was a homogenous, water-wet outcrop Bentheimer sandstone that consisted of 92% quartz, 5% feldspars and 3% clay minerals (Peksa et al., 2015). The initial core preparation was completed by PhD candidate Aleksandra Soyke. The core was prepared by first rinsing it with water and drying it in a heating cabinet for a minimum 48 hours at 60°C until a stable weight was reached. The core was then saturated with brine under vacuum. The permeability was measured at different injection rates and calculated by Darcy's law, and porosity was calculated based on mass balance (Table 7.1). Porosity and permeability measurements were conducted as described in Appendix A. The absolute permeability was measured between each experiment to monitor any changes in permeability from residual saturation of surfactant or CO_2 in the core. Only minor variations were observed, and the results of these measurements are presented in Appendix B.

Table 7.1 Bentheimer core properties used in the experimental work

Properties	Values
Diameter [cm]	3.88 ± 0.01
Length [cm]	24.40 ± 0.01
Pore Volume [mL]	62.16 ± 0.01
Porosity [%]	21.54 ± 0.1
Permeability [D]	2.14 ± 0.03

7.1.1 Cleaning and Preparation Procedure

The same core plug was used throughout the whole experimental part of the project. It was therefore important that the core was properly cleaned and prepared to prevent cross contamination between each experiment. After each complete experiment, the core was filled with CO_2 and surfactant solution residue which had to be flushed out completely. The core flushing routine was as follows:

1. 2 to 3 PV of cleaning solvent (IPA composition listed in Table 7.2) was injected at a maximum rate of 150 mL/h through the core plug to displace the CO_2.
2. 10 to 12 PV of brine was then injected at a rate of 40 mL/h to displace the IPA-solution and remaining CO_2.
3. Brine at high rate or a maximum of 150 mL/h was then injected for 1 to 2 PV to confirm proper flushing.

If the core still produced CO_2 after a full cycle of cleaning, the routine was repeated until the production was clear.

7.2 Fluid Properties

The fluid compositions and properties at experimental conditions (T = 40°C, P = 200 bar) are listed in Table 7.2 and 7.3, respectively. The foaming agent was a nonionic surfactant from Huntsman (SURFONIC L24-22) and was chosen for this project due to its relation to the field pilot conducted in the Permian Basin of West Texas. From previous surfactant screening studies, it had been identified as well suited for the project due to its low adsorption on reservoir rock (Alcorn et al., 2018; Jian et al., 2016). The surfactant was dissolved in brine at a concentration of 5000 ppm (parts per million) and 2500 ppm. Between each experiment, the core was cleaned by injecting Isopropyl Alcohol (IPA) solution before injecting brine. The IPA solution consisted of 87 wt.% isopropanol in distilled water, and the brine consisted of 3.5 wt.% Sodium Chloride (NaCl) in distilled water. The same brine was used for all experiments.

Table 7.2 Fluid compositions used in the experimental work

Fluid	Composition
Brine	Distilled water + 3.5wt.% NaCl
5000 ppm surfactant solution	Brine + 5000 ppm surfactant (*)
2500 ppm surfactant solution	Brine + 2500 ppm surfactant (*)
CO_2	>99.999% CO_2
IPA	Distilled water + 87wt.% Isopropanol

(*) Anionic surfactant. SURFIONIC L24-22

Table 7.3 Fluid properties at experimental conditions (T = 40°C, P = 200 bar)

Fluid	Density [g/mL]	Viscosity [cP]
Brine	1.016 [1]	0.665 [1]
CO_2	0.840 [2]	0.078 [2]

(1) Values obtained from (El-Dessouky, 2002)
(2) Values obtained from (Lemmon et al., 2012)

7.3 Experimental Setup

Figure 7.1 shows a schematic diagram of the experimental setup which was used for all laboratory experiments. The Bentheimer core plug was wrapped with nickel foil and placed in a vertically oriented Hassler core holder. The nickel foil acted as a barrier to reduce CO_2 diffusion into the rubber sleeve. The core holder was placed in a heating cabinet with a constant temperature of 40°C. An ISCO pump was used to set the confinement pressure by injecting hydraulic oil into core holder and constantly adjusting the confinement pressure to be 70 bar over the system pressure.

At the outlet of the system, two Equilibar back pressure regulators (BPR) regulated by a N_2 tank were connected in series to maintain a system pressure of 200 bar and minimize pressure fluctuations. Two ESI pressure transducers with ranges of 0 to 250 bar were used to measure the inlet and outlet pressure, and two ESI pressure transducers with ranges of 0 to 400 bar were used to measure the confinement and BPR pressure. The differential pressure was measured using APLISENS Smart Differential Pressure Transmitter and the values measured were used to calculate the foam apparent viscosity (APPV).

The pumps used include a Quizix QX6000 pump for injecting brine, IPA and surfactant solution, and a Quizix Q6000 – 10k for injecting CO_2. The CO_2 gas was pressurized with a Haskel Gas Booster before entering the pump. The pumps were connected at the inlet of the core holder and were controlled through the Quizix PumpWorks Software program on the laboratory computer. At the outlet, the fluids were depressurized and separated at atmospheric conditions by passing through the BPRs. The

liquid was then collected in a reagent bottle and the gas was vented through an adsorption column. All equipment utilized for the experiment are listed in Table 7.4.
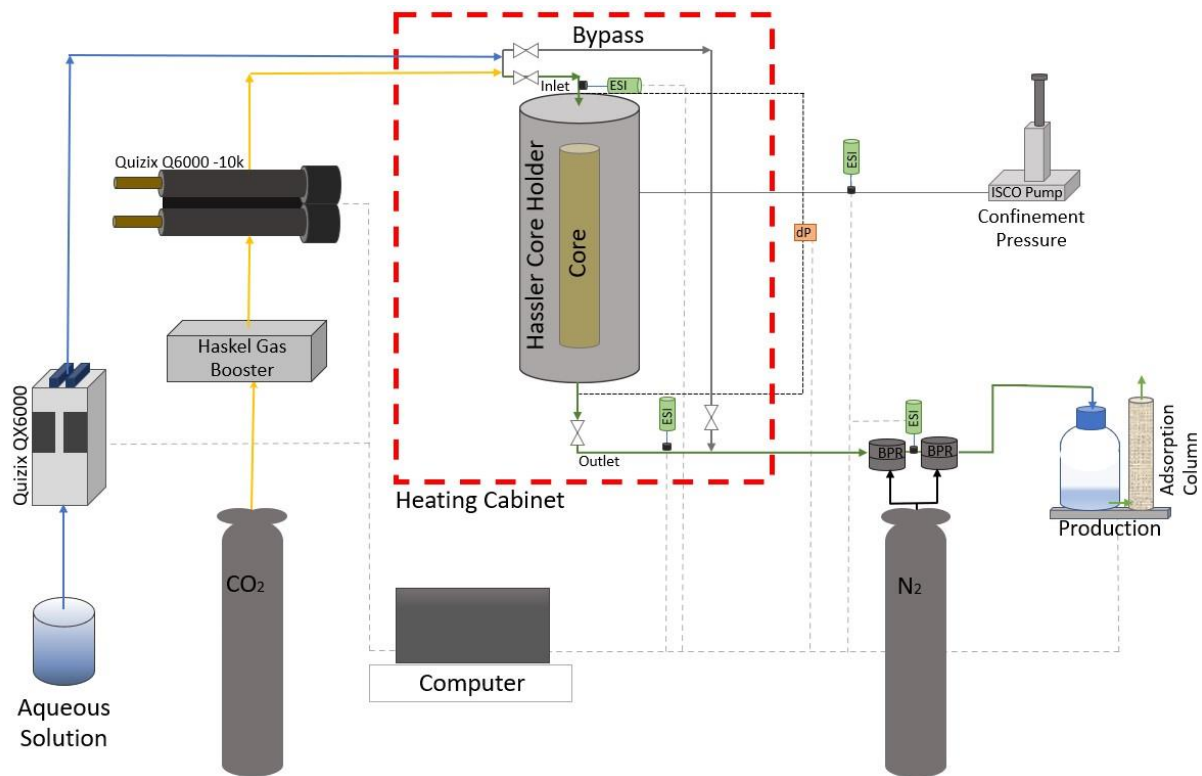
Figure 7.1 Schematic diagram of the experimental setup with the red line representing the heating cabinet, yellow and blue lines representing CO_2 and brine/surfactant solution flow, respectively, and the green line represents the flow of fluids during experiments.

Table 7.4 List of equipment used in the CO_2 foam experiments

Heating cabinet
2" diameter Hassler core holder
ISCO Syringe pump for confinement pressure in core holder
Quizix Q6000 – 10k pump for CO_2 injection
Quizix QX6000 pump for injection of brine and surfactant solution
Equilibar Back Pressure Regulator (BPR) regulated by a N_2 tank
APLISENS Smart Differential Pressure Transmitter (range 0 to 16 bar)
ESI Pressure Transducers for pressure measurements (range 0 to 250 bar for inlet and outlet and range 0 to 400 bar for BPR and confinement pressure)
Reagent bottle for collecting production
Adsorption column
CO_2 tank for gas injection
Haskel gas booster to pressurize injection gas
N_2 tank for BPR regulation
Automatic valves
Swagelock valves, fittings and tubings
Computer to operate pumps and automatic valves, overlook pressure data from differential pressure and ESI transducers, as well as continuous logging of experimental data

7.3.1 Set-up Maintenance

In between each experiment, the O-rings in the BPRs had to be changed due to CO_2 reacting and diffusing with the rubber material as can be seen in Figure 7.2. The rubber sleeve in the core holder was protected from the CO_2 by the nickel foil around the core, thereby was not necessary to be replaced for each experiment.
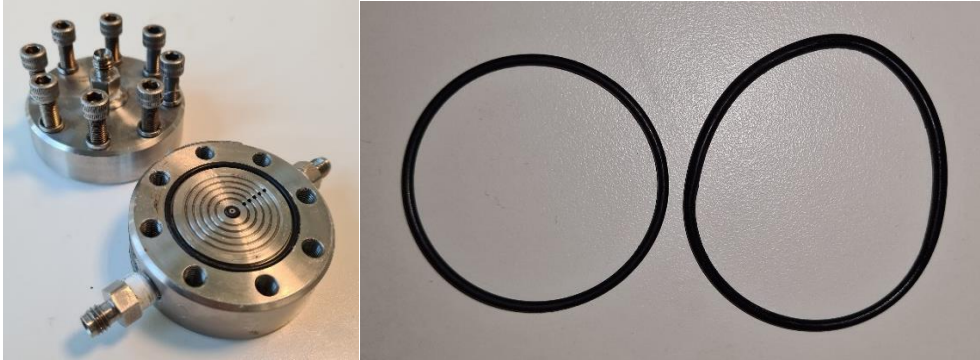
Figure 7.2 BPR with associated O-ring damaged by diffusion from contact with CO_2 during SAG injections.

7.4 Experimental Overview

A total of 16 foam sensitivity experiments were conducted for the experimental part of the thesis (Table 7.5).

Table 7.5 – Experimental overview

Injection strategy	Injection fluids	Gas fraction [f_g]	Injection rate [ft/day]	Number of experiments
WAG (baseline)	CO_2 and brine	0.6	4	1
SAG 5000 ppm surfactant solution	CO_2 and 5000 ppm surfactant solution	0.6	4	3
		0.7		3
SAG 2500 ppm surfactant solution	CO_2 and 2500 ppm surfactant solution	0.6	4	3
		0.7		2
SAG 8 ft/day	CO_2 and 5000 ppm surfactant solution	0.6	8	2
		0.7		2

7.5 Experimental Procedure

All experiments were conducted on the same core, initially 100% saturated with brine. CO_2 and surfactant solution were injected in alternating slugs with different surfactant concentrations, gas fractions and injection rates (listed in Table 7.5). The objective of the experimental work was to evaluate foam generation, strength, and stability of unsteady-state CO_2 foam in porous media at reservoir conditions to determine which injection rates, surfactant concentrations and gas fractions were suitable for generating strong and stable foam. A baseline water alternating gas (WAG) injection was performed for comparison. Each injection strategy and sensitivity are described below. The individual sensitivity injections were repeated two or three times each and the results were combined and averaged into one graph for each case.

7.5.1 Water Alternating Gas (WAG) Injection

Water alternating gas (WAG) injection was performed by injecting brine and CO_2 in alternating slugs at a superficial velocity (u) of 4 ft/day with a gas fraction (f_g) of 0.60. Each full cycle had the combined size of ~0.25 pore volume (PV) total, with the brine injection being 0.1 PV and the volume of the CO_2 injection was adjusted to keep the gas fraction at 0.60. In total, 12 cycles were injected, with the last CO_2 slug being 1 PV. The differential pressure was continuously logged for calculation of the apparent viscosity (APPV).

7.5.2 Surfactant Alternating Gas (SAG) Injections

Surfactant alternating gas (SAG) injections were performed with the same procedure as described for WAG injection in section 7.5.1. The first two cycles in each SAG experiment were without any surfactant and, thus, were WAG cycles. The next two cycles had 50% brine-diluted surfactant slugs which reduced the surfactant concentration by half, and the next 8 SAG cycles were injected with the concentration of surfactant solution listed in Table 7.2. The parameters in the sensitivity study were changed as listed in Table 7.5 which included testing a gas fraction (f_g) of 0.60 or 0.70, surfactant concentration of 2500 parts per million (ppm) or 5000 ppm, and a superficial velocity (u) of 4 ft/day or 8 ft/day. The differential pressure was continuously measured during the experiments for calculation of apparent viscosity (APPV).

7.5.3 Evaluation of Uncertainty and Smoothing of the Experimental Data

The experimental pressure measurements had high levels of fluctuation caused by the BPRs in the experimental setup. This was also observed by Skjelsvik (2018) and Soyke (2020). A visualization of the general uncertainty in the experiments can be seen in Figure 7.3, where the light colored points are the raw, unsmoothed data and represents the uncertainty of the dark colored smoothed data lines. Due to the high pressure fluctuations and the nature of unsteady-state flow, it was more appropriate to deploy a smoothing method on the raw experimental data to account for the general uncertainty.

The raw experimental pressure data was smoothed using a Python script developed by PhD candidate Aleksandra Soyke. The script reduced the noise in the raw data which had 90 measured pressure points per minute throughout the experiment as input. The method used a Savitzky-Golay filter for smoothing and is based on local least-squares polynomial approximation (Schafer, 2011) which was proven by Savitzky and Golay (1964) to reduce noise while still maintaining the height and shape of the peaks.

The main goal is to find coefficients in the filter that perseveres high order polynomials. They are derived by least-squares fitting for a polynomial for a given degree within a sliding window. The smoothed points are found by replacement of every data point with the value found by the fitted polynomial at the window center. Choosing the right size of the window function is therefore crucial

for not blurring important data points or to not filter enough to be able to see the main trends in the data (Suhling et al., 2004).

Figure 7.3 shows comparisons of the unsmoothed data for the baseline WAG in light blue and SAG in light green with the smoothed data for the baseline WAG in darker blue and SAG in darker green.
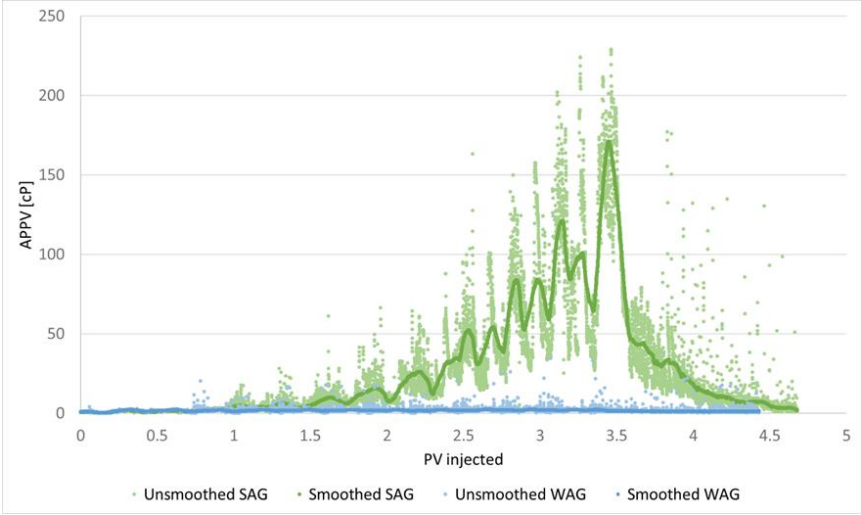
Figure 7.3 Unsmoothed (lighter colors) and smoothed (darker colors) experimental data for SAG and baseline WAG.

8. Numerical Modeling Methods

For this chapter, the setup and methods used for simulation of macroscopic flow of foam in a cross-sectional reservoir model are presented. The aim was to evaluate CO_2 foam mobility reduction performance related to foam generation and strength of different laboratory derived foam models at field-scale through analyzing injection bottom hole pressure (BHP), CO_2 tracers, producing gas-oil ratio (GOR), and water cut. In addition, the effect of residual oil on foam was evaluated. ECLIPSE has been used as the main tool during the numerical simulation, and Schlumberger's Petrel E&P has been used for data evaluation and visualization.

The numerical model used in this thesis was built from field data to represent the East Seminole Field which is a heterogeneous carbonate reservoir in the Permian basin of West Texas (Alcorn et al., 2016; Sharma et al., 2017). The cross-sectional model (Figure 8.1) is a cut-out from a sector reservoir model and is the area between well IL-1 and PL-1 (Figure 6.1). The IL-1 well is an injection well and PL-1 is a production well. The model consists of 28 vertical layers and has a length of 750 ft between the wells. The static geological structure and properties for the reservoir model was generated from integrating petrophysical well logs, core data and regional stratigraphy. The stratigraphic tops of the reservoir flow zones, and the impermeable zones were mapped and correlated across the model to build the framework of the geological model (Sharma et al., 2017). The dimensions of the model are 75 x 1 x 54 cells and the layer thickness varies from 1 to 10 feet depending on the stratigraphic mapping of the units (Sharma, 2017).

Porosity, permeability, and fluid saturations were all assigned to the geological framework for the model and were correlated to the flow zones through core data tied to neutron, gamma ray, resistivity, and density logs. Logs from each of the wells at the location supplied information to establish the interwell regions (Alcorn et al., 2018). The porosity in the reservoir zones had a range from 12 to 15%, and the permeability was measured to be between 1 mD to 300 mD with an average of 15 mD (Sharma et al., 2017).

Figure 8.1 Grid and permeability layers for the numerical cross-sectional model, visualized in Petrel (Alcorn et al., 2020).

8.1 Fluids in the Model

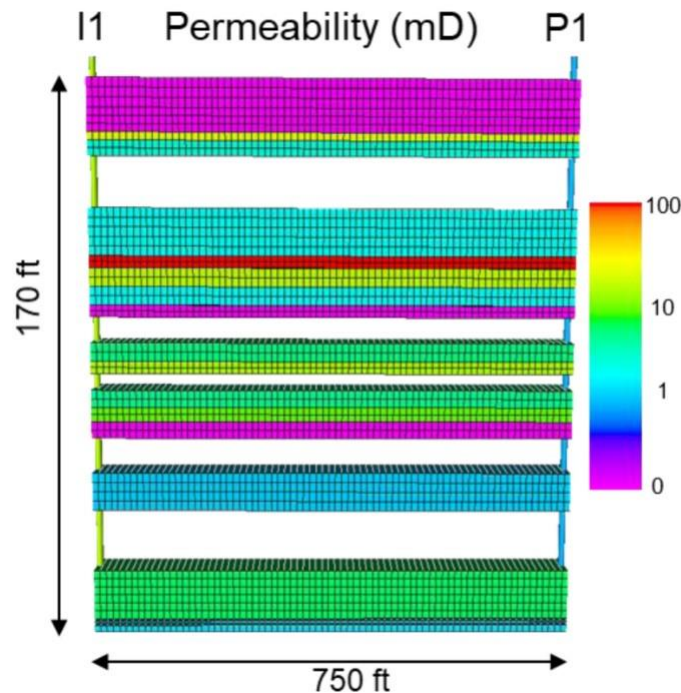A conventional finite-difference compositional model was set up by using a tuned Equation of State (EoS) model. In ECLIPSE, the liquid phase is usually modelled by using a single component. In this work, a second component (surfactant) was introduced for the local equilibrium foam model. Desorption and adsorption of foam in the model were obtained by modeling a reversible chemical reaction (Sharma et al., 2017). The foam model parameters were derived from core-scale laboratory experiments (foam quality and rate scans) with reservoir core material. The focus of the experimental work was to determine the optimal surfactant concentration and gas fraction which generated the most stable and strongest foam, given economic field restrictions (Alcorn et al., 2018).

Reservoir oil samples from the field were used for PVT studies (Figure 8.2) for the hydrocarbon components in the numerical model (Sharma, 2019). Calculations of phase behavior based on a Peng-Robinson EoS model and with a Peneloux molar volume correction for predicting liquid densities and saturations more carefully. The EoS model was adjusted with available PVT data with a total of 6 components, which included 2 C7+ components, and the lighter components merged as CO_2, N_2+C1, H_2S+C2+C3 and C4+C5+C6 (Kristiansen, 2018; Sharma, 2019). The reported C7+ fraction was separated using Gamma distribution before a Gaussian quadrature-based lumping, the critical properties were estimated by the Lee-Kesler correlation. For assessing miscibility, a parachor was related with each of the components to calculate the surface tension. The Pedersen model was tuned to match the viscosity data for oil while at the same time, not include previous parameters trough regression. The compositions were assumed to be uniform in all cells with values based on the EoS model at the start of the CO_2 simulation (Kristiansen, 2018; Sharma, 2019).

From laboratory tests, the reservoir was found to have mixed wettability with a slight lean towards oil-wet behavior, which is similar to other carbonate reservoirs. This was matched in the numerical model. The base water-oil relative permeability (Figure 8.3, left) was calculated by adjusting the parameters for a Corey-type model to available data from core flooding. The relative permeability for oil displacement by CO_2 (Figure 8.3, right) was set to a straight line with an endpoint of 1 due to an assumption of miscible displacement (Alcorn et al., 2018; Kristiansen, 2018; Sharma et al., 2017).
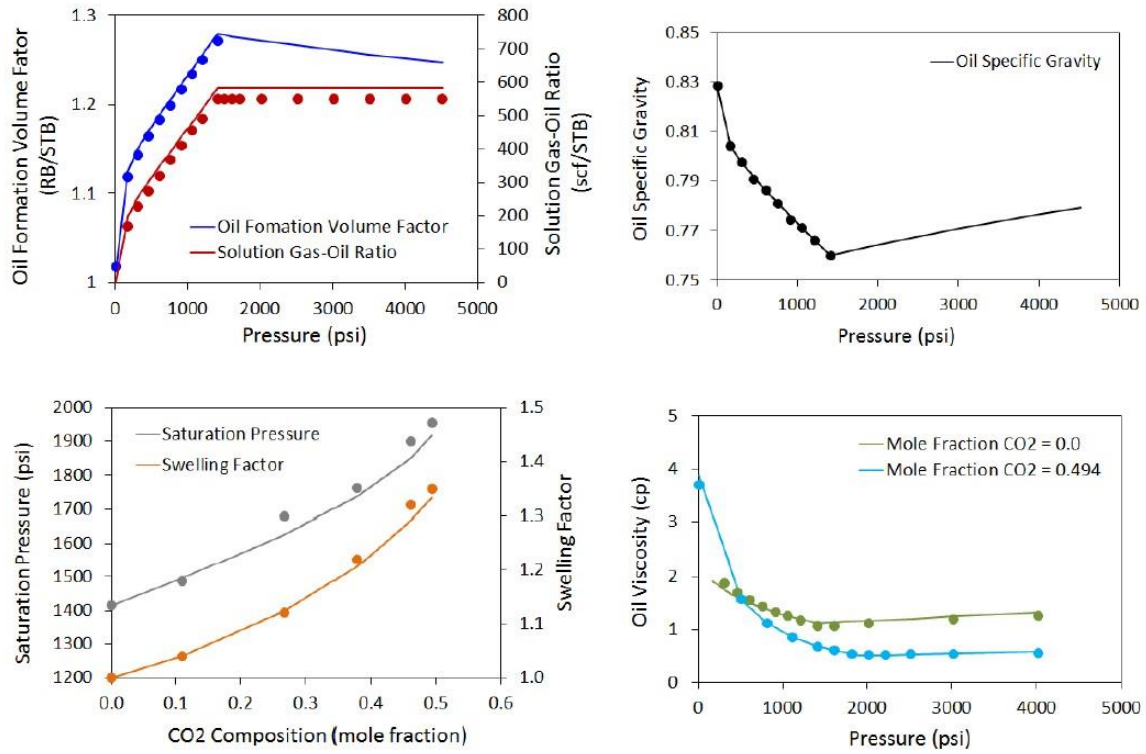
Figure 8.2 Fluid model used in the cross-sectional model with values from available PVT data such as differential liberation, swelling test and viscosity measurements (Sharma, 2019).
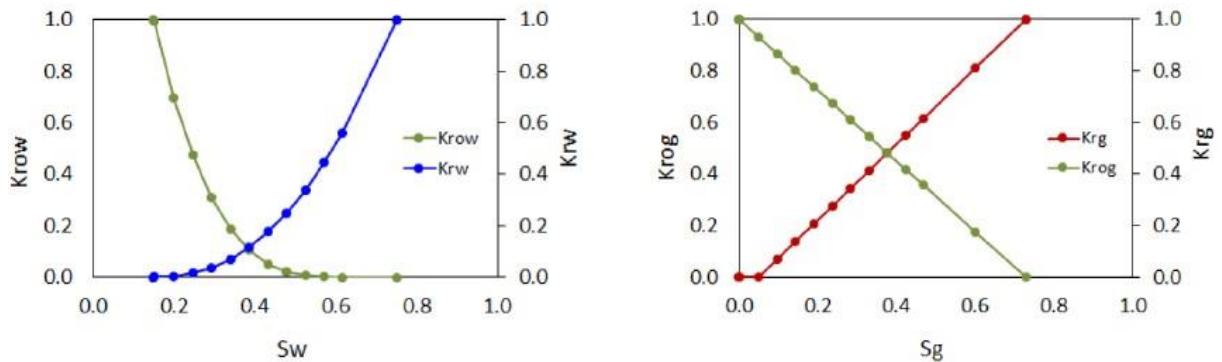
Figure 8.3 Base water-oil relative permeability for water and gas (left) and CO_2 displacement of oil (right) for the cross-sectional model (Sharma, 2017).

8.2 Foam Modeling

The foam model parameters were derived by fitting the empirical foam model to foam quality scan data through regression (Figure 8.4).
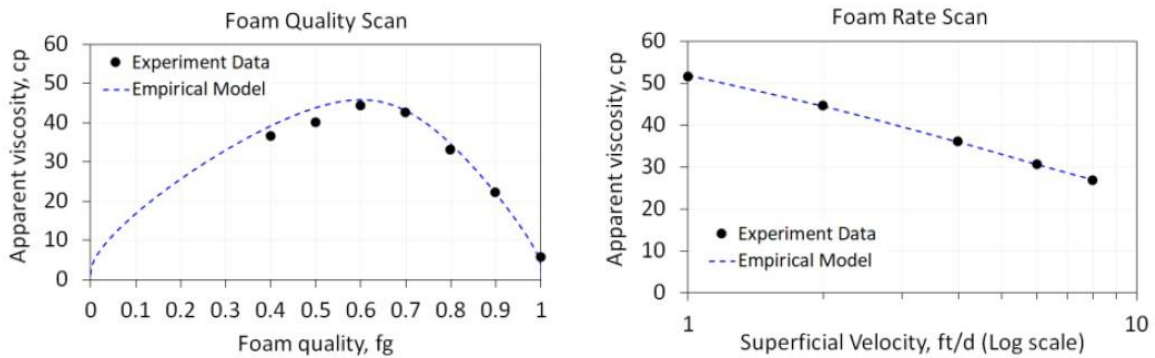
Figure 8.4 Experimental data and empirical foam model fit to a quality scan (left) and a rate scan (right) (Sharma, 2019).

The effect of permeability on foam was modeled by dividing the model into three permeability regions (Figure 8.5). Region 1 was defined as areas with permeability lower than 10 mD, Region 2 had a range from 10 to 50 mD in permeability, and Region 3 were all areas with a permeability greater than 50 mD. Each permeability region was assigned different foam model parameters as shown in Table 8.1 (Sharma, 2019).
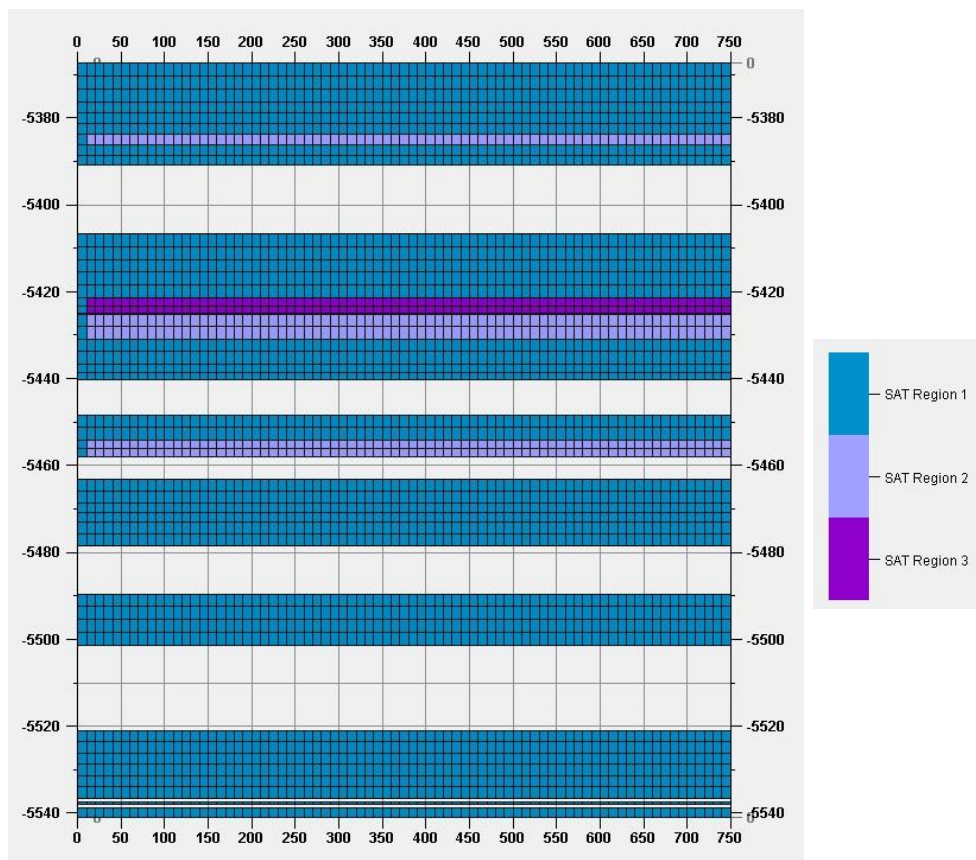
Figure 8.5 Permeability Region 1 to 3 in the numerical cross-sectional model.

In ECLIPSE, the foam model was placed in the PROPS section of the model. The different sections of the foam model are listed in Table 8.1 for the experimentally derived base foam model designed by

Dr. Mohan Sharma (2019). FOAMFRM is the mobility reduction factor and defines the level of reduction of mobility caused by foaming of the CO_2. The *fmmob* value sets the reduction value and is the reference gas mobility reduction factor for foam. FOAMFSW is the key for water saturation in the model and includes *fmdry* that is the water saturation in vicinity of which foam collapses, and *epdry* is the parameter controlling the abruptness of foam collapse. The base values used for *fmmob*, *fmdry* and *epdry* in Region 2 were obtained through quality scan data (Figure 8.4, left) with regression of the empirical foam model. FOAMFCN is the key for the capillary number and is defined by *fmcap* which is a parameter set to the smallest capillary number expected in the simulation, and *epcap* is the parameter set to capture shear-thinning behavior in low quality regimes. Both *fmcap* and *epcap* were obtained by fitting the foam model to rate scan data (Figure 8.4, right). FOAMFSC is the surfactant concentration and is represented by *fmsurf* which is the reference surfactant concentration. It is found by estimating the critical micellar concentration (CMC) that is the minimum of surfactant concentration needed to generate foam. It is also altered by *epsurf* which is the parameter controlling the effect of surfactant concentration and set by an assumption due to lack of data for this foam model. FOAMFST is the gas-water interfacial tension (IFT). FOAMFSO sets the level of oil saturation at which foam ceases to exist. *fmoil* is the reference high oil saturation for foam collapse and was estimated for the base model to be 0.28 through CO_2 EOR experiments. *epoil* is the parameter controlling the effect of oil saturation and was assumed due to lack of data. The values for *fmmob*, *fmdry* and *epdry* in the foam model for Region 1 and 3 were also assumed. For Region 1, it was assumed to not be any foam generation and thereby no reduction in mobility. The high permeability in Region 3 was assumed to have most of the foam generation (Sharma, 2019).

Table 8.1 Base foam model setup for the base SAG simulation case derived from experimental data (Sharma, 2019)

Parameter	Region	Base foam model	Remarks
fmmob	1	0	Assumed no foam generation
	2	630	Base value based on Quality Scan
	3	1200	
fmdry	1	0.32	
	2	0.27	Base value based on Quality Scan
	3	0.22	
epdry	1	500	
	2	100	Base value based on Quality Scan
	3	25	
fmcap	All	7.8E-07	Base value based on Rate Scan
epcap	All	0.65	Base value based on Rate Scan
fmsurf	All	0.175	Base value assumed 5 times of CMC
epsurf	All	1	
fmoil	All	0.28	Base value from EOR experiments
epoil	All	1	

8.3 Model Initialization

The reservoir had a hydrostatic pressure of 2300 psi in the main pay zone (MPZ). The initial water saturation was set to 0.5 based on laboratory SCAL studies for the MPZ and 0.68 for the residual oil zone (ROZ) due to natural water flooding occurring (Sharma, 2019). Remaining oil saturation (ROS) was suggested to be between 0.1 and 0.4 in the ROZ with an average of 0.32 (Honarpour et al., 2010).

The injection scheme for the numerical model is illustrated in Figure 8.6. The injection was stared January 1, 2018, with periods of WAG injection performed for over the course of a year before the start of the pilot. The pilot was started May 23, 2019. It contained 11 rapid SAG cycles which were injected over the course of the following 12 months, with the injection scheme described in Chapter 6, with a target gas fraction of 0.70, and target injection rate of 500 rb/day. The post pilot period went from the end of the pilot until September 1, 2020, with injection of water and CO_2.
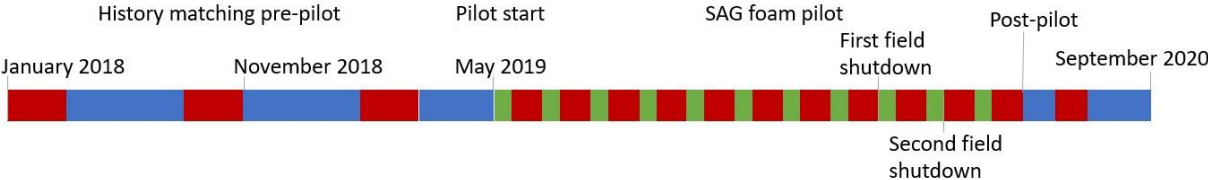
Figure 8.6 Full flooding scheme for the numerical model, described in Chapter 6.

8.3.1 Tracers in ECLIPSE

Tracers were used in the models to monitor breakthrough time between injection and production of the different fluid phases in the reservoir. A CO_2 tracer, GS1, and a water tracer, WT1 were injected before the start of the pilot, GS1 on January 3, 2018, and WT1 on November 21, 2018. These were used to set a baseline for the flooding through the reservoir before foam was introduced. Shortly after the start of the pilot, CO_2 tracer, GS2, and water tracer, WT2, were injected. GS2 was injected in CO_2 slug 1 on June 3, 2019, and WT2 was injected in water/surfactant slug 1 on May 23, 2019. At the end of the pilot, CO_2 tracer, GS3, was injected in CO_2 slug 11 on June 11, 2020.
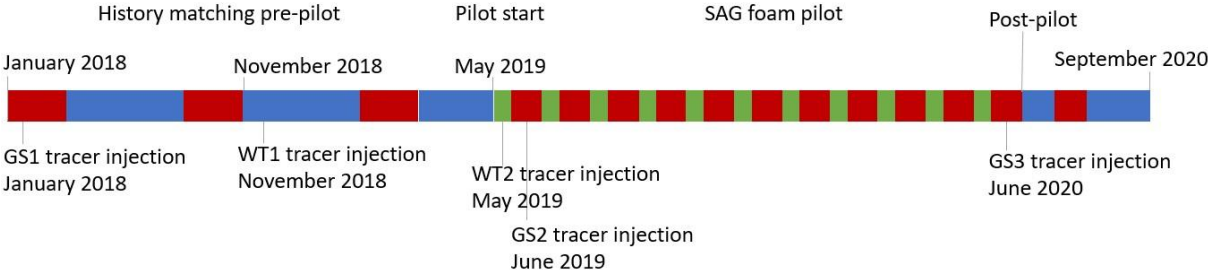
Figure 8.7 Placement of fluid tracers in the numerical model.

8.4 Numerical Overview

The numerical work aimed to evaluate CO_2 foam mobility reduction performance for generation and strength of different experimentally derived foam models. In addition, the effect of residual oil on foam was evaluated. A total of 18 numerical foam sensitivity runs (Table 8.2) were set up.

Table 8.2 – Numerical overview

Simulation cases	Number of Runs
Baseline WAG	1
Base SAG	1
Sensitivity study - Experimentally derived foam models	8
Permeability dependent combinations of experimentally derived foam models	3
Effect of oil on base SAG	5

8.5 Numerical Method

Numerical method and setup for the different numerical model sensitivity cases. The model was run in ECLIPSE 300 and visualized in Petrel. Bottom-hole pressure, tracer values, Gas-oil ratio and water cut were exported to Excel and graphed.

8.5.1 Baseline WAG and Base SAG Simulation Cases

A WAG case, without surfactant solution, was set-up to establish a baseline and confirm foam generation. The WAG case was directly compared to an identical base SAG simulation case with surfactant solution. As described in Section 8.2, the model was set up to account for shear-thinning by not letting foam form in the near well area as well as account for the effect of different permeabilities on foam. The foam model used in the Base SAG case is listed in Table 8.3 and was described in section 8.2.

Table 8.3 Base SAG foam model setup for each of the permeability regions (Alcorn et al., 2018; Rognmo, 2019)

Base SAG Foam Model Setup	Region 1	Region 2	Region 3
FOAMFRM (*fmmob*)	0	630	1200
FOAMFSW (*fmdry, epdry*)	0.32, 500	0.27, 100	0.22, 25
FOAMFCN (*fmcap, epcap*)	7.80E-07, 0.65	7.80E-07, 0.65	7.80E-07, 0.65

8.5.2 Sensitivity Study – Experimentally Derived Foam Models

Four different laboratory derived foam models (Table 8.4) were tested in the numerical model with the purpose of comparing foam performance for the individual models. The foam models listed in Table 8.4 were placed in the model with the same values for all permeability regions.

Table 8.4 Experimentally derived foam models (Alcorn et al., 2018; Rognmo, 2019)

Foam Models (from experimental data)				
	1	**2**	**3**	**4**
fmmob	41.5	108	192	248
fmdry	0.595	0.27	0.4	0.313
epdry	35	100	84	46.8
fmcap	2.14E-06	7.80E-07	9.00E-07	8.50E-07
epcap	0.87	0.65	0.59	0.71

8.5.3 Sensitivity Study – No Foam in Low Permeability Regions

For this section, the concept of shear-thinning by not allowing foam to form in the near well region was tested to evaluate how it influenced the performance of the experimentally derived foam models. In addition, no foam was allowed to generate in the low permeability regions with permeability values under 10 mD (Region 1, Figure 8.5).

As described in section 8.5.2, the individual foam models were placed in all permeability regions, but for this section, the values in the first permeability region were changed to the values from the base SAG foam model listed in Table 8.3. As described in section 8.5.1, a value for *fmmob* = 0 will not allow for generation of foam in the permeability layers covered by Region 1.

Table 8.5 Foam model setup (1* to 4*) with values from Table 8.3 and 8.4 for each permeability region

	Foam models			
	1*	**2***	**3***	**4***
Region 1	Base 1	Base 1	Base 1	Base 1
Region 2	1	2	3	4
Region 3	1	2	3	4

8.5.4 Sensitivity Study - Combinations of Experimentally Derived Foam Models

Different combinations of foam models were places in the different permeability regions. As described in section 4.1.1, permeability plays a central role in the generation of foam where lower permeability hinders generation of strong foam. This concept can be simulated by using foam models with lower values for *fmmob* (reference gas mobility-reduction factor for foam (Section 8.3)) in the lower permeability regions. Foam models with higher values for *fmmob* were placed in the other regions representing layers with higher permeability.

The combinations made for the experimentally derived foam models tested in this section has been listed in Table 8.6 and the foam model values are listed in Table 8.4. Combination A consisted of foam model 1, 2 and 3, where foam model 1 had the lowest value for *fmmob* with 41.5, foam model 2 had a *fmmob* value of 108 and foam model 3 had a *fmmob* value of 192. Combination B consisted of foam model 1, 2 and 4, where foam model 1 and 2 were the same as for the first combination, and foam model 4 was the model with the highest value for *fmmob* with 248. Combination C consisted of foam model 2, 3 and 4.

Table 8.6 Foam model combination with experimentally derived foam models listed in Table 8.4, for combination A to C

	Combination A	**Combination B**	**Combination C**
Region 1	1	1	2
Region 2	2	2	3
Region 3	3	4	4

8.5.5 The Effect of Oil on Foam in the Base SAG Model

The effect on residual oil on foam was tested for the base SAG foam model. As described in section 4.1.3, residual oil can have a great impact on the effectivity of generation and stability of foam. The base foam model (listed in Table 8.3) was therefore adjusted to test for higher and lower values for oil sensitivity to evaluate how the foam model responded.

As described in Section 8.2, *fmoil* is the maximum oil saturation above which foam ceases to be effective. It was set to 0.28 in the base foam model after being evaluated through laboratory tests. The value tested in *fmoil* has been called So*. So* = 0.40 was tested as an upper value for increased foam tolerance to oil, whereas the other values were lower for testing reduced tolerance to residual oil saturation. As described in Chapter 6, the maximum residual oil saturation found in the reservoir was 40%, hence testing a higher value was unnecessary.

Table 8.7 Values for reference high oil saturation for foam collapse, tested in the base SAG foam model (Table 8.3)

	So* = 0.05	So* = 0.10	So* = 0.15	So* = 0.20	So* = 0.40
fmoil	0.05	0.1	0.15	0.20	0.40
epoil	1	1	1	1	1

8.5.6 Evaluating Foam Performance

When valuating foam performance, foam generation, strength and sweep efficiency were evaluated with results from the numerical model cases. The parameters investigated was bottom hole pressure (BHP), fluid tracers, gas-oil ratio (GOR), and water cut. The BHP indicated foam generation through an increase in the pressure in the injection well. The foam strength was evaluated through fluid tracers by looking at the migration rate and delay in breakthrough time (Chou, 1991). The GOR was also used to evaluate the foam strength by determining the degree of decline in ratio for different foam cases which indicate reduction of the gas permeability (J. E. Hanssen & Dalland, 1994). Water cut was investigated to determine the volumetric sweep efficiency of the different cases. Due to the low residual oil saturation in the reservoir, a higher water cut can signalize higher volumetric mobilization of reservoir fluids (Chou, 1991; Gauglitz et al., 2002) in the numerical model.

Part III. Results and Discussion

9. Unsteady-state WAG and SAG Injections

Foam generation, strength and stability were evaluated at different gas fractions, surfactant concentrations and injection rates for unsteady-state core floods. A secondary objective was to design a laboratory methodology representative of the unsteady-state foam flow to assist in the interpretation of the field pilot test. All experiments were conducted with the same temperature and pressure conditions at T = 40°C and P = 200 bar, respectively. The same core was used for all experiments. An overview of the different sensitivities tested is listed in Table 7.5. The individual sensitivity injections were repeated two or three times each, and the results were combined and averaged into one graph for each case.

9.1 Baseline WAG and SAG

To establish a baseline, a WAG with alternating injection of brine and CO_2 was first performed without a foaming agent (procedure listed in Section 7.5). The baseline water alternating gas (WAG) injection was compared to an identical surfactant alternating gas (SAG) injection with a 5000 ppm surfactant solution. Both injections had an injection rate of 4 ft/day and a gas fraction of 0.60.

Figure 9.1 shows apparent viscosity (APPV) versus pore volume (PV) injected for the first five cycles for the WAG and SAG injections. The liquid slugs are colored dark green for the SAG and dark blue for the WAG, and the CO_2 slugs are colored light green for the SAG and light blue for the WAG (Figure 9.1). A Python script for smoothing was used to smooth the noise in the experimental laboratory data to be able to illustrate the shape and locate trends in the data (described in section 7.5.3). Based upon the experimental procedure, the first two cycles were pure WAG cycles for all experiments (Figure 9.1, vertical red line). For both the SAG and WAG, there was a minor increase in apparent viscosity of ~2 cP but stable foam was not generated because of the lack of foaming agent in the first two cycles. In the SAG, after the injection of two surfactant solution slugs, the apparent viscosity in the fourth CO_2 slug increased to 3.1 cP, indicating foam generation (Hirasaki & Lawson, 1985).

In Figure 9.1, the apparent viscosity decreased during injection of first three surfactant slugs, whereas the apparent viscosity increased during the CO_2 slugs. This may indicate foam more readily generating in a drainage-like process (Kovscek & Radke, 1993). However, during the injection of the fourth surfactant slug in the SAG injection, this trend had changed, and there was an increase in the apparent viscosity during both the surfactant and the CO_2 slugs. The increase in apparent viscosity for both slugs may be related to continual foam generation due local fluctuations in capillary pressure during drainage and imbibition processes. However, it may also be related to pressure fluctuations from changing injection pumps between the CO_2 and aqueous phase. Nonetheless, these results indicate that foam was generated in the SAG once surfactant was introduced.
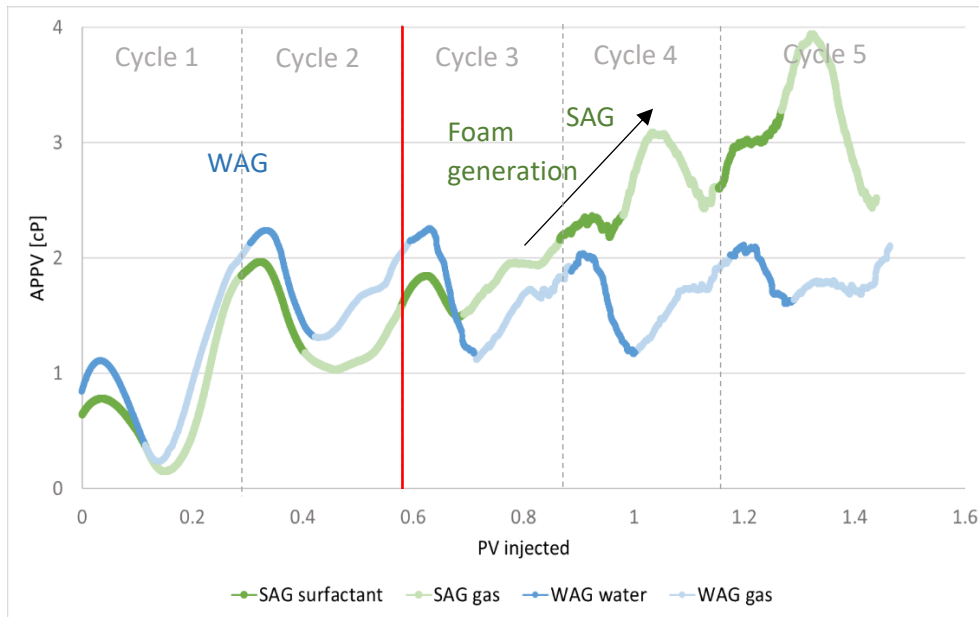
Figure 9.1 Apparent viscosity (APPV) versus pore volume (PV) injected for the first five cycles of baseline WAG and SAG. The red vertical line denotes the transition between the cycles injected with and without surfactant solution. The grey dashed lines indicate the transition between the individual WAG/SAG cycles.

Figure 9.2 shows apparent viscosity (APPV) versus pore volume (PV) injected for the complete 12 cycles for the baseline WAG and SAG injection. During the WAG injection, the apparent viscosity increased to 2.4 cP due to a reduced CO_2 relative permeability in the presence of high water saturation in a WAG process (Lake, 2010). Therefore, 2.4 cP was the foam generation limit for comparison to the SAG experiments. As in Figure 9.1, the SAG injection had a continuing trend of increasing apparent viscosity for each slug injected. This was the result of a foam bank moving further into the core, as well as the generation of more foam as the injection of new cycles continued. The peak apparent viscosity for the total injection was measured to be 146 cP for the SAG. It was measured during the peak of the last CO_2 slug of 1 PV of continuous CO_2 which dried out the foam after this point. The graphed injection showed no signs of reaching steady-state, hence, the maximum apparent viscosity potential of the foam system was most likely at a higher point. The half-life of the system was measured from the peak of the graph to the time it took for the apparent viscosity to reach half the value of the peak apparent viscosity. For the SAG injection, the apparent viscosity had halved its value after 0.09 PV injected (Figure 9.2, black dots).
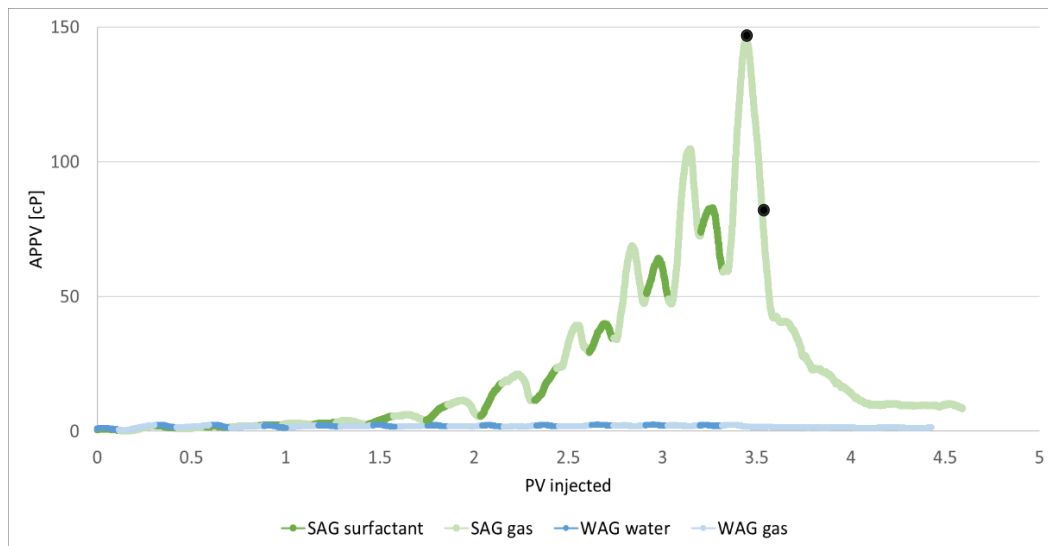
Figure 9.2 Apparent viscosity (APPV) versus pore volume (PV) injected during unsteady-state WAG and SAG injections. Both injections were performed with a gas fraction of 0.60 and an injection rate of 4 ft/day. Surfactant concentration for the SAG injection was 5000 ppm. Black dots mark the placement for the half-life calculation.

9.2 The Effect of Gas Fraction

The next set of experiments evaluated the influence of gas fraction on foam generation, strength, and stability during SAG injection. Gas fractions of 0.60 and 0.70 were tested and compared. For each gas fraction, the injection rate and surfactant concentration were also varied, one by one, to evaluate their influence on the foam behavior. For Section 9.2.1, the surfactant concentration was 5000 ppm and the injection rate 4 ft/day, for Section 9.2.2 the surfactant concentration was 2500 ppm and the injection rate 4 ft/day, and for Section 9.2.3, the surfactant concentration was 5000 ppm and the injection rate 8 ft/day. The system temperature was set at 40°C and the pressure to 200 bar, and the same core was used for all SAG injections (described in Section 7.1).

9.2.1 The Effect of Gas Fraction with a Surfactant Concentration of 5000 ppm and an Injection Rate of 4 ft/day

Figure 9.3 shows apparent viscosity (APPV) versus pore volume (PV) injected for the first five SAG cycles at a gas fraction of 0.60 (green curve) and 0.70 (orange curve). The surfactant slugs are shown as a dark shade, whereas the CO_2 slugs are shown as a light shade. The surfactant concentration was 5000 ppm and the injection rate was 4 ft/day for both experiments. The red lines in Figure 9.3 indicate when surfactant solution was injected. The size of the surfactant slugs was kept the same, but the size of the CO_2 slugs was changed to achieve the desired gas fraction.

The SAG injection with the gas fraction of 0.70 (Figure 9.3, orange curve) generated foam faster than the SAG injection with a gas fraction of 0.60 (Figure 9.3, green curve) based upon the increase in apparent viscosity to 5.2 cP, as soon as surfactant solution was injected (0.6 PV injected). The maximum apparent viscosity for the first five cycles was measured to be 3.9 cP for the 0.60 gas fraction and 30.1 cP for the 0.70 gas fraction. Thus, the SAG with a 0.70 gas fraction generated a stronger foam with less pore volume injected.
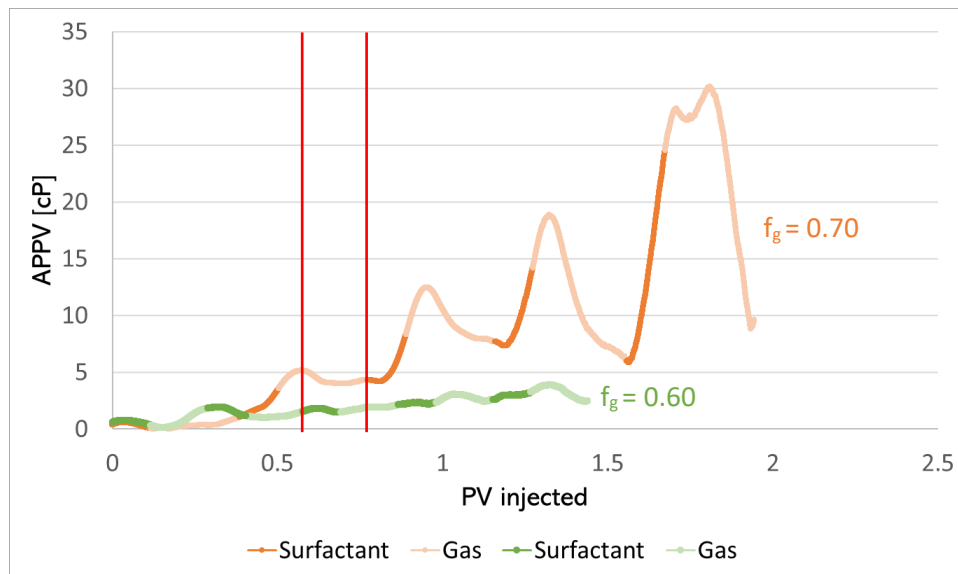
Figure 9.3 Apparent viscosity (APPV) versus pore volume (PV) injected for the first five cycles of SAG injections with a gas fraction of 0.60 (orange curve) and 0.70 (green curve), with a surfactant concentration of 5000 ppm and an injection rate of 4 ft/day. The red vertical lines denotes the transition between the cycles injected with and without surfactant solution.

Figure 9.4 shows apparent viscosity (APPV) versus pore volume (PV) injected for the complete 12 cycles for the 0.70 gas fraction SAG (orange curve) and the 0.60 gas fraction SAG (green curve). The peak apparent viscosity for the 0.60 gas fraction was 146 cP, whereas the 0.70 gas fraction had a peak apparent viscosity of 241.1 cP, a 65.1% increase in foam strength with the same amount of surfactant solution injected. Thus, continuing the trend for generation of a stronger foam as seen for the first five slugs for the 0.70 gas fraction. Throughout the injection, the apparent viscosity had a continuing increase for both injections, which was the result of the generation of additional foam as well as movement of the foam bank further into the core for each new cycle injected. The 0.70 gas fraction SAG had a stabilizing fluctuation in apparent viscosity towards the end of the experiment, during the injection of the last two cycles. It might be an indication of steady-state injection where the foam generates and decays at the same rate. The 0.60 gas fraction SAG did not experience the same decrease in the slope trend for the apparent viscosity, which made it difficult to determine at what value of apparent viscosity it would have stabilized at if the injection was continued further.

The injected cycles formed a maximum and a minimum apparent viscosity point in between each new cycle. For the 0.60 gas fraction injection, the gap between the max and min values was shorter than it was for the 0.70 gas fraction. This might be an indication of a more stable foam for the 0.60 gas injection, thus, forming a higher resistance in the foam to collapse and decrease the effect of dry-out, which decrease the fall in apparent viscosity more than for the 0.70 gas fraction SAG. As previously mentioned, the 0.60 gas fraction SAG did not appear to stabilize for the fluctuations in the apparent viscosity, thus, the distance might have increased with further injection. The fluctuations might also have been the consequence of the pressure fall occurring when the injection pumps were switched in between phases.

The continuous injection of CO_2 at the end of the injection formed the tail-part (4.3 PV injected) of the flooding where foam was dried out. The half-life was measured (Figure 9.4, black dots) as the time it took the peak apparent viscosity value to dry out to half its value. This was calculated to comment on the foam stability in relation to decay in contact with pure CO_2. The half-life of the 0.60 gas fraction was measured to be at 0.09 PV injected while the 0.70 gas fraction reached half the peak

value at 0.14 PV injected of pure CO_2, which was 55.6% longer than for the 0.60 gas fraction injection. Thus, indicating a higher stability in the foam for the 0.70 gas fraction SAG.

Figure 9.4 Apparent viscosity (APPV) versus pore volume (PV) injected for SAG injection with gas fraction of 0.60 (green curve) and 0.70 (orange curve), both with a surfactant concentration of 5000 ppm and an injection rate of 4 ft/day. Black dots mark the areas for calculating the half-life of the foam.

9.2.2 The Effect of Gas Fraction with a Surfactant Concentration of 2500 ppm and an Injection Rate of 4 ft/day

Figure 9.5 shows apparent viscosity (APPV) versus pore volume (PV) injected for the first five cycles of SAG, at a gas fraction of 0.60 (yellow curve) and 0.70 (purple curve). The surfactant slugs are shown as a dark shade, whereas the CO_2 slugs are shown as a light shade. The surfactant concentration was 2500 ppm, and the injection rate was 4 ft/day for both injections. The red vertical lines in Figure 9.5 demonstrate when surfactant solution was injected. The size of the surfactant slugs was kept the same, but the size of the CO_2 slugs was altered to achieve the desired gas fraction.

The SAG injection with the gas fraction of 0.60 (Figure 9.5, yellow curve) generated weaker foam after the injection of five full cycles compared to the SAG with the gas fraction of 0.70 (Figure 9.5, purple curve) did after four cycles injected (1.4 PV injected), with an apparent viscosity of 4.2 cP and 4.9 cP, respectively. The maximum apparent viscosity for the first five cycles was measured to be 4.2 cP for the 0.60 gas fraction and 8.2 cP for the 0.70 gas fraction. Thus, the SAG with a gas fraction of 0.70 generated a stronger foam with the same amount of injected surfactant solution.

Figure 9.5 Apparent viscosity (APPV) versus pore volume (PV) injected for the first five cycles of SAG with a gas fraction of 0.60 (yellow curve) and 0.70 (purple curve) with a surfactant concentration of 2500 ppm and an injection rate of 4 ft/day. The red vertical lines denote the transition in the SAG injections where surfactant solution was injected.

Figure 9.5 shows apparent viscosity (APPV) versus pore volume (PV) injected for the 12 SAG cycles for the 0.60 gas fraction SAG (yellow curve) and the 0.70 gas fraction SAG (purple curve). The peak apparent viscosity for the 0.60 gas fraction was 204.3 cP, whereas the 0.70 gas fraction had a peak apparent viscosity of 232.1 cP, an increase of 13.6% in foam strength with the same amount of surfactant solution injected. Even though the 0.70 gas fraction generated foam stronger foam quicker than the 0.60 gas fraction, the flooding was barely stronger than the 0.60 gas fraction further into the injection. Both injections had a continuing increasing apparent viscosity throughout the full SAG injection, which was a result of the generation of more foam and the movement of the foam bank further into the core.

The interval between the maximum and minimum values formed in each injected cycle had a larger distance for the 0.70 gas fraction SAG than it had for the 0.60 gas fraction SAG. During the 11th SAG cycle, the 0.70 gas fraction had a decrease in apparent viscosity of 138.9 cP, while the 0.60 gas fraction had a decrease of 89.8 cP for the same cycle. Which might indicate a lower stability and less resistance to decay in the foam generated by the 0.70 gas fraction SAG. The fluctuations could also have been the result of the pump switches in between the two different fluid injections.

The continuous injection of CO_2 during cycle 12 at the end of the injection, formed the tail-end of the flooding where foam was dried out. The half-life was measured (Figure 9.6, black dots) for the time it took the peak apparent viscosity value to reach half its peak value. This was calculated to comment on the foam stability in relation to pure CO_2 decay. The half-life was measured to be 0.11 PV injected for the 0.60 gas fraction while it was 0.10 PV injected for the 0.70 gas fraction, which was 9.1% less than for the 0.60 gas fraction injection. Thus, indicating a slightly more unstable foam for the SAG with a gas fraction of 0.70, supporting the observations discussed over.
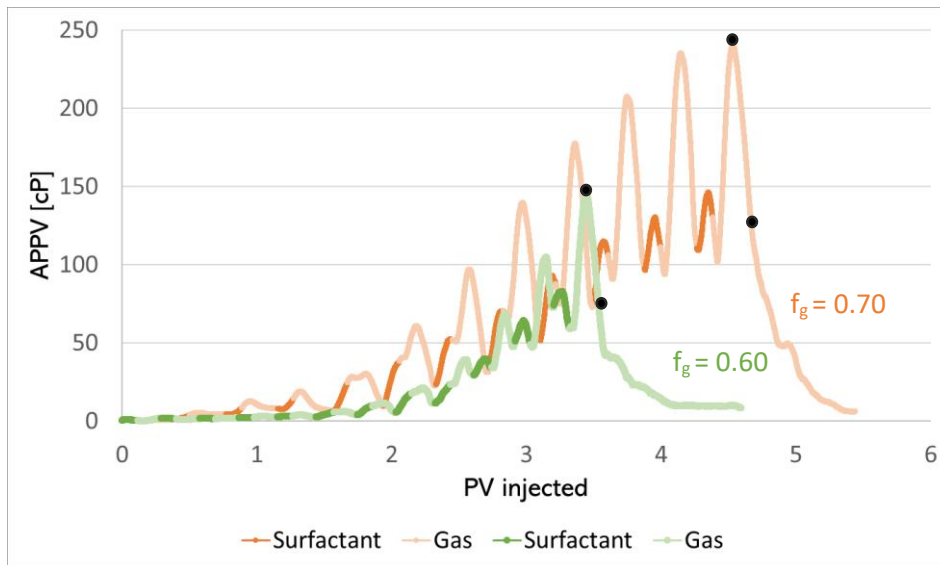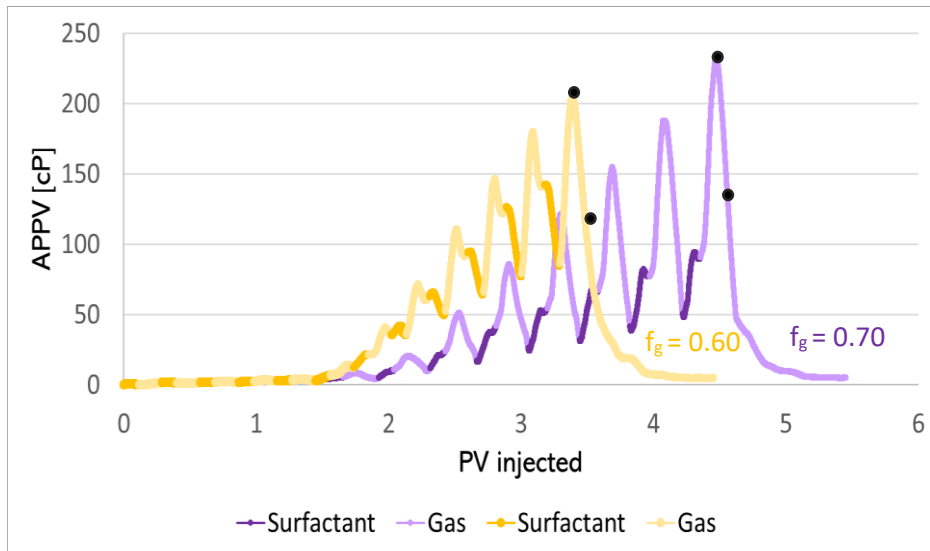
Figure 9.6 Apparent viscosity (APPV) versus pore volume (PV) injected for the SAG injections with a gas fraction of 0.60 (yellow curve) and 0.70 (purple curve), both with a surfactant concentration of 2500 ppm and an injection rate of 4 ft/day. Black dots mark the half-life calculation of the foam.

9.2.3 The Effect of Gas Fraction with a Surfactant Concentration of 5000 ppm and an Injection Rate of 8 ft/day
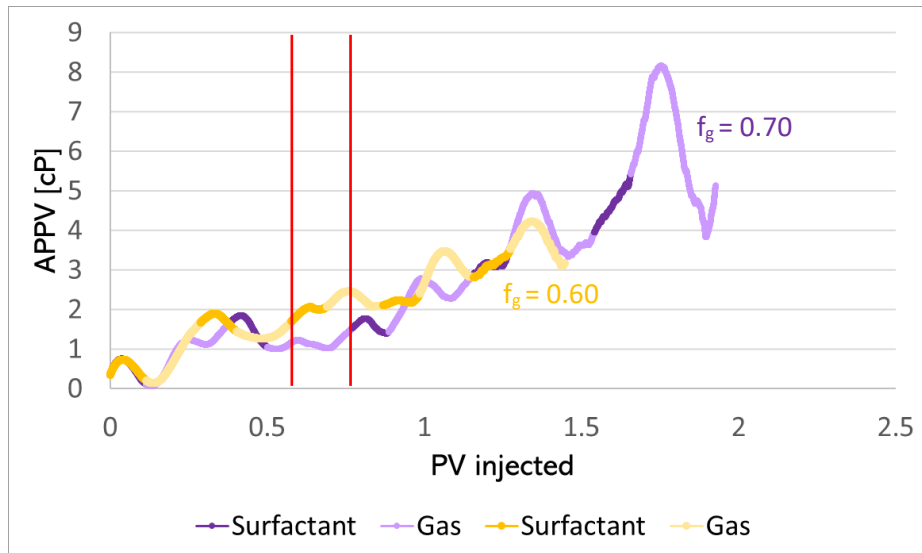
Figure 9.7 shows apparent viscosity (APPV) versus pore volume (PV) injected for the first five SAG cycles with a gas fraction of 0.60 (pink curve) and 0.70 (red curve). The surfactant slugs are shown as a dark shade, whereas the CO_2 slugs are shown as a light shade. The surfactant concentration was 5000 ppm and the injection rate 8 ft/day for both experiments. The red lines in Figure 9.7 marks the slug which first injected surfactant solution. The size of the surfactant slugs was kept the same, but the size of the CO_2 slugs was changed to achieve the desired gas fraction.

Both the SAG injection with a gas fraction of 0.60 (Figure 9.7, pink curve) and the SAG injection with a gas fraction of 0.70 (Figure 9.7, red curve) generated foam during the injection of the fifth cycle (1.4 PV injected and 1.8 PV injected, respectively). The maximum apparent viscosity for the first five cycles was measured to be 11.9 cP for the 0.60 gas fraction and 13.1 cP for the 0.70 gas fraction. Thus, indicating a negligible difference in foam strength for the two SAG cases during the injection of the fifth CO_2 slug for both injections.

51

Figure 9.7 Apparent viscosity (APPV) versus pore volume (PV) injected for the first five cycles of SAG injection with a gas fraction of 0.60 (pink curve) and 0.70 (red curve), with a surfactant concentration of 5000 ppm and an injection rate of 8 ft/day. The red vertical lines denote the transition between the cycles injected with and without surfactant solution.

Figure 9.8 shows apparent viscosity (APPV) versus pore volume (PV) injected for the complete 12 cycles for the 0.60 gas fraction SAG (pink curve) and the 0.70 gas fraction SAG (red curve). The peak apparent viscosity for the 0.60 gas fraction was 168.1 cP, whereas the 0.70 gas fraction had a peak apparent viscosity of 166.4 cP, a decrease of 1.0% in foam strength with the same amount of surfactant solution injected, indicating a negligible strength difference between the two. During the injection, the apparent viscosity continued to increase for each cycle injected for both injections, which was the result of additional foam being generated and the moving foam bank further into the core as new cycles were injected. Both the 0.60 and the 0.70 gas fraction SAG had a starting flattening trend of the apparent viscosity towards the end of the experiment, during the last few cycles injected. Thus, indicating a stabilization of the generation and decay of foam in the two systems.

The distance formed between the maximum and minimum values in the individual cycles was greater for the 0.70 gas fraction SAG than it was for the 0.60 gas fraction SAG. During the injection of the 11th cycle, the 0.70 gas fraction formed a distance between the apparent viscosity max and min points of 84.1 cP, whereas it was 50.1 cP for the 0.60 gas fraction during the same cycle. This may indicate a lower foam stability as a result of less resistance in the foam to pure CO_2 for the 0.70 gas fraction SAG. The trend could also be the result of the switching between injection pumps between each of the injected phases.

The continuous injection of CO_2 at the end of the 12th SAG cycle formed the tail-section of the flooding where foam was dried out (3.4 and 4.5 PV injected, for the 0.60 and 0.70 gas fraction, respectively). The half-life was measured (Figure 9.8, black dots) as the distance from the peak apparent viscosity value to the point where the peak had halved in value during the dry-out of the foam. This was calculated to comment on the foam stability in relation to pure CO_2 decay. The half-life of the 0.60 gas fraction was after 0.18 PV of pure CO_2 had been injected while it was after 0.12 PV injected for the 0.70 gas fraction, 33.3% less injected CO_2 than for the 0.60 gas fraction. Thus,

indicating a weaker foam for the SAG with a gas fraction of 0.70, supporting the observations discussed over.

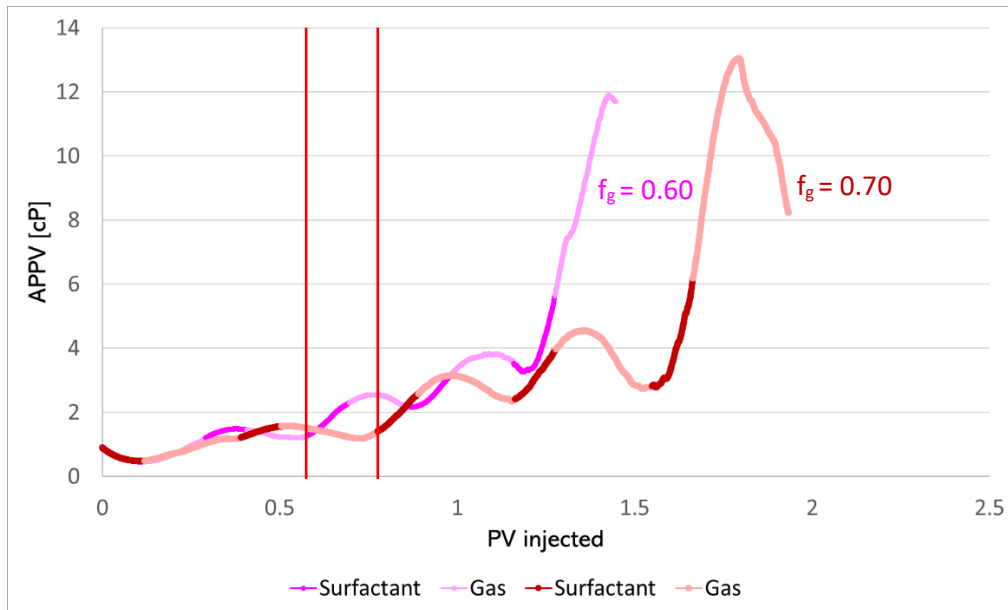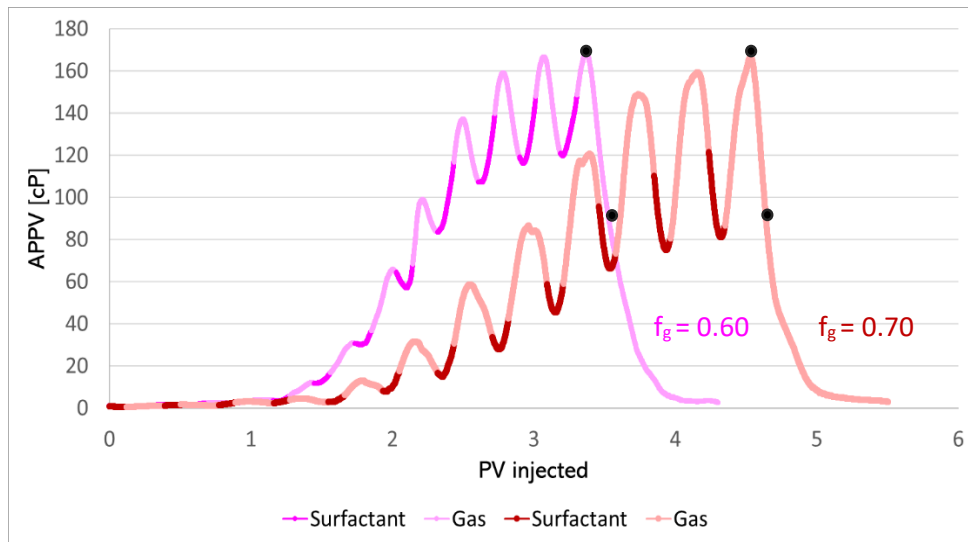

Figure 9.8 Apparent viscosity (APPV) versus pore volume (PV) injected for the SAG injections with a gas fraction of 0.60 (pink curve) and 0.70 (red curve), both with a surfactant concentration of 5000 ppm and an injection rate of 8 ft/day. Black dots indicate the locations on the graphs for calculating half-life of the foam.

9.3 The Effect of Surfactant Concentration

The next set of experiments evaluated the influence of surfactant concentration on foam generation, strength, and stability during SAG injection. Surfactant concentrations of 2500 ppm and 5000 ppm were tested and compared. For each surfactant concentration, the gas fraction was also varied to evaluate its influence on foam behavior. For Section 9.3.1, the gas fraction was 0.60 and the injection rate 4 ft/day, and for Section 9.3.2, the gas fraction was 0.70 and the injection rate 4 ft/day. The system temperature was set at 40°C and the pressure to 200 bar, and the same core was used for all SAG injections (described in Section 7.1).

9.3.1 The Effect of Surfactant Concentration with a Gas Fraction of 0.60 and an Injection Rate of 4 ft/day

Figure 9.9 shows apparent viscosity (APPV) versus pore volume (PV) injected for the first five cycles of SAG with a surfactant concentration of 2500 ppm (yellow curve) and 5000 ppm (green curve). The surfactant slugs are shown as a dark shade, whereas the CO_2 slugs are shown as a light shade. The gas fraction was 0.60 and the injection rate was 4 ft/day for both SAG injections. The red line in Figure 9.9 indicates when surfactant solution was injected, and the grey dashed lines indicates the transition between the individual SAG cycles.

The SAG injection with the surfactant concentration of 2500 ppm (Figure 9.9, yellow curve) generated foam at about the same rate as the SAG injection with a surfactant concentration of 5000 ppm (Figure 9.9, green curve) based upon the similar increase in apparent viscosity with the same amount of pore volume injected. The maximum apparent viscosity for the first five cycles was measured to be 4.2 cP for the 2500 ppm surfactant concentration and 3.9 cP for the 5000 ppm surfactant concentration. Thus, indicating a negligible difference in foam strength for the two injections at 1.4 PV injected.

Figure 9.9 Apparent viscosity (APPV) versus pore volume (PV) injected for the first five cycles of SAG injection for surfactant concentrations 2500 ppm (yellow curve) and 5000 ppm (green curve), with a gas fraction 0.60 and an injection rate of 4 ft/day. The red vertical line denotes the transition between the cycles injected with and without surfactant solution, and the grey dashed lines indicates the transition between the individual SAG cycles.

Figure 9.10 shows apparent viscosity (APPV) versus pore volume (PV) injected for the complete 12 cycles for the 2500 ppm surfactant concentration (yellow curve) and the 5000 ppm surfactant concentration (green curve). The peak apparent viscosity for the 2500 ppm surfactant concentration was 204.3 cP, whereas the 5000 ppm surfactant concentration had a peak apparent viscosity of 146.0 cP, a 39.9% increase in foam strength for the 2500 ppm surfactant concentration SAG with the same fluid volume injected. During the injection, the apparent viscosity had a continuing increase for each cycle injected for both SAG injections, which was the result of a constant generation of more foam and the foam bank moving further into the core as new SAG cycles were injected. The 2500 ppm surfactant concentration SAG increased in apparent viscosity at a higher rate than the 5000 ppm surfactant concentration SAG from the injection of 7th slug (1.7 PV injected) and onwards, thus generating a stronger foam from that point of the injection.

The distance formed between the maximum and minimum values in the individual cycles was greater for the 2500 ppm surfactant concentration than it was for the 5000 ppm surfactant concentration. For the 11th SAG slug, the distance between the apparent viscosity max and min values was 99.3 cP for the 2500 ppm surfactant concentration, while it was 55.3 cP for the 5000 ppm surfactant concentration during the same cycle. Which may be an indication of less stability for the foam in the 2500 ppm surfactant concentration SAG injection. It might also have been the result of the pressure loss caused by switching between pumps when changing between the fluid phases.

The continuous injection of CO_2 at the end of the injection during the 12th slug (3.4 PV injected), formed the tail-end of the flooding where foam was dried out. The half-life was measured (Figure 9.10, black dots) from the peak apparent viscosity value to the half point of the peak value and was calculated to comment on the foam stability in relation to decay in contact with pure CO_2. The half-life of the 2500 ppm surfactant concentration was measured to be after 0.11 PV injected while the 5000 ppm surfactant solution reached half the peak value after 0.09 PV injected of pure CO_2. Thus, indicating a slightly weaker foam for the SAG with a surfactant concentration of 5000 ppm.

Figure 9.10 Apparent viscosity (APPV) versus pore volume (PV) injected for the SAG injections with a surfactant concentration of 2500 ppm (yellow curve) and 5000 ppm (green curve), both with a gas fraction of 0.60 and an injection rate of 4 ft/day. Black dots indicate the areas for calculating the half-life of the foam.

9.3.2 The Effect of Surfactant Concentration with a Gas Fraction of 0.70 and an Injection Rate of 4 ft/day

Figure 9.11 shows apparent viscosity (APPV) versus pore volume (PV) injected for the first five SAG cycles with a surfactant concentration of 2500 ppm (purple curve) and 5000 ppm (orange curve). The surfactant slugs are shown as a dark shade, whereas the CO_2 slugs are shown as a light shade. The gas fraction was 0.70 and the injection rate was 4 ft/day for both experiments. The red line in Figure 9.9 indicates when surfactant solution was injected in the system, and the grey dashed lines indicates the transition between the individual SAG cycles.

The SAG injection with the surfactant concentration of 5000 ppm (Figure 9.11, orange curve) generated foam faster than the SAG injection with a surfactant concentration of 2500 ppm (Figure 9.11, purple curve) based upon the increase in apparent viscosity to 12.4 cP as soon as surfactant solution was injected (1.0 PV injected). The maximum apparent viscosity for the first five cycles was measured to be 8.2 cP for the 2500 ppm surfactant concentration and 30.1 cP for the 5000 ppm surfactant concentration. Thus, indicating the generation of significantly stronger foam for the SAG with the 5000 ppm surfactant concentration with the same pore volume of fluids injected (1.4 PV injected).
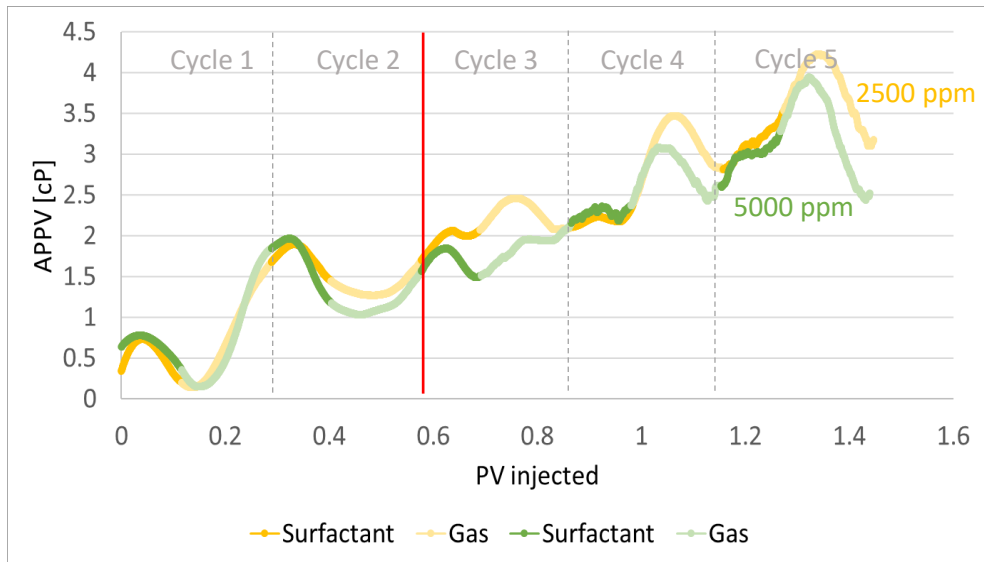
Figure 9.11 Apparent viscosity (APPV) versus pore volume (PV) injected for the first five cycles of SAG injection with surfactant concentrations of 2500 ppm (purple curve) and 5000 ppm (orange curve), with a gas fraction of 0.70 and an injection rate of 4 ft/day. The red vertical line denotes the transition between the cycles injected with and without surfactant solution, and the grey dashed lines indicates the transition between the individual SAG cycles.

Figure 9.12 shows apparent viscosity (APPV) versus pore volume (PV) injected for the complete 12 injected cycles for the 2500 ppm surfactant concentration (purple curve) and the 5000 ppm surfactant concentration (orange curve). The peak apparent viscosity for the 2500 ppm surfactant concentration was 232.1 cP, whereas the 5000 ppm surfactant concentration had a peak apparent viscosity of 241.1 cP, a 3.9% increase in foam strength with the same volume of fluids injected, suggesting a negligible difference in end-point foam strength. The average apparent viscosity, however, lists the overall strength of the 5000 ppm surfactant concentration SAG as higher due to a 67.2% overall increase compared to the average apparent viscosity for the 2500 ppm surfactant solution SAG. During the injection, the apparent viscosity had a steady increase for each new cycle injected for both injections, which was the product of the generation of additional foam and the foam bank moving further into the core.

The distance formed between the maximum and minimum points in between the individual slugs was large for both injections. During the 11th SAG cycle, the distance between min and max apparent viscosity was 148.3 cP the 2500 ppm surfactant concentration, while it was 141.9 cP for the 5000 ppm surfactant concentration during the same cycle. Which may be an indication of a lower stability for the foam in both injections. Though, it might also have been the result of the pressure loss from switching the pumps between injection of surfactant solution and CO_2.

The tail-part of the flooding was formed by the continuous injection of CO_2 during the end of the 12th cycle, which dried out the foam. The half-life was measured (Figure 9.12, black dots) from the peak apparent viscosity to the midpoint of the decrease in apparent viscosity during the foam decay. The half-life of the 2500 ppm surfactant concentration was measured to be after 0.10 PV injected while it was after 0.14 PV injected for the 5000 ppm surfactant. Which might be an indication of less stability for the 2500 ppm surfactant concentration.
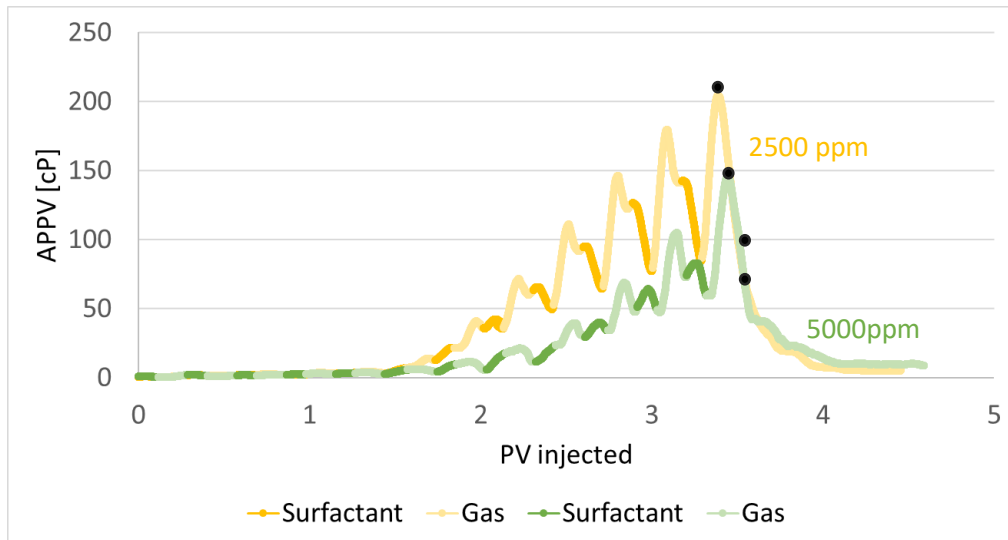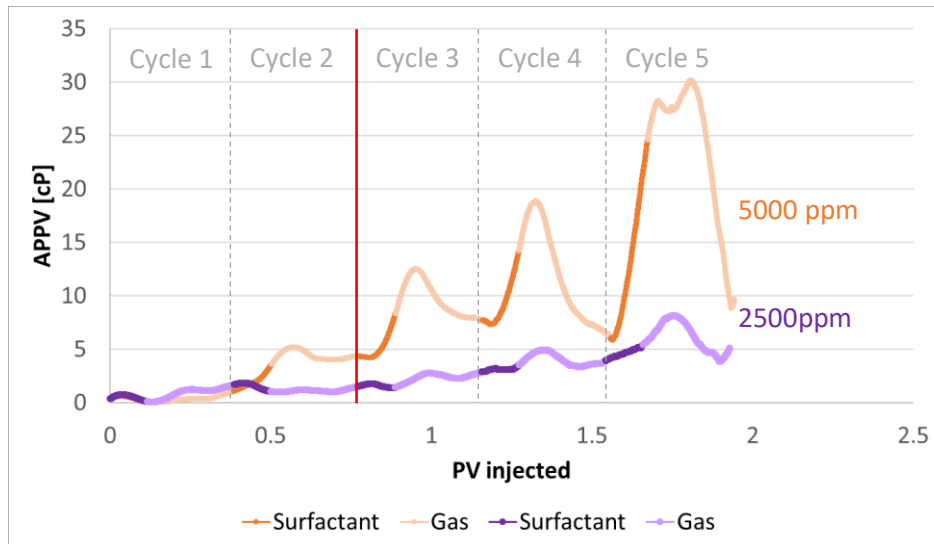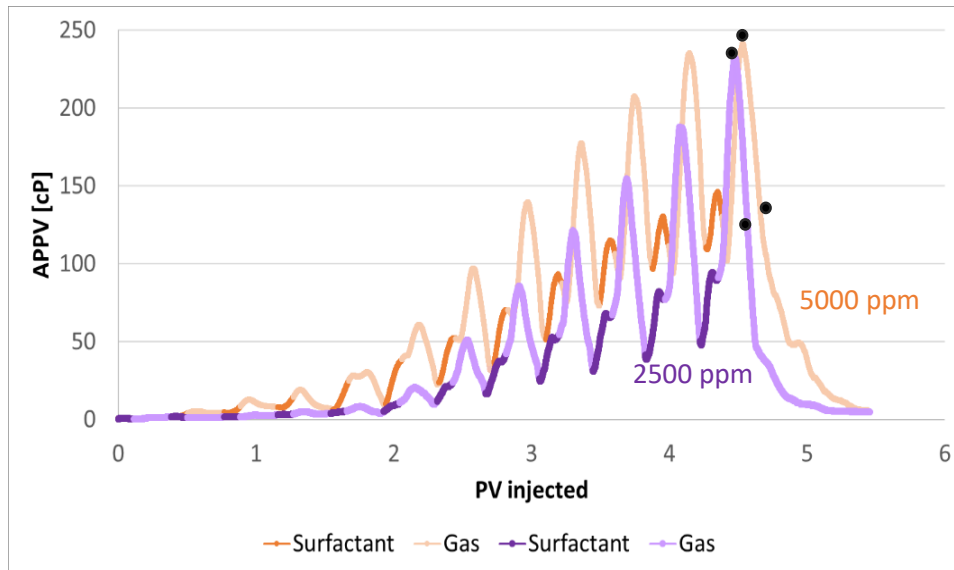
Figure 9.12 Apparent viscosity (APPV) versus pore volume (PV) injected for SAG injections with surfactant concentration of 2500 ppm (purple curve) and 5000 ppm (orange curve), both with a gas fraction of 0.70 and an injection rate of 4 ft/day. Black dots indicate the areas for calculating the half-life of the foam.

9.4 The Effect of Injection Rate

The next set of experiments evaluated the influence of injection rate on foam generation, strength, and stability during SAG injection. Injection rates of 4 ft/day and 8 ft/day were tested and compared. For each injection rate, the gas fraction was also varied. For Section 9.4.1, the gas fraction was 0.60 and the surfactant concentration 5000 ppm, and for Section 9.4.2, the gas fraction was 0.70 and surfactant concentration 5000 ppm. The system temperature was set at 40°C and the pressure to 200 bar, and the same core was used for all SAG injections (described in Section 7.1).

9.4.1 The Effect of Injection Rate with a Gas Fraction of 0.60 and a Surfactant Concentration of 5000 ppm

Figure 9.13 shows apparent viscosity (APPV) versus pore volume (PV) injected for the first five SAG cycles at an injection rate of 4 ft/day (green curve) and 8 ft/day (pink curve). The surfactant slugs are shown as a dark shade and the CO_2 slugs are shown as a light shade. The gas fraction was 0.60 and the surfactant concentration 5000 ppm for both experiments. The red line in Figure 9.13 indicates when surfactant solution was injected, and the grey dashed lines indicates the transition between the individual SAG cycles.

The SAG injection with the injection rate of 8 ft/day (Figure 9.13, pink curve) generated a stronger foam earlier than the SAG injection with the injection rate of 4 ft/day (Figure 9.13, green curve) based upon the steep increase in apparent viscosity during the injection of cycle five (1.4 PV injected). The maximum apparent viscosity for the first five cycles was measured to be 3.9 cP for the 4 ft/day injection rate and 11.9 cP for the 8 ft/day injection rate. Thus, indicating the 8 ft/day injection rate generating a considerably stronger foam with the same pore volume of fluids injected (1.4 PV injected).

Figure 9.13 Apparent viscosity (APPV) versus pore volume (PV) injected for the first five cycles of SAG for injection rate 4 ft/day (green curve) and 8 ft/day (pink curve), with a gas fraction 0.60 and a surfactant concentration of 5000 ppm. The red vertical line denotes the transition between the cycles injected with and without surfactant solution, and the grey dashed lines indicates the transition between the individual SAG cycles.

Figure 9.14 shows apparent viscosity (APPV) versus pore volume (PV) injected for the complete 12 cycles for the SAG injection with an injection rate of 4 ft/day (green curve) and 8 ft/day (pink curve). The peak apparent viscosity for the 4 ft/day injection was 146.0 cP, whereas the 8 ft/day injection had a peak apparent viscosity of 168.1 cP, indicating a slightly stronger foam in the peak point with the same quantity of fluids injected. The overall apparent viscosity was 125.6% higher in average apparent viscosity for the 8 ft/day injection, suggesting that the overall generation of foam was significantly stronger during the injection of the 12 cycles. The apparent viscosity had a steady increase for each new SAG cycle injected for both injections, which was the result of a constant generation of additional foam and the movement of the foam bank further into the core. The 8 ft/day SAG injection had a starting stabilization of the fluctuation in apparent viscosity towards the end of the experiment, during the injection of the last two cycles. Whereas the 4 ft/day SAG injection did not experience the same decrease in gradient of the slope for the apparent viscosity, which makes the peak value of the graph highly uncertain.

The tail-part of the flooding was the result continuous injection of CO_2 during the end of the 12th SAG cycle (3.4 PV injected), which dried out the foam. The half-life was measured (Figure 9.14, black dots) from the peak apparent viscosity to the apparent viscosity midpoint of the peak, during the decay of foam. The half-life of the 4 ft/day injection was measured to be 0.9 PV injected while the 8 ft/day injection reached half its peak value after 0.18 PV injected of pure gas. Thus, indicating the generation of a significantly stronger foam for the 8 ft/day SAG injection.

Figure 9.14 Apparent viscosity (APPV) versus pore volume (PV) injected for SAG injections with an injection rate of 4ft/day (green curve) and 8 ft/day (pink curve), both with a gas fraction of 0.60 and a surfactant concentration of 5000 ppm. Black dots indicate the areas for calculating the half-life of the foam.

9.4.2 The Effect of Injection Rate with a Gas Fraction of 0.70 and a Surfactant Concentration of 5000 ppm

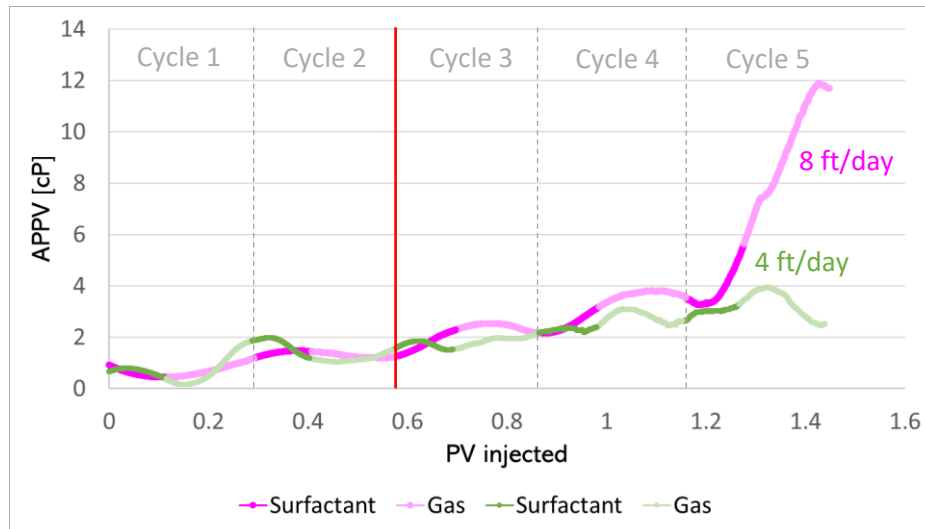Figure 9.15 shows apparent viscosity (APPV) versus pore volume (PV) injected for the first five SAG cycles at an injection rate of 4 ft/day (orange curve) and 8 ft/day (red curve). The surfactant slugs are shown as a dark shade, whereas the CO_2 slugs are shown as a light shade. The gas fraction was 0.70 and the surfactant concentration was 5000 ppm for both experiments. The red vertical line in Figure 9.13 indicates the injection time for the surfactant solution, and the grey dashed lines indicate the transition between the individual SAG cycles.

The SAG injection with the injection rate of 4 ft/day (Figure 9.15, orange curve) generated foam quicker than the SAG injection with the injection rate of 8 ft/day (Figure 9.15, red curve) based upon the increase in apparent viscosity to 12.4 cP as soon as surfactant was injected in the system (0.8 PV injected). The maximum apparent viscosity for the first five cycles was measured to be 30.1 cP for the 4 ft/day injection rate and 12.1 cP for the 8 ft/day injection rate. Thus, indicating the generation of a considerably stronger foam for the SAG with the injection rate of 4 ft/day with the same volume of fluids injected (1.9 PV injected).

Figure 9.15 Apparent viscosity (APPV) versus pore volume (PV) injected for the first five cycles of SAG injections with an injection rate of 4 ft/day (orange curve) and 8 ft/day (red curve), both with a gas fraction of 0.70 and a surfactant concentration of 5000 ppm. The red vertical line denotes the transition between the cycles injected with and without surfactant solution, and the grey dashed lines indicates the transition between the individual SAG cycles.

Figure 9.16 shows apparent viscosity (APPV) versus pore volume (PV) injected for the complete 12 cycles of the SAG injection with an injection rate of 4 ft/day (orange curve) and 8 ft/day (red curve). The peak apparent viscosity for the 4 ft/day injection was 241.1 cP, whereas the 8 ft/day injection had a peak apparent viscosity of 166.4 cP, a decrease of 31% in foam strength with the same quantity of fluids injected. The apparent viscosity was increasing throughout the injection for both SAG injections due to the constant generation of additional foam and movement of the foam bank further into the core during the injection of new SAG cycles. Both injections had a starting stabilization of the fluctuation in apparent viscosity towards the end of the experiment, during the last few injected cycles.

The distance formed in between the maximum and minimum apparent viscosity points for the individual cycles was larger for the 4 ft/day injection than it was for the 8 ft/day injection. During the injection of the 11th SAG cycle, the distance between the max and min apparent viscosity was 141.9 cP the 4 ft/day injection, while it was 83.3 cP for the 8 ft/day injection during the same cycle. Which might be an indication of a higher stability in the foam generated in the 8 ft/day SAG injection. Though, it might also have been the result of pressure loss from switching the pumps between the injection of surfactant solution and CO_2.

The tail-part of the flooding was formed by the continuous injection of CO_2 during the last SAG cycle of the injection (4.5 PV injected), which dried out the foam. The half-life was measured (Figure 9.16, black dots) as the time it took the peak apparent viscosity value to dry out to half its value. The half-life of the 4 ft/day injection was measured to be 0.14 PV injected while the 8 ft/day injection reached half its peak value after 0.12 PV injected of pure CO_2. Thus, indicating a slightly higher resistance to pure CO_2 in the 4 ft/day injection.
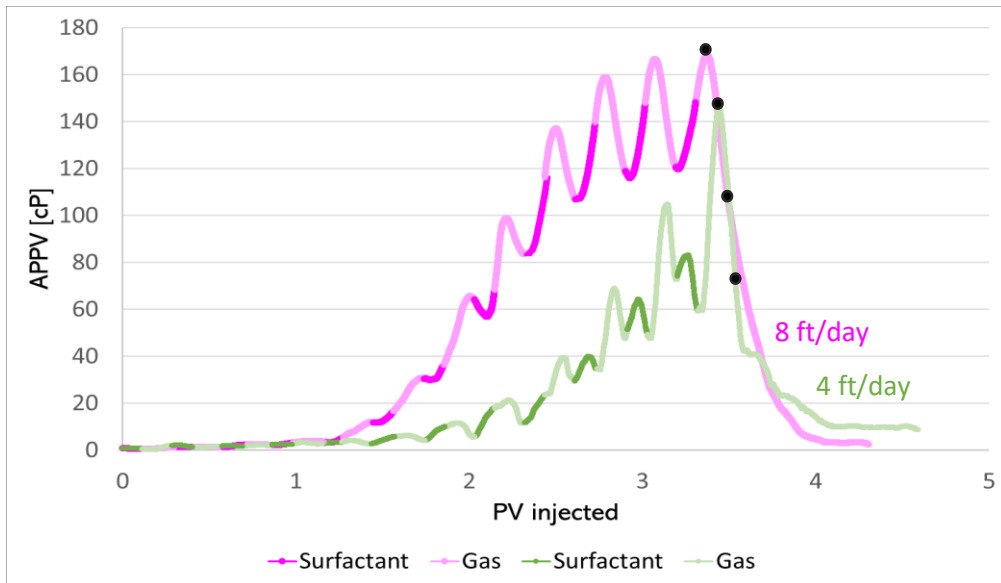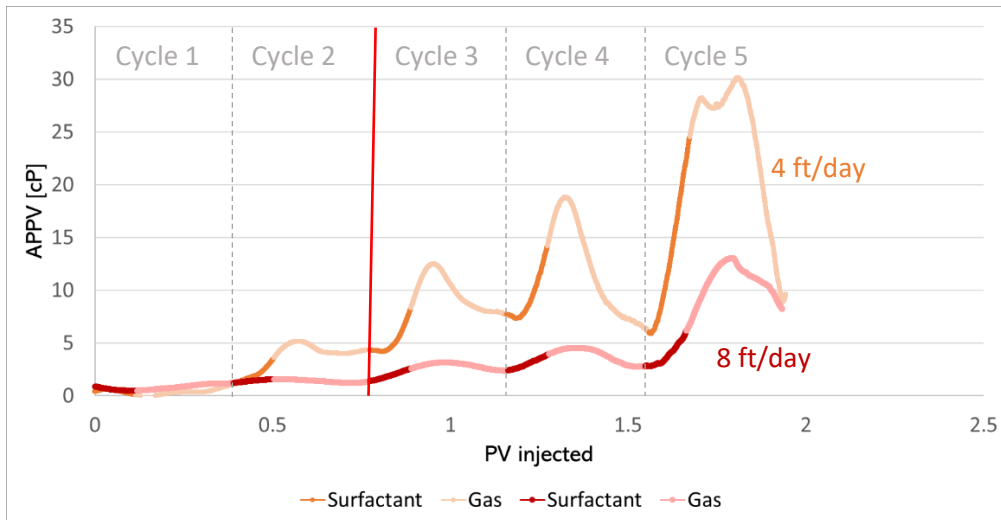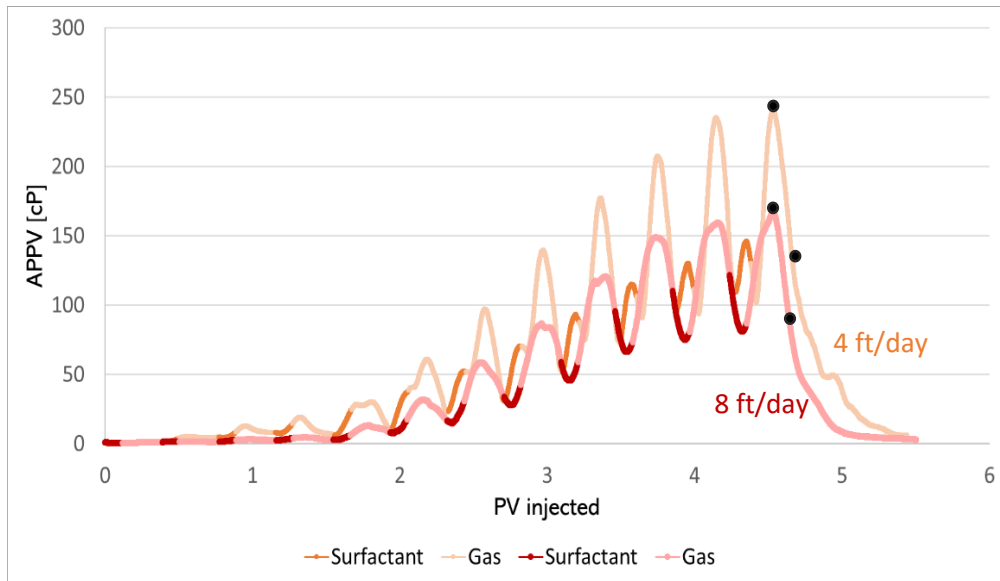
Figure 9.16 Apparent viscosity (APPV) versus pore volume (PV) injected for SAG injection with injection rates of 4 ft/day (orange curve) and 8 ft/day (red curve), both with a gas fraction of 0.70 and a surfactant concentration of 5000 ppm. Black dots indicate the areas for calculating the half-life of the foam.

10. Numerical Sensitivity Study

The cross-sectional model of the pilot injector/producer well-pair of the East Seminole field was used to evaluate the performance of different experimentally derived foam models. The main objective was to test the laboratory derived foam models sensitivity to foam generation, CO_2 mobility reduction and sweep efficiency at field-scale. In addition, the effect of residual oil on foam was evaluated. Each sensitivity case has been listed in Table 8.2.

10.1 Baseline WAG and Base SAG

To establish a baseline and confirm foam generation, a baseline WAG was set up and compared to a base SAG simulation case. As described in section 8.5.1, the two models were set up in the exact same way except for the SAG case injecting surfactant solution in the liquid phase, rather than only water.

10.1.1 Foam Generation

Foam generation at the field-scale is often indicated by an increase in injection bottom hole pressure (BHP) due to reduction of CO_2 relative permeability which gives an increase of the viscosity in the CO_2 phase, as well as an increase in pressure from foam blocking high-permeable layers (Rossen, 1996). To verify generation of foam, the BHP in the injection well during SAG injection was compared to the baseline WAG. Figure 10.1 shows the BHP versus time for the injection well for the base SAG (green curve) and the baseline WAG (blue curve). A secondary x-axis showing PV injected is also included. The BHP for the base SAG started to increase right after the start of the pilot on May 23, 2019, after 0.011 PV injected, to 2483.2 psi, whereas the baseline WAG had a BHP of 2380.4 psi. The increase in BHP of the base SAG compared to the WAG indicated generation of foam. The continued injection of new SAG cycles indicated a further increase in the BHP for the base SAG, this was due to the generation of additional foam for every new SAG cycle injected, as well as the foam bank moving further into the reservoir thereby further increasing the pressure.

WAG also experienced a gradual increase in BHP as the alternating slugs reduced the relative permeability of CO_2 in the presence of higher saturation of water, and thereby improved the mobility ratio (Enick et al., 2012). It had a lower increase in pressure than the base SAG due to the lack of stable foam in the system.

The field experienced two shutdowns during the pilot injection, which have been included in the numerical model (Figure 10.1). The first shutdown occurred in between the injection of SAG cycle 8 and 9 (0.127 PV injected, Figure 10.1) on January 19, 2020, and lasted for 22 days. The second shutdown took place March 9, 2020, during the injection of SAG cycle 10 (0.134 PV injected, Figure 10.1) and lasted for 60 days. During the two shutdowns, the recorded BHP fell by 116.2 psi and 96.1 psi, respectively, for the base SAG. The reservoir pressure, however, increased during the two shutdowns due to the sudden stop in injection and production while still having movement of fluids in the system. This was the reason for the increase in pressure after resuming production.

For the total SAG injection, the peak BHP was 3112.4 psi at 0.147 PV injected, and 2429.4 psi for the baseline WAG at the same injection point, an increase of 28.1% for the base SAG, confirming a continued generation of foam for the injection. The peak BHP was also the injection point at which the response of the post-pilot WAG injection was observed, after 0.147 PV total had been injected. The 60-day post pilot decreased the BHP in the base SAG due to the lack of new supply of surfactants in the system as well as the changed injection scheme. At the end of the injection (September 1, 2020, 0.154 PV injected) the BHP had decreased by 355.3 psi for the base SAG injection.
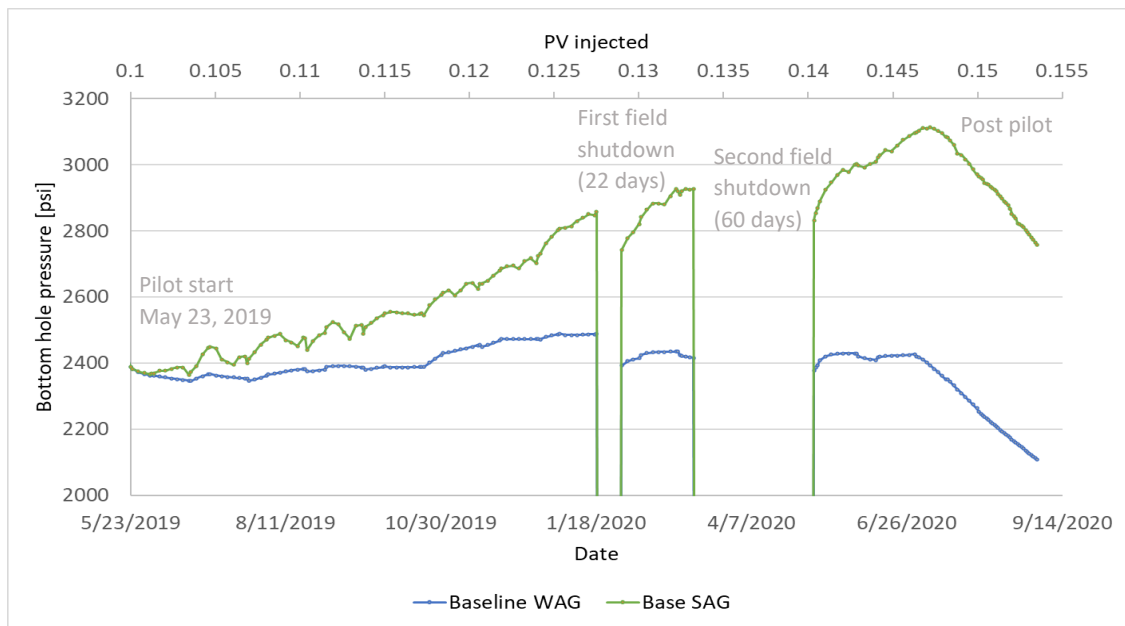
Figure 10.1 Injection bottom hole pressure (BHP) versus time and pore volume (PV) injected for the baseline WAG (blue curve) and base SAG (green curve) simulation cases. The base SAG injection obtained a significantly higher pressure than the baseline WAG injection due to the generation of foam.

10.1.2 CO_2 Mobility Reduction

CO_2 and water tracers were used to analyze CO_2 mobility reduction by foam. A delay in CO_2 breakthrough indicates a larger reduction in CO_2 mobility. The migration rate and number of days for breakthrough from the injection well to the production well for the tracers was described in Section 8.3.1 and shown in Table 10.1 for the baseline WAG and base SAG. To measure the baseline migration rate, a CO_2 tracer, GS1, and a water tracer, WT1 were injected before the start of the pilot, January 3, 2018, and November 21. 2018, respectively. Shortly after the start of the pilot, CO_2 tracer, GS2, and water tracer, WT2, were injected. GS2 was injected in CO_2 slug 1 June 3, 2019, and WT2 was injected in water/surfactant slug 1, May 23, 2019.

Figure 10.2 shows tracer response curves for the first CO_2 tracer (GS1) and the first water tracer (WT1). The red line indicates tracer injection, and the orange and yellow curves indicate tracer production for the baseline WAG and base SAG, respectively. Both the CO_2 tracer (GS1) (Figure 10.2, a) and the water tracer WT2 (Figure 10.2, b) were placed before the start of the pilot and injected with the same rate. The migration rate for the CO_2 tracer was 6 ft/day and it had a breakthrough time of 125 days for both cases (Figure 10.2, a). The migration rate for the water tracer was 4.66 ft/day and it had a breakthrough time of 161 days (Figure 10.2, b). The 36-day difference in breakthrough between the water and the CO_2 phase was related to the mobility ratio difference for the two fluids. Pure CO_2 flooding suffers from early gas breakthrough as a direct consequence of an unfavorable mobility ratio (Kovscek & Radke, 1993; Lee & Kam, 2013) as can be seen in this case by the higher migration rate for the CO_2 phase.

Figure 10.2 Tracer response curves with tracer injection (red curve), CO_2 tracer (GS1) and water tracer (WT1) production for baseline WAG (orange curve) and base SAG (yellow curve). Baseline WAG and base SAG had the same production time of 125 days for GS1 and 161 days for WT1.

A distinct set of tracers were also injected in the first cycle of the pilot as described in Section 8.3.1. For the CO_2 tracer, the effect of foam was expected to increase the breakthrough time for the CO_2 phase, indicating reduced mobility. Figure 10.3 shows the tracer response curves for the CO_2 tracer GS2 (Figure 10.3, a) and the water tracer WT2 (Figure 10.3, b) for the WAG and SAG simulation cases. The migration rate of the CO_2 tracer in the WAG was 10.87 ft/day whereas the CO_2 tracer in the SAG injection had a reduced migration rate of 6.88 ft/day (Table 10.1). When comparing the days from injection to production, the WAG CO_2 tracer broke at the production well in 69 days and the SAG CO_2 tracer broke through in 109 days. The 40-day delay in breakthrough time was caused by the foam generation and reduced CO_2 mobility in the SAG case. The water phase in the WAG injection had a migration rate of 4.08 ft/day, whereas the migration rate was 3.50 ft/day for the SAG injection. When comparing the days of migration, the WAG water tracer used 184 days to breakthrough, whereas the surfactant tracer in the SAG injection used 214 days. Foam generation in the SAG case may have reduced the relative permeability of the water phase, however, foam is not expected to have a large impact on water mobility.

The last CO_2 tracer, GS3, did not have a breakthrough in the production well for the base SAG simulation and was therefore not included. For the next sections, the first two tracers (GS1 and WT1) have not been displayed due to them not changing for any of the cases. The second water tracer (WT2) is also not included due to the design of this model not targeting changes in the water phase.
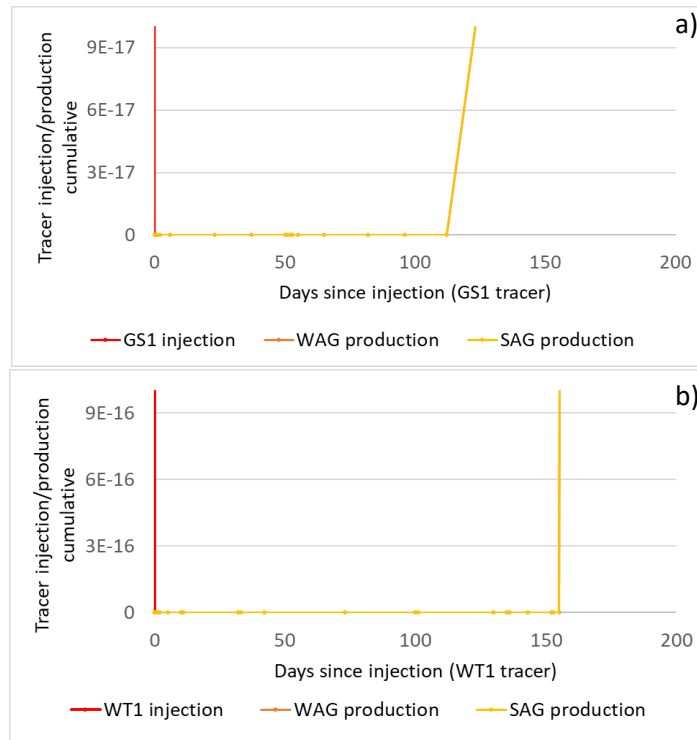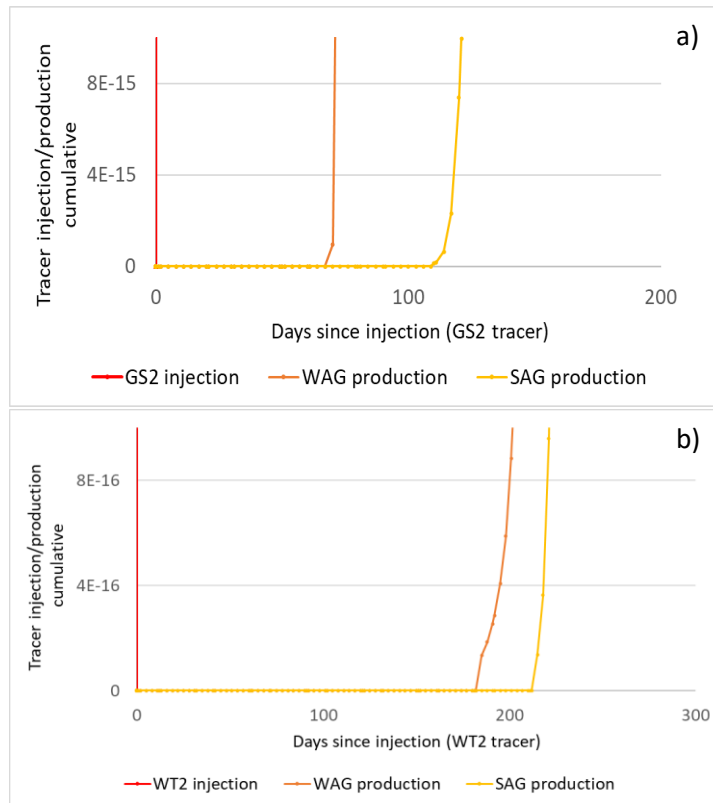
Figure 10.3 Tracer response curves with tracer injection (red curve), CO_2 tracer (GS2) and water tracer (WT2) production for baseline WAG (orange curve) and base SAG (yellow curve). Baseline WAG had a breakthrough time of 69 days for the GS2 tracer and 184 days for the WT2 tracer while the base SAG had a breakthrough time of 109 days for the GS2 tracer and 241 days for the WT2 tracer.

Table 10.1 Overview of breakthrough time and migration rate between the injection well and the production well for tracer GS1, WT1, GS2 and WT2

Tracer		WAG	SAG
GS1	Tracer Breakthrough time	125 days	
WT1		161 days	
GS2		69 days	109 days
WT2		184 days	214 days
GS1	Migration rate	6 ft/day	
WT1		4.66 ft/day	
GS2		10.87 ft/day	6.88 ft/day
WT2		4.08 ft/day	3.50 ft/day

Another way of evaluating the impact of foam on CO_2 mobility is by analyzing the producing gas-oil ratio (GOR) (Figure 10.4) for the baseline WAG and base SAG. As described in Section 8.5.6, a reduction in producing GOR is one method to verify CO_2 mobility control by foam at the field-scale.

Shortly after the start of the pilot, both the WAG and the SAG had a small decrease in the GOR with the SAG injection having the lowest ratio of 2.8 mscf/stb, 39.3% lower than for the WAG injection which was at 3.9 mscf/stb at its lowest. The GOR then increased for both injection cases at ~0.11 PV injected with the WAG injection always having a higher GOR than the SAG injection. From the tracer data, it can be seen that the GS2 tracer did not have a breakthrough until September 20, 2019, which

means that most of the increase in GOR seen before this, was the result of the pre-pilot and previous flooding. Simultaneously, the WT2 trace did not have a breakthrough until December 23, 2019, which also would contribute to a higher GOR with the reduced migration rate in the water phase.

The WAG injection peaked at a value of 18.9 mscf/stb before flattening out with a slight decrease up until the first shutdown (Figure 10.4, grey line). The SAG peaked at a value of 14.7 mscf/stb before decreasing with a steep slope ending with a GOR 405.7% lower than for the WAG, indicating a highly effective reduction of CO_2 mobility by foam in the SAG injection.

The drop in ratio after 0.146 PV injected was the start of the post-pilot, after this, both cases increased in GOR, before ending at a value of 17.9 mscf/stb for the baseline WAG and 10.2 mscf/stb for the base SAG. The increase was caused by the WAG in the post-pilot not supplying the system with more surfactant solution and thereby not reducing the CO_2 mobility to the same effect as seen for the SAG injection. Throughout the flooding, the ratio for the SAG injection was on average 115.4% lower than the ratio for the WAG injection further confirming the success of the CO_2 foam mobility control.

Figure 10.4 Producing Gas-oil ratio (GOR) versus time and pore volume (PV) injected for the WAG (blue curve) and SAG (green curve) with the grey line marking the first shut down. The base SAG injection obtained a significantly lower GOR than the baseline WAG injection.

10.1.3 Sweep Efficiency

Sweep improvement by foam was evaluated by analyzing water cut in the production well. As a result of generation of foam and CO_2 mobility reduction in the reservoir, a better macroscopic sweep and a higher volume of mobilized fluids are expected (Green & Willhite, 1998). Figure 10.5 shows the water cut versus time and pore volume (PV) injected for the baseline WAG (blue curve) and the base SAG (green curve). At the start of the pilot injection, the water cut was high at ~0.96 stb/stb for both cases due to waterflooding conducted before the start of the pilot (Chapter 6).

After 0.11 PV had been injected (Figure 10.5), the water cut decreased for both the SAG and the WAG, with the WAG declining at a steeper slope. When 0.12 PV had been injected, the SAG had a water cut of 0.89 stb/stb and the WAG 0.84 stb/stb. At this point, the water cut in the SAG started to increase before reaching a maximum value of 0.97 stb/stb as the field was shut down (0.127 PV injected). At the same time, the water cut for the WAG injection continued to decrease before reaching a water cut of 0.82 stb/stb right as the field was shut down for the first out of the two

shutdowns in the pilot. At this point, the SAG had a 18.3% higher water cut than the WAG injection. This was due to the CO_2 foam increasing the volumetric sweep in the SAG injection.

After resuming the injection, the water cut for the SAG had a small increase before decreasing to 0.93 stb/stb, right before the second field shutdown. For the WAG, the water cut continued to decrease as before the first shut down and ended on a water cut of 0.80 stb/stb, which was 14.8% lower than the SAG, right before the second shut down. After the final shut down, the water cut for the SAG had a decrease of 0.02 stb/stb, before increasing by 0.03 stb/stb, and finally decreasing during the post-pilot, ending on a water cut of 0.90 stb/stb. The water cut for the WAG also saw a decrease after the final shutdown. First, it decreased by 0.05 stb/stb, before increasing by 0.08 stb/stb to a water cut of 0.87, which was held throughout the post-pilot.

At the end of the pilot, the water cut in the SAG was 8.1% higher than for the WAG, but after the post-pilot, it was only 3.5% higher. The SAG saw a change in the water cut during the post-pilot due to foam no longer being generated at the same rate as before, whereas the WAG saw no change due to it not having any major changes for the injection scheme between the pilot and post-pilot.
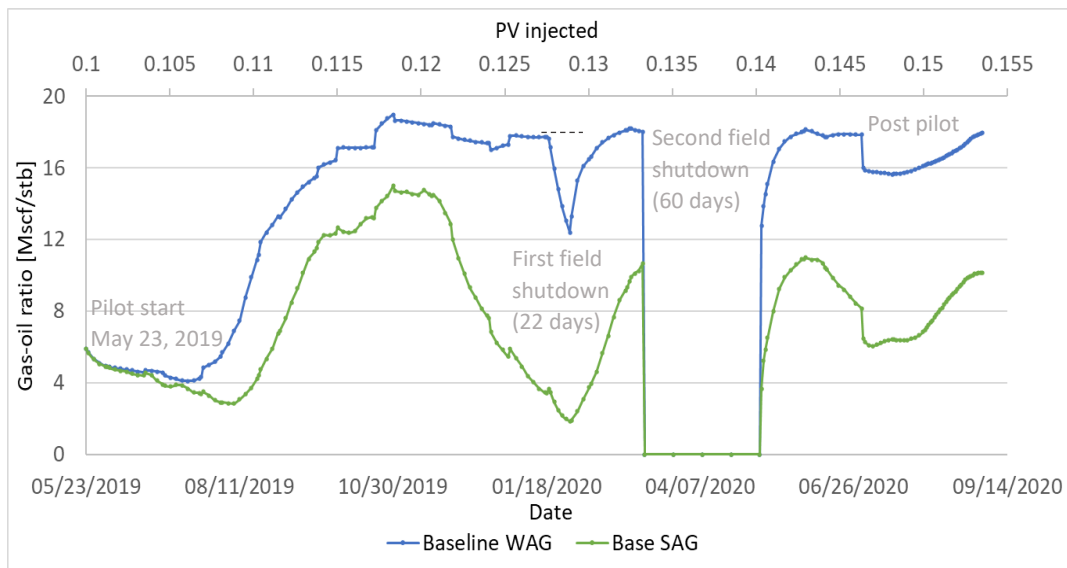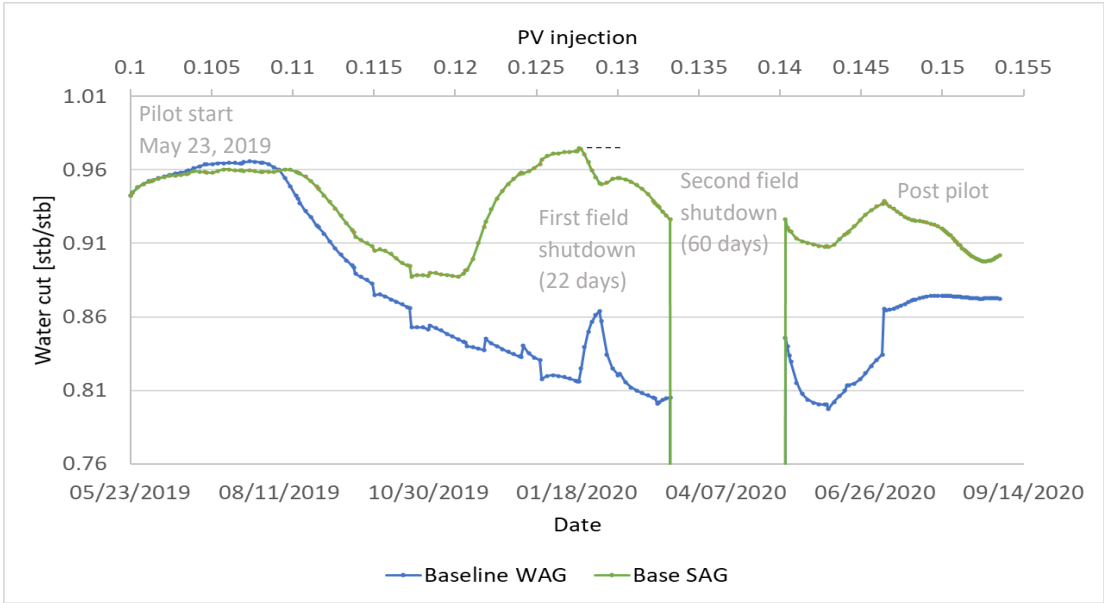

Figure 10.5 Producing Water cut versus time and pore volume (PV) injected for WAG (blue curve) and SAG (green curve) with the grey line marking the first shut down. The base SAG injection obtained a significantly higher water cut than the baseline WAG injection.

10.2 Sensitivity Study – Experimentally Derived Foam Models

Experimentally derived foam models (listed in Table 8.4) were investigated and compared based on foam generation, CO_2 mobility reduction and sweep efficiency in a numerical model. As described in section 8.5.2, the foam model values were tested in all permeability regions, simultaneously.

10.2.1 Foam Generation

An increase in bottom hole pressure (BHP) is usually an indication of foam generation. To compare the foam generation ability of the different models, the bottom hole pressure (BHP) in the injection well was compared for the four different foam models (Table 8.4). Figure 10.6 shows the BHP versus time for the injection well for foam model 1 (grey curve), foam model 2 (yellow curve), foam model 3 (blue curve), and foam model 4 (green curve). A secondary x-axis showing pore volume (PV) injected is also included.

The BHP for all the foam models started to increase shortly after the start of the pilot on May 23, 2019, with a base pressure of 2391.3 psi for all foam models. Right after the start, foam model 4 had the highest BHP which suggests that it generated the strongest foam. Throughout the flooding, the BHP increased steadily for all foam models. After 0.146 PV had been injected, all the foam models peaked in BHP, which was at 3259.7 psi for foam model 4, 3049.6 psi for foam model 2, 2954.8 psi for foam model 3, and 2890.3 psi for foam model 1 which had the lowest peak value. Thus indicating, the strongest foam was generated in foam model 4, then foam model 2, foam model 3, and lastly foam model 1 with the weakest foam. Throughout the full SAG injection, the order of the BHP for the foam models stayed the same.

The average BHP for the whole injection was 2749.7 psi for foam model 4, 2649.2 psi for foam model 2, 2612.5 psi for foam model 3, and 2582.7 psi for foam model 1. Which lists the pressure as 3.8% lower for foam model 2 than foam model 4 on average, 5.3% lower for foam model 3 than foam model 4 on average, and 6.5% lower for foam model 1 than foam model 4 on average. Indicating the overall performance of foam generation to be close in value for the different foam models.

All models decreased in BHP after 0.146 PV had been injected due to the post-pilot not supplying surfactant solution for generation of new foam.
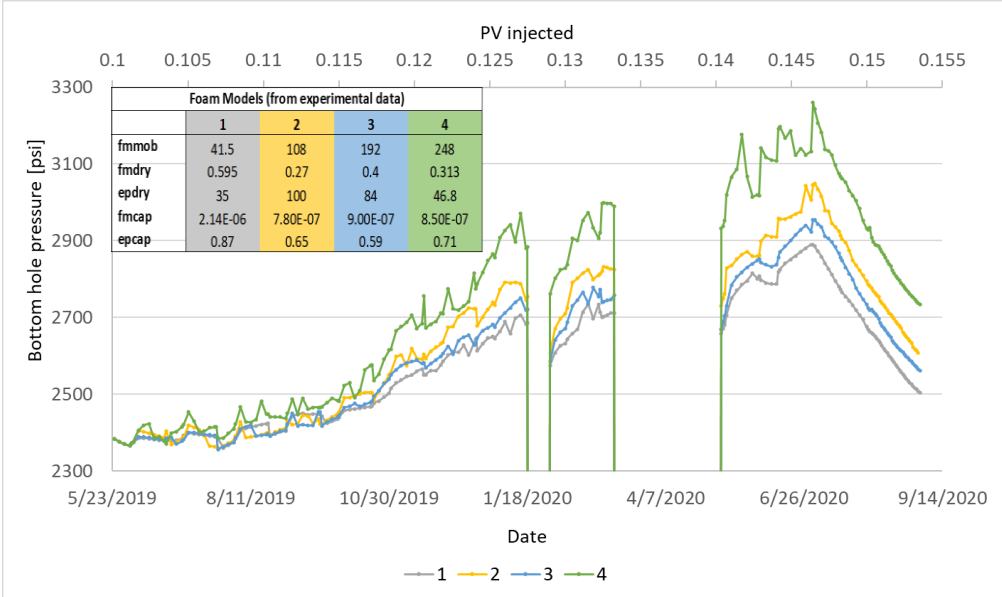
Figure 10.6 Injection bottom hole pressure (BHP) versus time and pore volume (PV) injected for foam model 1 (grey curve), foam model 2 (yellow curve), foam model 3 (blue curve), and foam model 4 (green curve) (Table 8.4).

10.2.2 CO_2 Mobility Reduction

The migration rate and number of days for breakthrough from the injection well to the production well for the tracers was described in Section 8.3.1 and shown in Table 10.2 for the experimentally derived foam models. The tracers were used to compare the individual foam model's ability to reduce the CO_2 mobility.

Figure 10.7 shows the tracer response curves for CO_2 tracer GS2 and GS3. The red line indicates the injection of the tracer, the grey curve the production of foam model 1, the yellow curve the production of foam model 2, the blue curve the production of foam model 3, and the green curve the production of foam model 4. The CO_2 tracer (GS2) (Figure 10.7, a) was placed in the first CO_2 cycle in the pilot and CO_2 tracer GS3 (Figure 10.7, b) was placed in the 11th CO_2 cycle (Section 8.4.1).

The migration rate for the GS2 CO_2 tracer was 10.00 ft/day for foam model 1, and it had a breakthrough time of 75 days, foam model 2 had a migration rate of 8.43 ft/day and a breakthrough time of 89 days, foam model 3 had a migration rate of 9.04 ft/day and a breakthrough time of 83 days, and foam model 4 with a migration rate of 4.34 ft/day and a breakthrough time of 173 days (Figure 10.7, a, Table 10.2). This suggests that foam model 4 had the highest reduction of CO_2 mobility, then foam model 2, foam model 3, and lastly foam model 1 with the least reduction of foam mobility and the quickest CO_2 breakthrough. This is consistent with the order seen for the BHP (Figure 10.6), with foam model 4 having the highest and foam model 1 the lowest BHP. Thus, the highest BHP generated the strongest foam and thereby increased the breakthrough time more than the models with lower BHPs.

For CO_2 tracer GS3 (Figure 10.7, b), the foam models followed the same order for both migration rate and breakthrough time as for GS2 (Table 10.2). The producing breakthrough time and migration rates, however, was quicker for the GS3 than they were in GS2, with the same injection rate. This was caused by the higher relative permeability for the CO_2 in the system when GS3 was injected. This was at the end of the pilot and large amounts of CO_2 had been injected for a year. It could also be the result of the two shutdowns which increased the pressure in the system and thereby increasing the production rate of the reservoir fluids after resuming production.
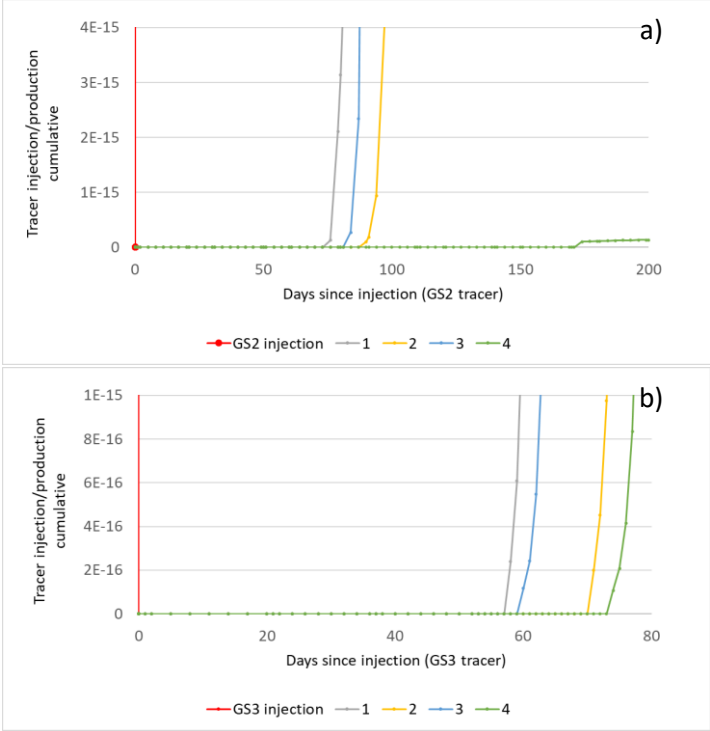
Figure 10.7 Tracer response curves showing tracer injection (red curve), and production of CO_2 tracer GS2 (a) and GS3 (b) for foam model 1 (grey curve), foam model 2 (yellow curve), foam model 3 (blue curve), and foam model 4 (green curve).

Table 10.2 Overview of breakthrough time and migration rate between the injection well and the production well for CO_2 tracer GS2 and GS3

Tracer		Foam model 1	Foam model 2	Foam model 3	Foam model 4
GS2	Breakthrough	75 days	89 days	83 days	173 days
GS3	time	57 days	70 days	59 days	73 days
GS2	Migration	10.00 ft/day	8.43 ft/day	9.04 ft/day	4.34 ft/day
GS3	rate	13.16 ft/day	10.71 ft/day	12.71 ft/day	10.27 ft/day

Another way of verifying and comparing foam flow in the system is by analyzing the producing gas-oil ratio (GOR) for the experimentally derived foam models. As described in Section 8.5.6, a reduction in producing GOR is one method of verifying CO_2 mobility control by foam at the field-scale.

The average GOR was 10.49 mscf/stb for foam model 1, 9.44 mscf/stb for foam model 2, 9.76 mscf/stb for foam model 3, and 8.54 mscf/stb for foam model 4. Which supports the trend seen for the tracers with foam model 4 reducing the CO_2 mobility the most, and foam model 1 reducing the CO_2 mobility the least.
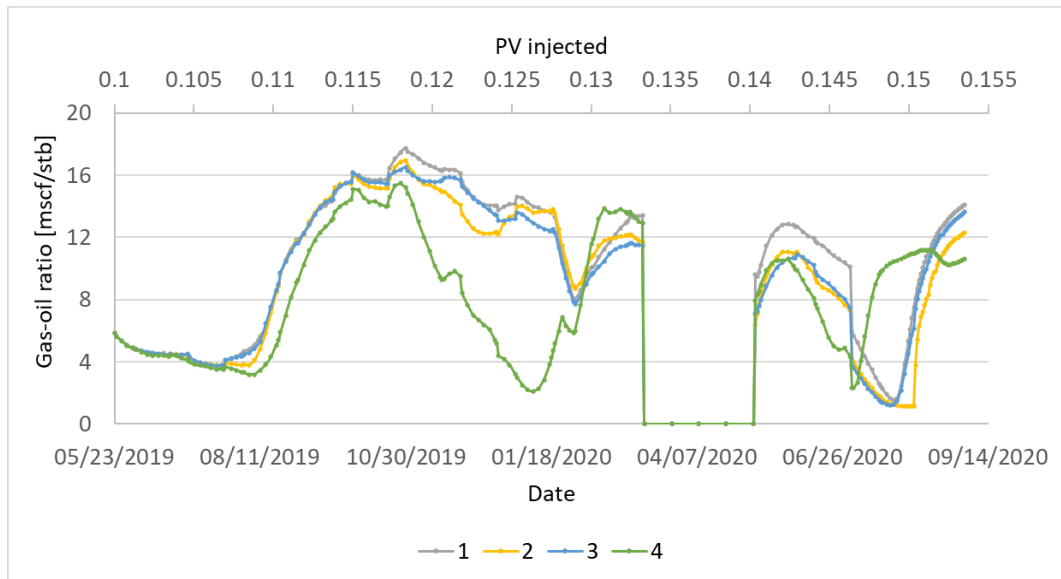
Figure 10.8 Producing Gas-oil ratio (GOR) versus time and pore volume (PV) injected for foam model 1 (grey curve), foam model 2 (yellow curve), foam model 3 (blue curve), and foam model 4 (green curve).

10.2.3 Sweep Efficiency

Sweep improvement by foam was evaluated and compared by analyzing water cut in the production well for the different foam models. Figure 10.9 shows the water-cut versus time and pore volume (PV) injected for foam model 1 (grey curve), foam model 2 (yellow curve), foam model 3 (blue curve), and foam model 4 (green curve). At the start of the pilot injection, the water cut was high at ~0.96 stb/stb for all cases due to the waterflooding conducted before the start of the pilot (Chapter 6).

After 0.11 PV had been injected (Figure 10.9), the water cut started to decrease with the same slope down to 0.86 stb/stb at 0.118 PV injected for all foam models. After this, foam model 4 increase to a water cut of 0.98 stb/stb which suggests a far greater volumetric sweep than for the other foam models that all had a water cut of ~0.88 stb/stb at the same pore volume injected (0.126 PV injected). They all saw a steady increase in water cut up until the first shutdown and after resuming

production following the second shutdown, suggesting an increased volumetric sweep for all foam models (0.117 to 0.146 PV injected).

The average water cut throughout the flooding was 0.93 stb/stb for foam model 4, 0.92 stb/stb for foam model 3, 0.92 stb/stb for foam model 2 and 0.91 stb/stb for foam model 1, suggesting foam model 4 had the most effective volumetric sweep, and foam model 1 the least, which supports the trends seen for the BHP, CO_2 tracers and GOR. The spread in values, however, was small between the models.

Figure 10.9 Producing water cut versus time and pore volume (PV) injected for foam model 1 (grey curve), foam model 2 (yellow curve), foam model 3 (blue curve), and foam model 4 (green curve).

10.3 Sensitivity Study – No Foam in Low Permeability Regions

The experimentally derived foam models (listed in Table 8.4) were investigated and compared regarding foam generation, CO_2 mobility reduction and sweep efficiency. As described in section 8.5.3, the foam model values were tested in all permeability regions, simultaneously, except for in permeability Region 1 where the values from the base foam model listed in Table 8.3 were used. This was tested to account for the shear-thinning effect of foam by adjusting the model to not generate foam in the near-well region (Figure 8.5). In addition, no foam was allowed to generate in low permeability regions with permeability values under 10 mD.

10.3.1 Foam Generation

An increase in bottom hole pressure (BHP) is usually an indication of foam generation. To compare the foam generation of the different models, the bottom hole pressure (BHP) in the injection well was compared for the four different foam model setups (Table 8.5). Figure 10.10 shows the BHP versus time for the injection well for foam model 1* (grey curve), foam model 2* (yellow curve), foam model 3* (blue curve), and foam model 4* (green curve). A secondary x-axis showing pore volume (PV) injected is also included.

The BHP for all the foam models started to increase shortly after the start of the pilot on May 23, 2019, with a base pressure of 2391.3 psi for all foam models. Throughout the flooding, BHP increased steadily for all foam models. After 0.146 PV had been injected, all foam models reached a peak BHP of 2855.9 psi for foam model 1*, 3000.1 psi for foam model 2*, 2890.4 psi for foam model 3*, and 3096.2 psi for foam model 4*. Thus, indicating the strongest foam was generated in foam model 4*, then foam model 2*, foam model 3*, and lastly foam model 1* which generated the weakest foam.

72

Throughout the full SAG injection, the order of the BHP for the foam models stayed the same, which was also seen for the BHP for the similar foam models in Section 10.2.1 (Figure 10.6).

The average BHP was 2718.8 psi for foam model 4*, 2665.0 psi for foam model 2*, 2593.2 psi for foam model 3*, and 2576.4 psi for foam model 1*. Setting the average pressure to be 2.0% lower for foam model 2 than foam model 4*, 4.6% lower for foam model 3* than foam model 4*, and 5.2% lower for foam model 1* than foam model 4*. Thus indicating that the overall foam generation was strongest for foam model 4*and weakest for foam model 1*, but that the models did not have any major differences in the foam generation performance. When compared to the setup in Section 10.2.1, the BHP was sligtly lower with no generation of foam in Region 1, but the difference between them was small.

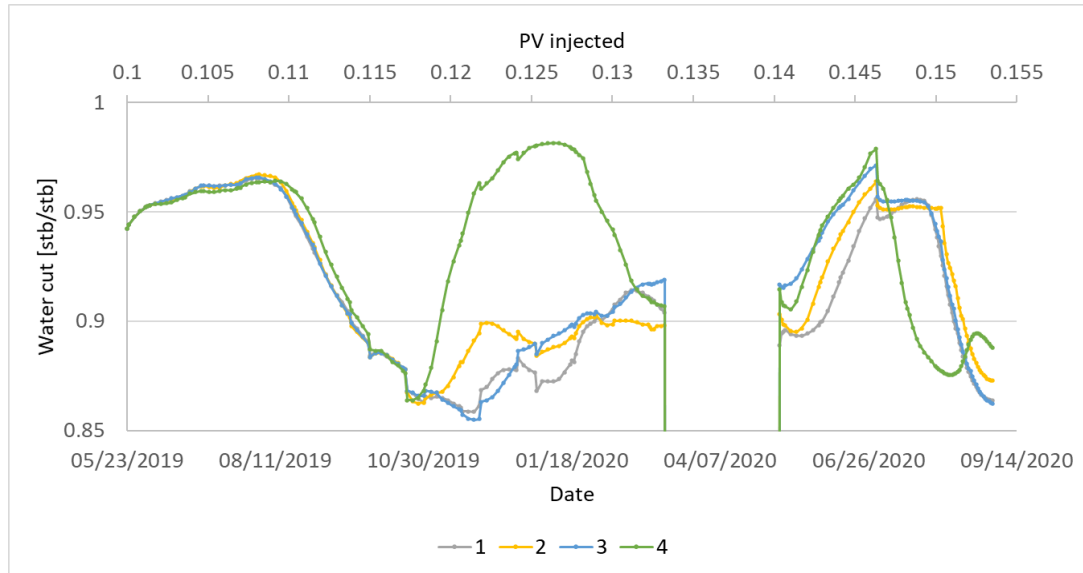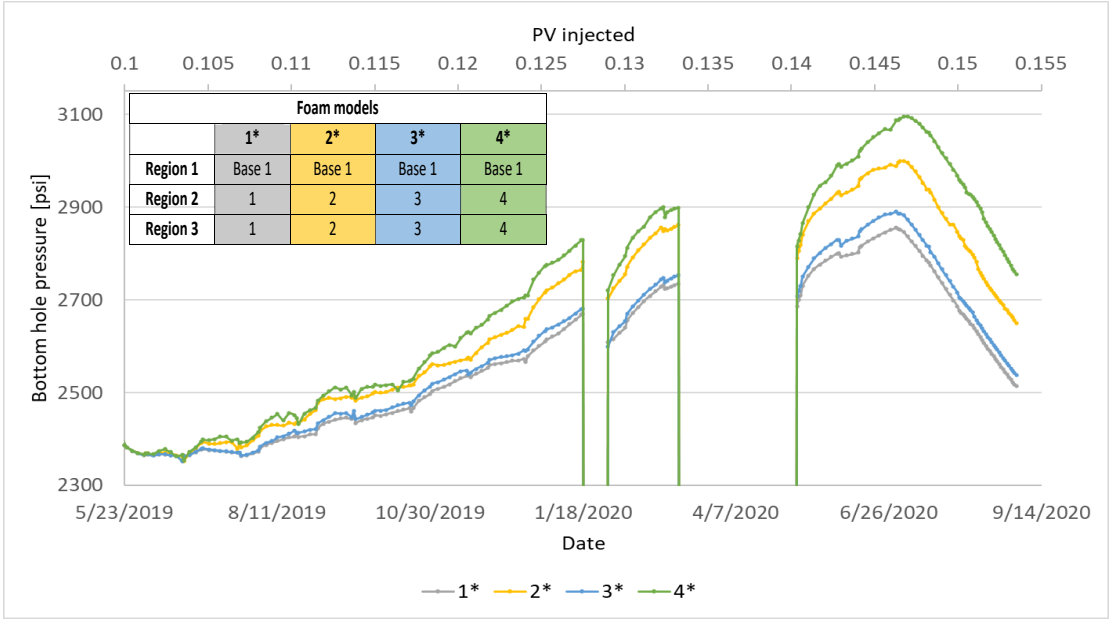Figure 10.10 Injection bottom hole pressure (BHP) versus time and pore volume (PV) injected for foam model 1* (grey curve), foam model 2* (yellow curve), foam model 3* (blue curve), and foam model 4* (green curve) (Table 8.5).

10.3.2 CO_2 Mobility Reduction

The migration rate and number of days for breakthrough from the injection well to the production well for the tracers was described in Section 8.3.1 and shown in Table 10.3 for the experimentally derived foam models. The tracers were used to compare the individual foam model's ability to reduce CO_2 mobility.

Figure 10.11 shows the tracer response curves for the two CO_2 tracers GS2 and GS3. The red line indicates the injection of the tracer, the grey curve the production of foam model 1*, the yellow curve the production of foam model 2*, the blue curve the production of foam model 3*, and the green curve the production of foam model 4*. The CO_2 tracer (GS2) (Figure 10.11, a) was placed in the first CO_2 cycle in the pilot and CO_2 tracer GS3 (Figure 10.11, b) was placed in the 11th CO_2 cycle (Section 8.4.1).

The migration rate for the GS2 CO_2 tracer was 9.38 ft/day for foam model 1*, and it had a breakthrough time of 80 days, foam model 2* had a migration rate of 8.06 ft/day and a breakthrough time of 93 days, foam model 3* had a migration rate of 9.62 ft/day and a breakthrough time of 78 days, and foam model 4* with a migration rate of 7.58 ft/day and a breakthrough time of 99 days (Figure 10.11, a, Table 10.3). Hence suggesting that foam model 4* had the highest reduction of CO_2

mobility, then foam model 2*, foam model 1*, and lastly foam model 3* with the least reduction of CO_2 mobility and the quickest CO_2 breakthrough.

For the CO_2 tracer, GS3 (Figure 10.11, b), the foam models did not follow the same order as for GS2. From tracer migration rate and breakthrough time, foam model 4* did still reduce the CO_2 mobility the most, and then foam model 2*, but foam model 1* and 3* switched places. The two foam models had a breakthrough time for GS2 with only 2 days separating them. For GS3, the order was opposite and there was 6 days separating them. This was after the two shutdowns and at a point where the pilot had injected fluids for over a year, which had increased the reservoir pressure and the CO_2 relative permeability due to a higher saturation of CO_2. The breakthrough time and migration rate were also faster for GS3 than for GS2, this might also be due to the high CO_2 saturation and increase in reservoir pressure.
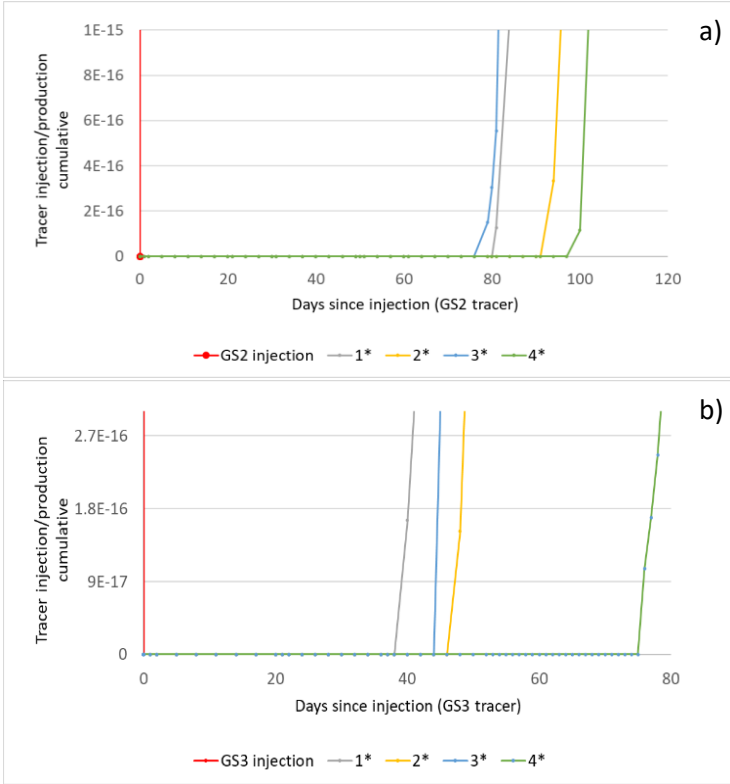
Figure 10.11 Tracer response curves showing tracer injection (red curve), and production of CO_2 tracer GS2 (a) and GS3 (b) for foam model 1* (grey curve), foam model 2* (yellow curve), foam model 3* (blue curve), and foam model 4* (green curve).

Table 10.3 Overview of breakthrough time and migration rate between the injection well and the production well for CO_2 tracer GS2 and GS3

Tracer		Foam model 1*	Foam model 2*	Foam model 3*	Foam model 4*
GS2	Breakthrough	80 days	93 days	78 days	99 days
GS3	time	39 days	47 days	45 days	73 days
GS2	Migration	9.38 ft/day	8.06 ft/day	9.62 ft/day	7.58 ft/day
GS3	rate	19.23 ft/day	15.96 ft/day	16.67 ft/day	10.00 ft/day

Another way to verify and compare foam flow in the system is by analyzing the producing gas-oil ratio (Figure 10.12) for the experimentally derived foam models (Foam model 1* to 4*). As described

in Section 8.5.6, a reduction in producing GOR is one method to verify CO_2 mobility control by foam at the field-scale.

The average GOR was 11.49 mscf/stb for foam model 1*, 9.55 mscf/stb for foam model 2*, 11.14 mscf/stb for foam model 3*, and 7.81 mscf/stb for foam model 4* (Figure 10.12). Thus, supporting the trend seen for the BHP and CO_2 tracers, where foam model 4* reduced the CO_2 mobility the most, but also the overall trend of only minor differences between all models.
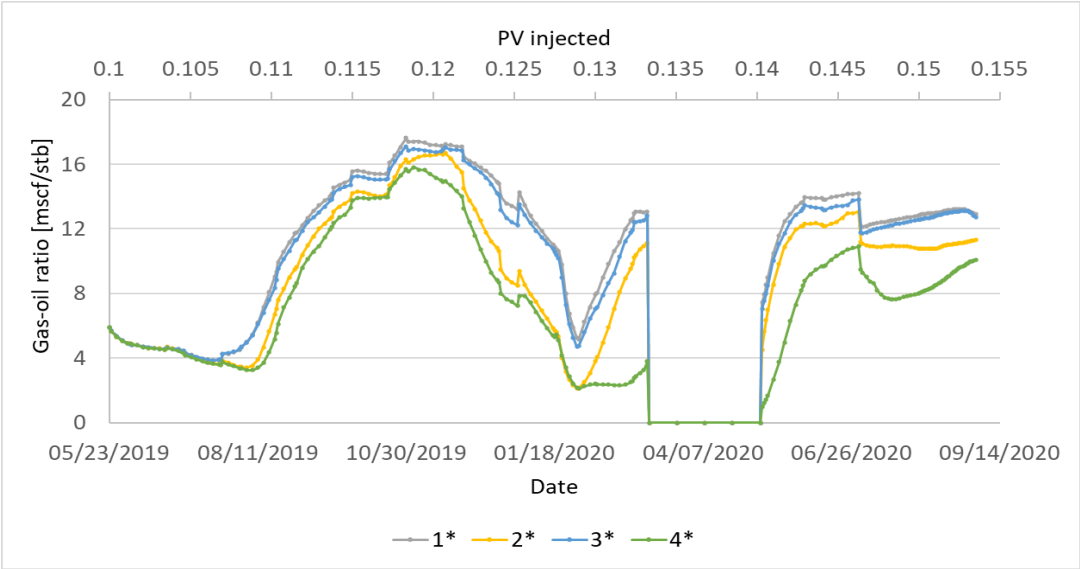
Figure 10.12 Producing Gas-oil ratio (GOR) versus time and pore volume (PV) injected for foam model 1* (grey curve), foam model 2* (yellow curve), foam model 3* (blue curve), and foam model 4* (green curve).

10.3.3 Sweep Efficiency

Sweep improvement by foam was evaluated and compared for the foam models by analyzing water cut in the production well. Figure 10.13 shows the water cut versus time and pore volume (PV) injected for foam model 1* (grey curve), foam model 2* (yellow curve), foam model 3* (blue curve), and foam model 4* (green curve). At the start of the pilot injection, the water cut was high at ~0.96 stb/stb for all cases due to waterflooding conducted before the start of the pilot (Chapter 6).

The average water cut was 0.91 stb/stb for foam model 1*, 0.92 stb/stb for foam model 2*, 0.91 stb/stb for foam model 3* and 0.93 stb/stb for foam model 4*, suggesting a slightly better volumetric sweep for foam model 4* than for the other models. This is also supported by the model having the highest BHP, the slowest migration rate and the lowest GOR.

For these models compared to the setup in Section 10.2.3, the behavior of the individual models is more similar to each other. They also have a higher response to the CO_2 breakthrough at 0.12 PV injected where all foam models increase in water cut from ~0.87 stb/stb at 0.117 PV injected to ~0.96 stb/stb at 0.127 PV injected. The increase was roughly from ~0.86 to ~0.90 stb/stb for the foam models in Section 10.2.3, suggesting a better volumetric sweep earlier in the models that accounts for shear thinning. The average water cut was still the same between the two cases due to the high increase in water cut after the second shutdown (0.141 PV injected) for the foam models in Section 10.2.3.
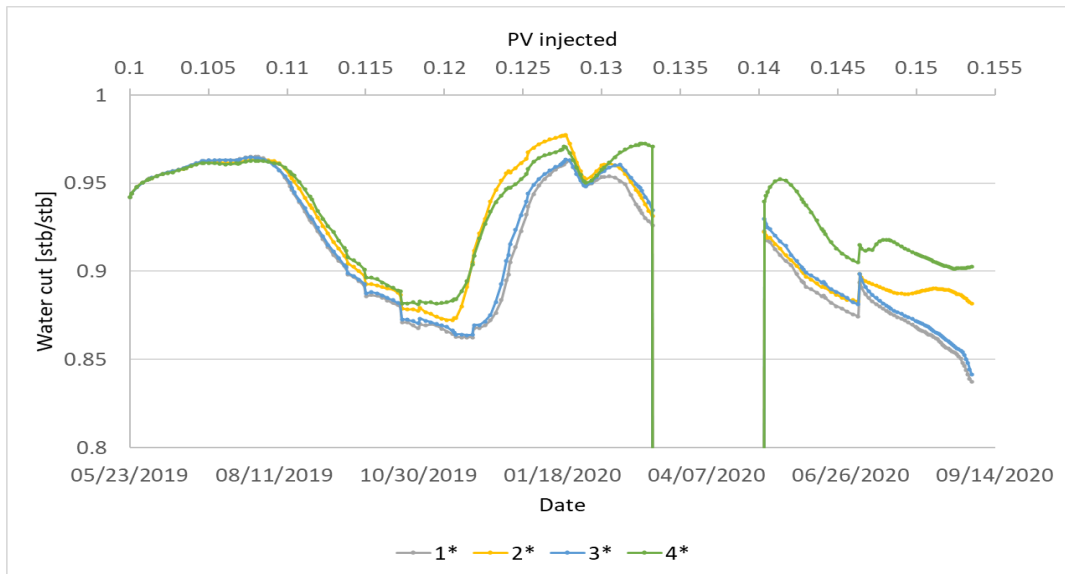
Figure 10.13 Producing water cut versus time and pore volume (PV) injected for foam model 1* (grey curve), foam model 2* (yellow curve), foam model 3* (blue curve), and foam model 4* (green curve).

10.4 Sensitivity Study - Combination of Experimentally Derived Foam Models

Experimentally derived foam models (listed in Table 8.4) were investigated and compared regarding foam generation, CO_2 mobility reduction, and sweep efficiency. As described in Section 8.5.4, the experimentally derived foam models were placed in the different permeability regions with the model with lowest reference gas mobility-reduction factor for foam (*fmmob*) placed in the region with the lowest permeability, and the models with the higher *fmmob*s in the higher permeability regions. This was performed to account for the impact of permeability on foam. As described in Section 4.1.1, permeability plays a central role in the generation of foam where lower permeability layers hindering the generation of strong foam.

10.4.1 Foam Generation

An increase in bottom hole pressure (BHP) is usually an indication of foam generation. To compare the foam generation ability of the different model combinations, the BHP in the injection well was compared for the three different foam model combinations (Table 8.6). Figure 10.14 shows the BHP versus time for the injection well for combination A (pink curve), combination B (yellow curve), and combination C (blue curve). A secondary x-axis showing PV injected is also included.

Throughout the flooding, the BHP increased steadily for all combinations. After 0.146 PV had been injected, the combinations reached a peak BHP of 2899.3 psi for combination A, 2994.2 psi for combination B, and 3071.1 psi for combination C. Which suggest that the strongest foam was generated by foam model combination C, although the difference was not extensive. Throughout the full SAG injection, the order of the foam models BHP stayed the same.

The average BHP was 2586.8 psi for combination A, 2630.1 psi for combination B, and 2657.7 psi for combination C. A 2.7% decrease for combination A compared to combination C on average, and a 1.0% decrease for combination B compared to combination C on average. Thus, indicating a small spread from the stongest and weakest generated foam, but that the overall strongest foam was generated by combination C.
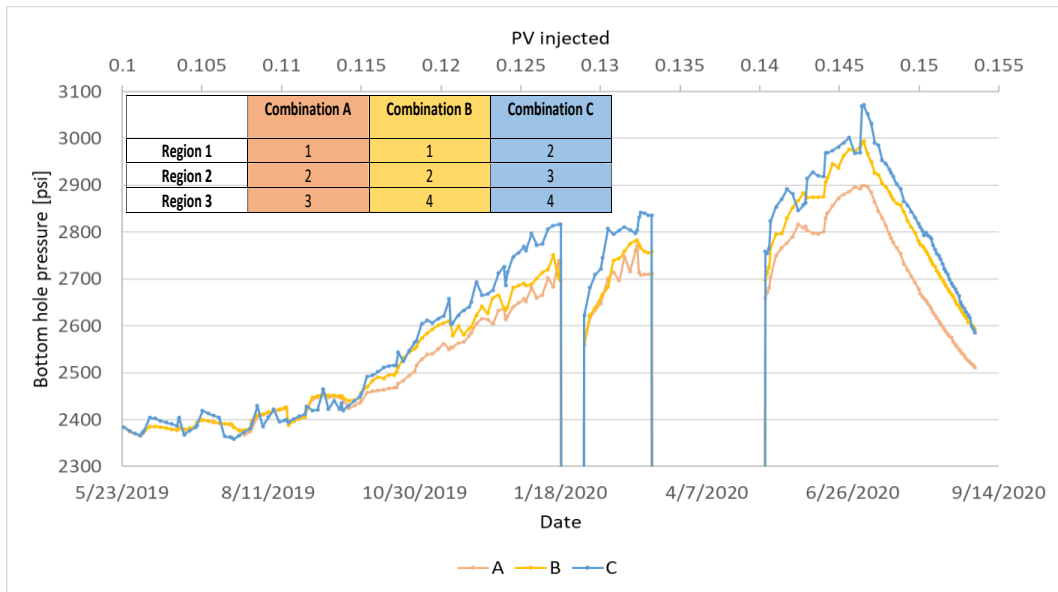
Figure 10.14 Injection bottom hole pressure (BHP) versus time and pore volume (PV) injected for combination A (pink curve), combination B (yellow curve), and combination C (blue curve) (Table 8.6).

10.4.2 CO$_2$ Mobility Reduction

CO$_2$ tracers were used to analyze the reduction of CO$_2$ mobility by foam, whereas a longer delay in CO$_2$ breakthrough indicates a larger reduction in CO$_2$ mobility. The migration rate and number of days for breakthrough from the injection well to the production well for the tracers were described in Section 8.3.1 and shown in Table 10.4 for the foam model combinations. The tracers were used to compare each of the foam model combination's ability to reduce the CO$_2$ mobility.

Figure 10.15 shows the tracer response curves for CO$_2$ tracer GS2 and GS3. The red line indicates the injection of the tracer, the pink curve the production of combination A, the yellow curve the production of combination B, and the blue curve the production of combination C. The CO$_2$ tracer GS2 (Figure 10.15, a) were placed in the first CO$_2$ cycle in the pilot and CO$_2$ tracer GS3 (Figure 10.15, b) were placed in the 11th CO$_2$ cycle (Section 8.4.1).

The migration rate for the GS2 CO$_2$ tracer was 10.00 ft/day for combination A and it had a breakthrough time of 75 days, combination B had a migration rate of 9.38 ft/day and a breakthrough time of 80 days, and combination C had a migration rate of 8.33 ft/day and a breakthrough time of 90 days (Figure 10.15, a, Table 10.4). Foam model combination C had the highest reduction of CO$_2$ mobility and thereby generated the strongest foam, although the difference between the different combination was small. For CO$_2$ tracer GS3 (Figure 10.15, b), the foam models followed the same order for both migration rate and breakthrough time as GS2 (Table 10.4). As for the earlier sections, the GS3 tracer also had a higher migration rate and lower breakthrough time in for these cases due to the higher CO$_2$ relative permeability and higher system pressure.
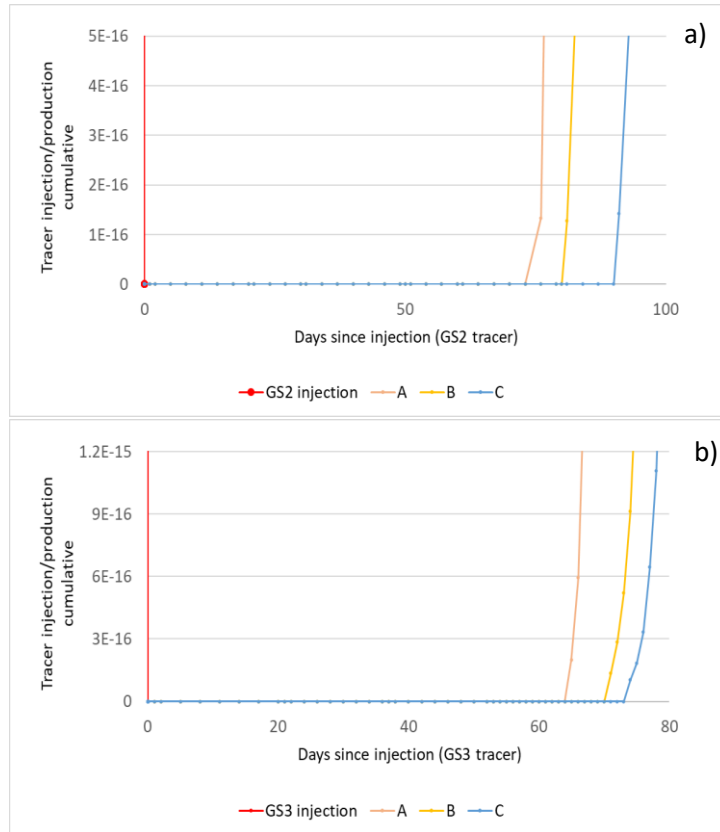
Figure 10.15 Tracer response curves showing tracer injection (red curve), and production of CO_2 tracer GS2 (a) and GS3 (b) for foam model combination A (pink curve), combination B (yellow curve), and combination C (blue curve).

Table 10.4 Overview of breakthrough time and migration rate between the injection well and the production well for CO_2 tracer GS2 and GS3

Tracer		Combination A	Combination B	Combination C
GS2	Breakthrough	75 days	80 days	90 days
GS3	time	64 days	70 days	73 days
GS2	Migration	10.00 ft/day	9.38 ft/day	8.33 ft/day
GS3	rate	11.72 ft/day	10.27 ft/day	10.27 ft/day

Foam generation can also be compared and verified by investigating the producing gas-oil ratio (GOR) for the different foam model combinations. As described in Section 8.5.6, a reduced GOR is one of the characteristics which is used to verify CO_2 mobility control by foam. Producing GOR versus time and pore volume (PV) injected has been graphed (Figure 10.17) for foam model combination A (pink curve), combination B (yellow curve), and combination C (blue curve).

The average GOR was 10.38 mscf/stb for foam model combination A, 9.37 mscf/stb for combination B, and 9.27 mscf/stb for combination C (Figure 10.17). Thus, supporting the trend seen for the BHP and tracers with foam model combination C reducing the CO_2 mobility the most, but that all the combinations were close in overall performance.
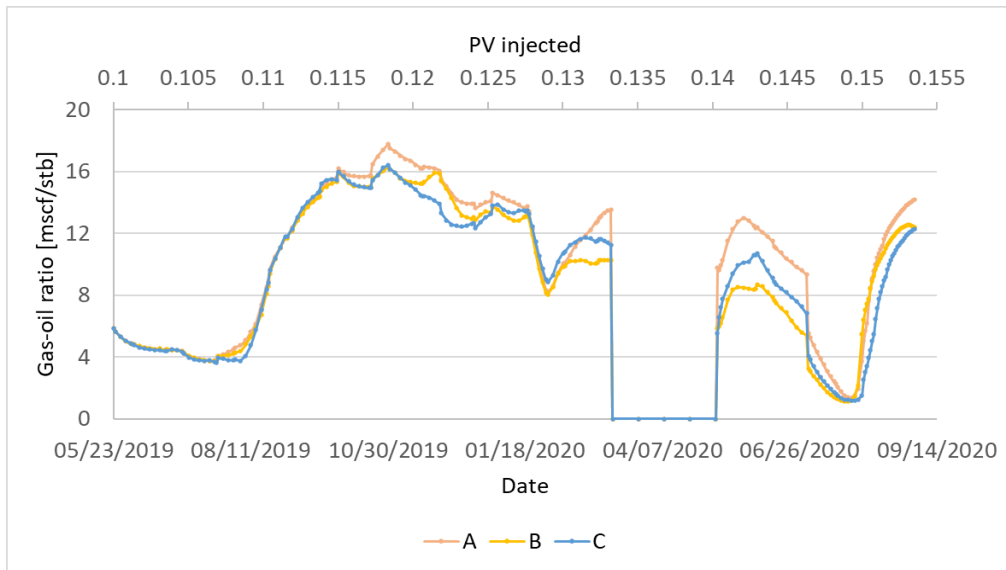
Figure 10.17 Producing gas-oil ratio (GOR) versus time and pore volume (PV) injected for foam model combination A (pink curve), combination B (yellow curve), and combination C (blue curve).

10.4.3 Sweep Efficiency

Sweep improvement by foam was evaluated and compared for the foam model combinations by analyzing water cut in the production well. Figure 10.16 shows the water cut versus time and pore volume (PV) injected for foam model combination A (pink curve), combination B (yellow curve), and combination C (blue curve).

All combinations increased the water cut during the start of the pilot, until 0.11 PV had been injected. Then, all combination decreased in water cut to ~0.86 stb/stb at 0.115 PV injected, before steadily increasing up to a water cut of 0.96 stb/stb at 0.145 PV injected. The slow increase was also seen for the foam models in Section 10.2.3, which also did not account for shear-thinning in the near-well region.

The average water cut was 0.912 stb/stb for foam model combination A, 0.916 stb/stb for combination B and 0.918 stb/stb for combination C, suggesting a slightly better volumetric sweep for foam model combination C but almost a negligible difference between the different combinations.

79
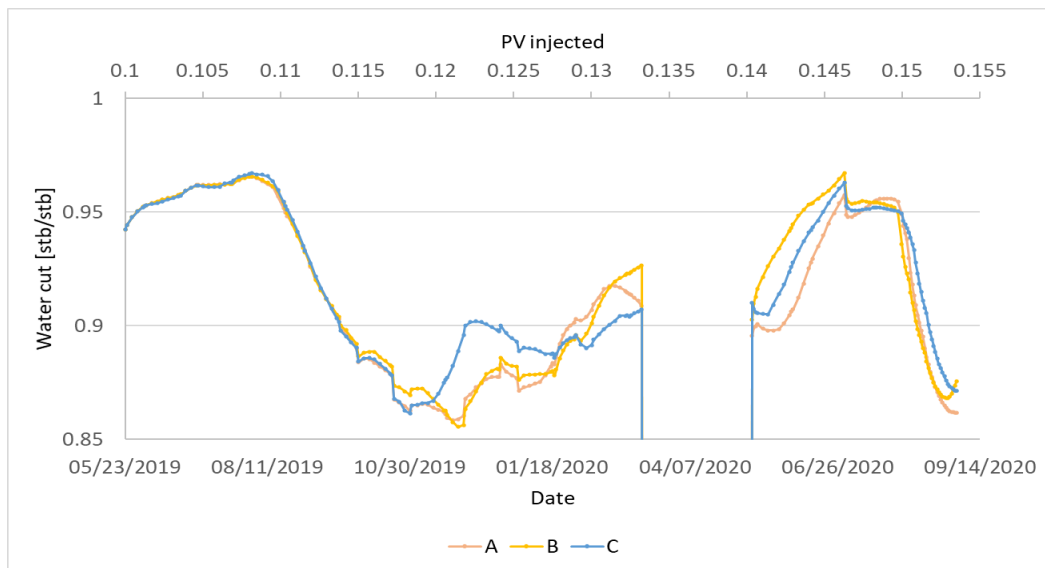
Figure 10.16 Producing water cut versus time and pore volume (PV) injected for foam model combination A (pink curve), combination B (yellow curve), and combination C (blue curve). The highest average water cut was observed for foam model combination C.

10.5 Effect of Oil on Foam in the Base SAG Model

The sensitivity of the base SAG foam model (listed in Table 8.3) to residual reservoir oil was tested by comparing different sensitivities on performance for foam generation, CO_2 mobility reduction and sweep efficiency. As described in Section 8.5.5, the base sensitivity value of 0.28 was found through experimental tests. A high tolerance value was therefore tested and set to 0.40, meaning that all areas of the reservoir (with permeability over the range for Region 1) with a residual oil saturation under 40% will be able to generate foam. Tests showed a maximum of 40% residual oil in the reservoir (Chapter 6), hence, values over 0.4 was unnecessary to test. From 0.28, the tolerance was stepwise lowered down to a minimum of 0.05, to analyze the foam response.

10.5.1 Foam Generation

An increase in bottom hole pressure (BHP) is usually an indication of foam generation. To compare the different oil tolerances (So*) for the different cases (Table 8.7), the BHP in the injection well was compared. Figure 10.18 shows the BHP versus time for the injection well for So* = 0.05 (green curve), So* = 0.10 (pink curve), So* = 0.15 (grey curve), So* = 0.20 (yellow curve) and So* = 0.40 (blue curve). A secondary x-axis showing pore volume (PV) injected is also included.

The average BHP was 2733.0 psi for So* = 0.40, 2702.8 psi for So* = 0.20, 2672.6 psi for So* = 0.15, 2643.3 psi for So* = 0.10, and 2616.8 psi for So* = 0.05. Which was a 1.1% decrease for So* = 0.20 compared to So* = 0.40 on average, a 2.2% decrease for So* = 0.15 compared to So* = 0.40 on average, a 3.3% decrease for So* = 0.10 compared to So* = 0.40 on average, and a 4.3% decrease for So* = 0.05 compared to So* = 0.40 on average. Thus, indicating the overall generation of foam for the models to be approximately the same for the different sensitivities, but that the highest tolerance to oil (So* = 0.40) generated a slightly stronger foam than the rest. The low residual oil saturation in the reservoir might be the reason for the small range in performance for the models.
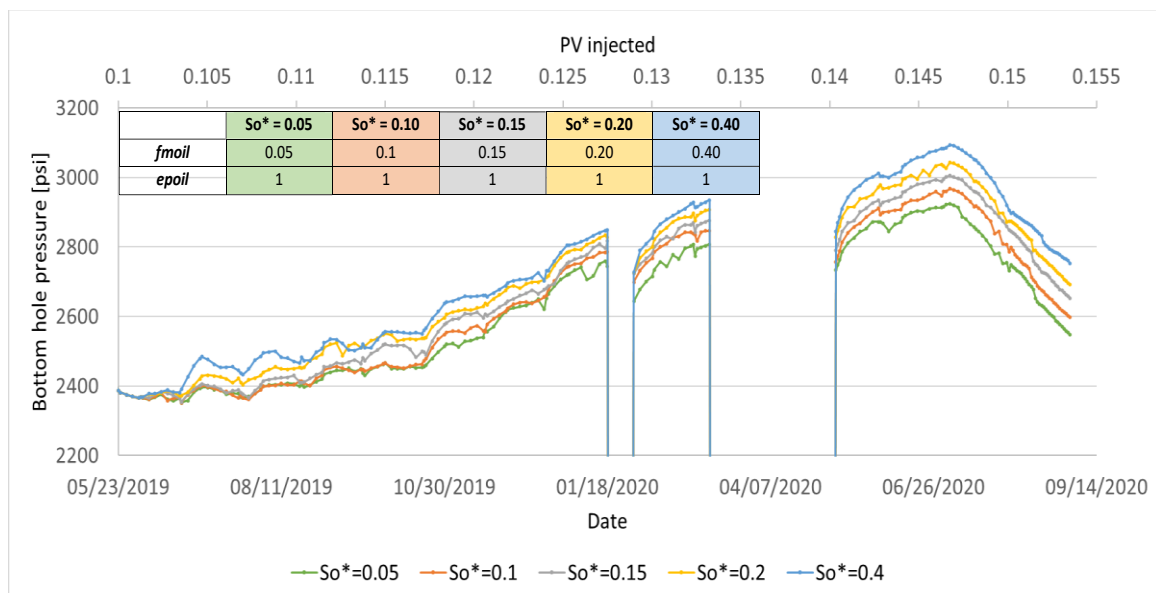
Figure 10.18 Injection bottom hole pressure (BHP) versus time and pore volume (PV) injected for So* = 0.05 (green curve), So* = 0.10 (pink curve), So* = 0.15 (grey curve), So* = 0.20 (yellow curve) and So* = 0.40 (blue curve).

10.5.2 CO₂ Mobility Reduction

The reduction of CO_2 mobility by foam were analyzed by using CO_2 tracers. The migration rate and breakthrough time from the injection well to the production well for the tracers was described in Section 8.3.1 and shown in Table 10.5 for the different oil sensitivity cases. The tracers were used to compare the different sensitivity's ability to reduce the CO_2 mobility.

Figure 10.19 shows tracer response curves for CO_2 tracer GS2 and GS3. The red line indicates the injection of the tracer, the green cure is the So* = 0.05 case, the pink curve is the So* = 0.10 case, the grey curve is the So* = 0.15 case, the yellow curve is the So* = 0.20 case, and the blue curve is the So* = 0.40 case. The CO_2 tracer (GS2) (Figure 10.19, a) was placed in the first CO_2 cycle in the pilot and CO_2 tracer GS3 (Figure 10.19, b) was placed in the 11th CO_2 cycle (Section 8.4.1).

The migration rate for the GS2 CO_2 tracer was 8.33 ft/day for So* = 0.05 and it had a breakthrough time of 90 days, it was 8.06 ft/day for So* = 0.10 and it had a breakthrough time of 93 days, it was 7.58 ft/day for So* = 0.15 and it had a breakthrough time of 99 days, it was 6.94 ft/day for So* = 0.20 and it had a breakthrough time of 108 days, and it was 6. 47 ft/day for So* = 0.40 and it had a breakthrough time of 116 days (Figure 10.19, a, Table 10.5). As seen for the BHP, the migration rates and breakthrough times are still close in value for the different sensitivities and continuing the same order from highest to lowest tolerance to oil. For CO_2 tracer GS3, the order of the production breakthrough times was switched with So* = 0.15 being produced last, but only 8 days differentiated the quickest and slowest breakthrough time.
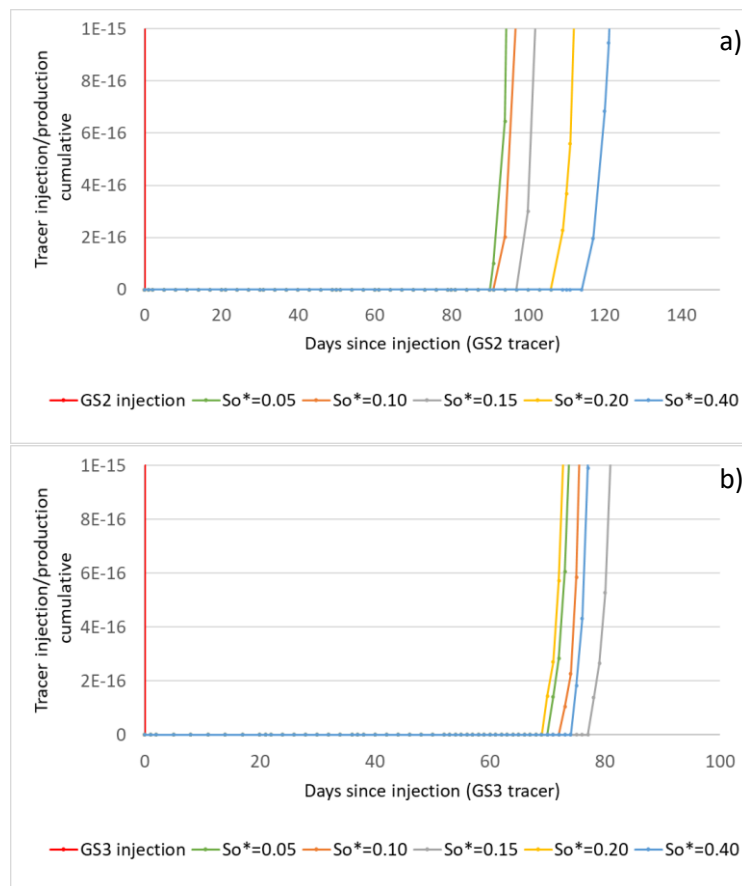
Figure 10.19 Tracer response curves showing tracer injection (red curve), and production of CO_2 tracer GS2 (a) and GS3 (b) for So* = 0.05 (green curve), So* = 0.10 (pink curve), So* = 0.15 (grey curve), So* = 0.20 (yellow curve) and So* = 0.40 (blue curve).

Table 10.5 Overview of breakthrough time and migration rate between the injection well and the production well for tracer GS2 and GS3

Tracer		So* = 0.05	So* = 0.10	So* = 0.15	So* = 0.20	So* = 0.40
GS2	Breakthrough	90 days	93 days	99 days	108 days	116 days
GS3	time	70 days	72 days	77 days	69 days	74 days
GS2	Migration	8.33 ft/day	8.06 ft/day	7.58 ft/day	6.94 ft/day	6.47 ft/day
GS3	rate	10.71 ft/day	10.42 ft/day	9.74 ft/day	10.87 ft/day	10.14 ft/day

Foam generation was also compared and verified by investigating the producing gas-oil ratio (GOR) for the different residual oil sensitivity cases. Producing GOR versus time and pore volume (PV) injected has been graphed (Figure 10.20) for So* = 0.05 (green curve), So* = 0.10 (pink curve), So* = 0.15 (grey curve), So* = 0.20 (yellow curve) and So* = 0.40 (blue curve).

The average GOR was 11.03 mscf/stb for So* = 0.05, 10.45 mscf/stb for So* = 0.10, 9.87 mscf/stb for So* = 0.15, 8.78 mscf/stb for So* = 0.20, and 8.16 mscf/stb for So* = 0.40. Thus, further supporting the trend and order seen for BHP and the GS2 CO_2 tracer, with the highest tolerance to residual oil (So* = 0.40) reducing the CO_2 mobility the most.
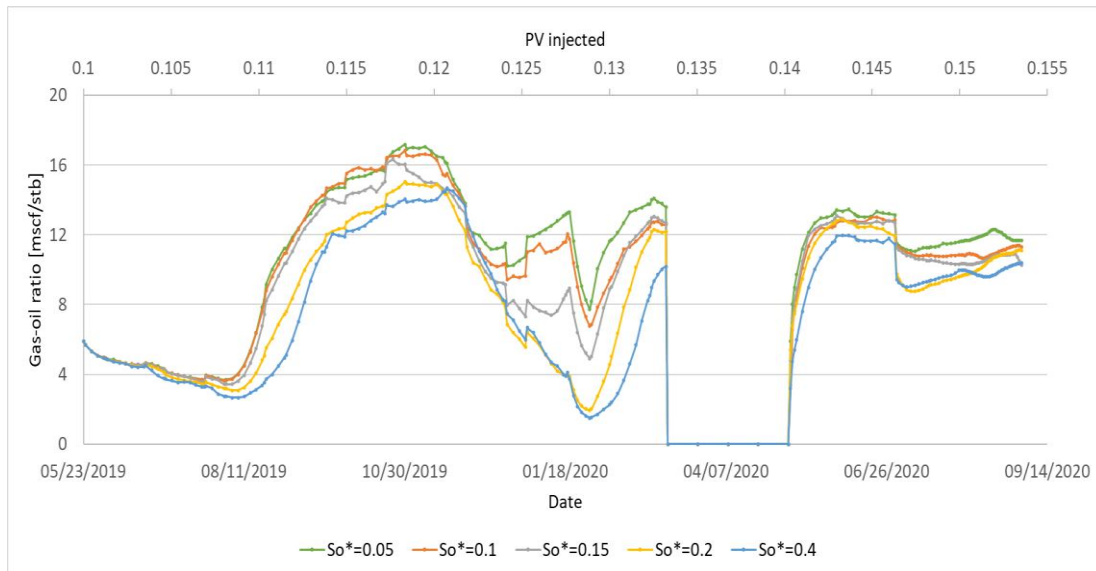
Figure 10.20 Producing gas-oil ratio (GOR) versus time and pore volume (PV) injected for production for So* = 0.05 (green curve), So* = 0.10 (pink curve), So* = 0.15 (grey curve), So* = 0.20 (yellow curve) and So* = 0.40 (blue curve).

10.5.3 Sweep Efficiency
Sweep improvement by foam was evaluated and compared for the different oil tolerances by analyzing water cut in the production well. Figure 10.16 shows the water cut versus time and pore volume (PV) injected for So* = 0.05 (green curve), So* = 0.10 (pink curve), So* = 0.15 (grey curve), So* = 0.20 (yellow curve) and So* = 0.40 (blue curve).

The average water cut was 0.909 stb/stb for So* = 0.05, 0.916 stb/stb for So* = 0.10, 0.919 stb/stb for So* = 0.15, 0.926 stb/stb for So* = 0.20, and 0.928 stb/stb for So* = 0.40. Furthering the support of the trend seen for the BHP, tracers and GOR with So* = 0.40 having a slightly better volumetric sweep, but that the overall water cut values for all sensitivities were about the same.
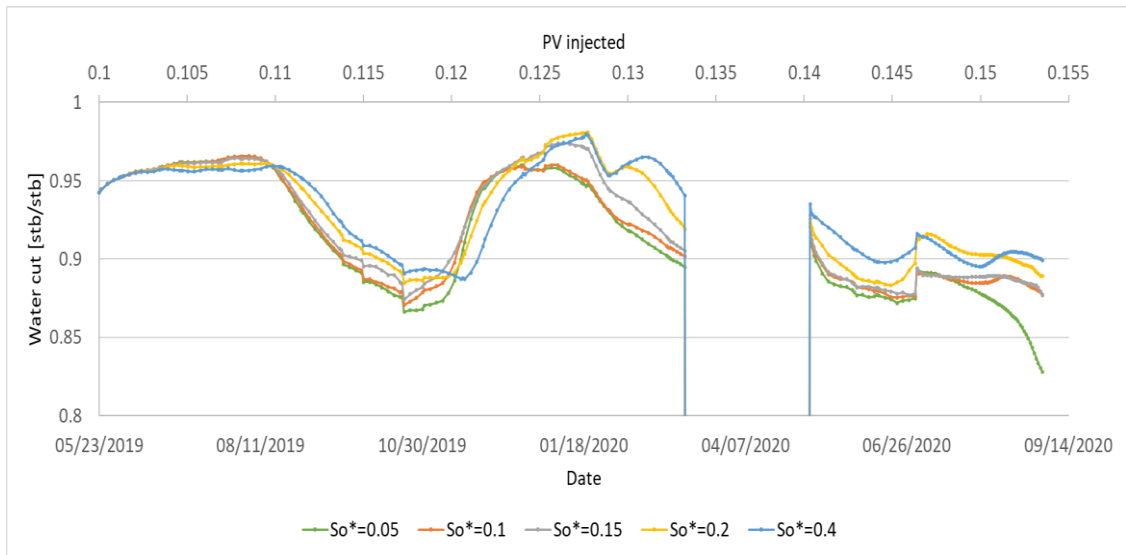
Figure 10.21 Producing water cut versus time and pore volume (PV) injected for So* = 0.05 (green curve), So* = 0.10 (pink curve), So* = 0.15 (grey curve), So* = 0.20 (yellow curve) and So* = 0.40 (blue curve).

Part IV. Conclusion and Future Work

11. Conclusion

CO_2 foam generation, strength, and stability were tested in unsteady-state core floods at reservoir conditions to determine which injection rates, surfactant concentrations and gas fractions were suitable for generating strong and stable foam. Below are the key observations/conclusions for the experimental sensitivity study:

A laboratory methodology representative of unsteady-state flow was designed and utilized for core-flooding which allowed for analyzation of unsteady state foam flow. Foam was proved to be generated in all core SAG injections.

Baseline: Foam generation was confirmed by the comparison of the baseline WAG and SAG injection. Foam was generated during cycle 4 (0.9 PV injected) for the SAG injection. The peak apparent viscosity was 2.4 cP for the baseline WAG whereas it was 146.0 cP for the SAG.

The Effect of Gas Fraction:

- A gas fraction of 0.70 generated a stronger foam, faster than the 0.60 gas fraction (12.4 cP and 2.6 cP at 1 PV injected, respectively) with a surfactant concentration of 5000 ppm and an injection rate of 4 ft/day. The 0.70 gas fraction generated a stronger foam (241.1 cP and 146.0 cP, respectively) with a higher foam stability (half-life of 0.14 and 0.09 PV injected for 0.70 and 0.60, respectively).

- A gas fraction of 0.70 generated stronger foam with less surfactant solution injected (at 0.5 PV of surfactant solution injected, 8.2 cP and 4.2 cP, respectively), with a surfactant concentration of 2500 ppm and an injection rate of 4 ft/day. It also generated a 13.6% stronger foam overall, and the stability was negligible between the two gas fractions (half-life of 0.11 and 0.10 PV injected for the 0.60 and 0.70 gas fraction, respectively).

- Foam generation were negligible in strength for the 0.60 and 0.70 gas fraction for the first five cycles with a surfactant concentration of 5000 ppm and injection rate of 8 ft/day. The overall strength was also negligible (168.1 cP and 166.4 cP, for gas fraction 0.60 and 0.70, respectively). The stability was higher for the 0.60 gas fraction (half-life of 0.18 PV injected) than it was for the 0.70 gas fraction (half-life of 0.12 PV injected) gas fraction.

The Effect of Surfactant Concentration:

- Foam was generated at about the same rate and strength for the 2500 ppm and 5000 ppm surfactant concentrations (1.4 PV injected, ~4 cP) at a gas fraction of 0.60 and an injection rate of 4 ft/day. The 2500 ppm surfactant solution generated an overall stronger foam than the 5000 ppm surfactant solution (205.3 cP and 146.0 cP, respectively). It also had a 22.2% more stable foam.

- The 5000 ppm surfactant solution generated foam faster and stronger than the 2500 ppm injection (1 PV injected, 12.3 cP and 2.7 cP, respectively) at a gas fraction of 0.70 and an injection rate of 4 ft/day. The overall difference in foam strength was negligible for the two surfactant concentrations, but the 5000 ppm surfactant concentration had a higher foam stability than the 2500 ppm surfactant concentration (half-life of 0.14 and 0.10 PV injected, respectively).

<u>The Effect of Injection Rate:</u>

- The 8 ft/day injection rate generated foam faster and stronger than the 4 ft/day injection (1.4 PV injected, 11.9 cP and 3.9 cP, respectively) with a 0.60 gas fraction and 5000 ppm surfactant concentration. The overall foam strength was 125.6% higher on average for the 8 ft/day injection, and the stability was higher (half-life of 0.18 and 0.09 PV injected for the 8 ft/day and 4 ft/day, respectively).

- The 4 ft/day injection rate generated stronger foam faster than the 8 ft/day injection (1 PV injected, 12.3 cP and 3.1 cP, respectively), with a 0.70 gas fraction and 5000 ppm surfactant concentration. The overall strength was also higher for the 4 ft/day injection than the 8 ft/day injection (241.1 cP and 166.4 cP, respectively). The 4 ft/day injection had a 14.8% longer half-life and thereby was slightly more stable.

Overall, there was uncertainty in the experimental data and/or no evident trends in the data due to the pressure fluctuations, lack of stabilization as well as the unsteady-state of the SAG floodings. Therefore, these complex systems should be evaluated further by continuing the SAG injection to evaluate when and at what value the APPV flattens and stabilizes, as well as used longer cores for flooding to reduce the effect of the pressure fluctuations on high permeability cores.

CO_2 foam mobility reduction performance was also investigated in a field-scale numerical reservoir model. The aim was to evaluate foam generation, CO_2 foam mobility reduction, and sweep efficiency of different experimentally derived foam models. In addition, the effect of residual oil on foam was evaluated numerically. The following key observations/conclusions for the numerical work were:

Overall, the numerical results showed that CO_2 mobility was reduced by foam. In addition, foam models with higher values for reference gas mobility-reduction factor (*fmmob*) generated stronger foam with a higher reduction of CO_2 mobility and an improved volumetric sweep. A higher reference oil saturation for foam collapse (*fmoil*) also resulted in stronger foam generation with a higher CO_2 mobility reduction and a better volumetric sweep.

- Foam generation was confirmed in the reservoir model by comparing the SAG injection to an identical WAG injection. The peak bottom hole pressure (BHP) was 28.1% higher for the SAG than the WAG. The effect of foam was also confirmed by the increased breakthrough time for the CO_2 tracer which broke 40 days later in the production well in the SAG case. The sweep efficiency was also improved for the SAG indicated by a 6.7% increase in water cut on average compared to the WAG.

- The experimentally derived foam model with the highest value for the reference gas mobility-reduction factor (*fmmob*), generated foam slightly faster and stronger than the other models (3.8% higher than the next), it also reduced the CO_2 mobility the most with an 84-day longer breakthrough time for the CO_2 tracer than the second. As well as increased the sweep efficiency the most (average water cut of 0.93 stb/stb).

- When accounting for shear-thinning in the near-well region for the experimentally derived foam models, the model with the highest *fmmob*, generated foam slightly faster and stronger than the other models (2% higher than the next), it also reduced the CO_2 mobility the most with a 6-day longer breakthrough time for the CO_2 tracer than the second, as well as increased the sweep efficiency the most (average water cut of 0.93 stb/stb).

-   The experimentally derived foam model combination with the highest values for *fmmob*, Combination C, generated slightly stronger foam than the combination with lower values for *fmmob*, it also reduced the CO_2 mobility and increased the volumetric sweep slightly more than the other combinations.

-   The base SAG model and foam strength were sensitive to oil saturation. Foam with a higher tolerance to oil was stronger, reduced the CO_2 mobility and increased the sweep efficiency the most. Due to low residual oil saturation in the reservoir model, the differences between each of the sensitivities was minor.

12. Future Work

The experimental and numerical work presented in this thesis was a part of an ongoing CO_2 foam field pilot project, led by the Reservoir Physics group at the Department of Physics and Technology, University of Bergen. For this thesis, the performance of different injection rates, gas fractions and surfactant concentrations were investigated. As well as evaluation of CO_2 foam mobility reduction performance regarding foam generation and strength of different laboratory derived foam models at the field-scale.

The work has provided improved understanding of unsteady-state SAG injections in cores as well as for the numerical foam sensitivity tests, but results should be further verified through additional laboratory and numerical work. The following is a list of suggestions for future work:

- Furthering the SAG injection to evaluate when and at what value the APPV flattens and stabilizes.

-Test the same procedure but with injection of surfactant solution from the first injected cycle, instead of from the third.

-Test the same method with residual oil in the system.

-Change the sensitivities further by change the sizes of the SAG slugs, testing lower concentrations of surfactants and different gas fractions.

-Use longer cores for experimental core floods to reduce the effect of pressure fluctuations on cores with high permeability.

-Find a method to automatically change between phases to get a closer match in volume for the slugs.

-Compare the numerical results to observed field data.

-Numerically test the impact of lower surfactant concentration in the SAG injection.

Part V. Nomenclature, Abbreviations, References and Appendix

Nomenclature

A Cross sectional area

C_N Conversion factor dependent upon units used

cP Centipoise

C_s Effective surfactant concentration

C_s^r Reference surfactant concentration

D Darcy

D Diameter

epcap   Parameter that captures sear-thinning behavior in the low-quality regime

epdry   Parameter controlling the abruptness of foam collapse

epoil   Parameter controlling the effect of oil saturation

e_c Exponent which controls the steepness of the transition about the point $N_c = N_c^r$

e_o Exponent which controls the steepness of the transition about the point $S_o = S_o^m$

e_s Exponent which controls the steepness of the transition about the point $C_s = C_s^r$

epsurf   Parameter controlling the effect of surfactant concentration

fmcap   Parameter set to the lowest capillary number expected in the simulation

fmdry   Water saturation in vicinity of which foam collapses

f_g Gas fraction/Foam quality

fmmob Reference gas mobility-reduction factor for foam

fmsurf   Reference surfactant concentration

fmoil   Reference high oil saturation for foam collapse

F_c Mobility reduction factor component due to gas velocity (capillary number)

F_o Mobility reduction factor component due to oil saturation

F_s Mobility reduction factor component due to surfactant concentration

ft Feet

F_w Mobility reduction factor component due to water saturation

f_w Weighting factor which controls the sharpness in the change in mobility

K Absolute permeability

K_i Effective permeability

$K_{r,foam}$ Gas relative permeability modification from foam

$K_{r,g}$ Relative permeability of CO_2

K_{ri} Relative permeability of phase i

L Length

M Residual mass

M_i Initial mass

M_r Reference mobility reduction factor

M_{rf} Mobility reduction factor

$mscf$ Million standard cubic feet

N_c Capillary number

N_c^r Reference capillary number

P Pressure

P_c Capillary pressure

P_{nw} Pressure in non-wetting phase

psi Pound-force per square inch

$psig$ Pound-force per square inch Gauge

P_w Pressure in wetting phase

Q Flow rate

q_g Gas phase rate

q_{liq} Liquid phase rate

r Radius

rb Reservoir barrels

S_i Saturation of phase i

S_o Oil saturation

S_o^m Maximum oil saturation above which the foam ceases to be effective

S_w Water saturation

S_w^1 Limiting water saturation below which the foam ceases to be effective

T Temperature

u Velocity

V_p Pore volume

V_t Total bulk volume

$wt.\%$ Weight percent

ΔM Produces mass

ΔP Differential pressure

θ Angle between fluids

σ Interfacial tension

σ_{wg} Gas-water interfacial tension

ϕ_{eff} Effective porosity

ϕ_{res} Residual porosity

ϕ_{tot} Total porosity

μ Viscosity

μ_{app} Apparent viscosity

Abbreviations

API   American Petroleum Institute gravity

APPV   Apparent viscosity

BHP   Bottom Hole Pressure

BPR   Back Pressure Regulator

CCS   Carbon Capture and Storage

CCUS   Carbon Capture, Utilization and Storage

CMC   Critical Micellar Concentration

EOR   Enhanced Oil Recovery

EoS   Equation of State

GOR   Gas-Oil Ratio

IFT   Interfacial Tension

MMP   Minimum Miscibility Pressure

MPZ   Main Pay Zone

MRF   Mobility Reduction Factor

OOIP   Original Oil In Place

ppm   Parts per million

PV   Pore Volume

ROS   Remaining Oil Saturation

ROZ   Residual Oil Zone

SAG   Surfactant Alternating Gas

SCAL   Special Core Analysis

WAG   Water Alternating Gas

References

Abidin, A., Puspasari, T., & Nugroho, W. (2012). Polymers for enhanced oil recovery technology. *Procedia Chemistry, 4*, 11-16.

Al-Wahaibi, Y. M., & Grattoni, C. A. (2008). *Mechanisms of Oil Recovery via Multi-Contact Miscible Gas Injection Process within Lensed Systems.* Paper presented at the SPE Symposium on Improved Oil Recovery.

Aladasani, A., & Bai, B. (2010). *Recent Developments and Updated Screening Criteria of Enhanced Oil Recovery Techniques.* Paper presented at the International Oil and Gas Conference and Exhibition in China.

Alagorni, A. H., Yaacob, Z. B., & Nour, A. H. (2015). An overview of oil production stages: enhanced oil recovery techniques and nitrogen injection. *International Journal of Environmental Science and Development, 6*(9), 693-701.

Alcorn, Z. P., Fernø, M., & Graue, A. (2016). *Workflow for Optimal Injection of CO2 to Enhance Oil Recovery in Mature Oil Fields: A Preliminary Study for a Field Pilot Program.* Paper presented at the SPE Bergen One Day Seminar.

Alcorn, Z. P., Føyen, T. L., Zhang, L., Karakas, M., Biswal, S. L., Hirasaki, G., & Graue, A. (2020). *CO2 Foam Field Pilot Design and Initial Results.* Paper presented at the SPE Improved Oil Recovery Conference.

Alcorn, Z. P., Fredriksen, S. B., Sharma, M., Rognmo, A. U., Føyen, T. L., Fernø, M. A., & Graue, A. (2018). *An Integrated CO2 Foam EOR Pilot Program with Combined CCUS in an Onshore Texas Heterogeneous Carbonate Field.* Paper presented at the SPE Improved Oil Recovery Conference.

Alcorn, Z. P., Fredriksen, S. B., Sharma, M., Rognmo, A. U., Føyen, T. L., Fernø, M. A., & Graue, A. (2019). An Integrated Carbon-Dioxide-Foam Enhanced-Oil-Recovery Pilot Program With Combined Carbon Capture, Utilization, and Storage in an Onshore Texas Heterogeneous Carbonate Field. *SPE Reservoir Evaluation & Engineering, 22*(04), 1449-1466. doi:10.2118/190204-pa

Anderson, W. G. (1986a). Wettability Literature Survey- Part 1: Rock/Oil/Brine Interactions and the Effects of Core Handling on Wettability. *Journal of Petroleum Technology, 38*(10), 1125-1144. doi:10.2118/13932-pa

Anderson, W. G. (1986b). Wettability Literature Survey- Part 2: Wettability Measurement. *Journal of Petroleum Technology, 38*(11), 1246-1262. doi:10.2118/13933-pa

Anderson, W. G. (1987a). Wettability Literature Survey- Part 4: Effects of Wettability on Capillary Pressure. *Journal of Petroleum Technology, 39*(10), 1283-1300. doi:10.2118/15271-pa

Anderson, W. G. (1987b). Wettability Literature Survey Part 5: The Effects of Wettability on Relative Permeability. *Journal of Petroleum Technology, 39*(11), 1453-1468. doi:10.2118/16323-pa

Barnes, K. B. (1936). *Porosity and Saturation Methods.* Paper presented at the Drilling and Production Practice.

Batycky, R., Thiele, M., Coats, K., Grindheim, A., Ponting, D., Settari, T., . . . Whitson, C. (2007). Chapter 17 - Reservoir Simulation. In *Petroleum Engineering Handbook, Vol. 5 - Reservoir Engineering and Petrophysics*.

Bikerman, J. J. (1973). Foams. Retrieved from http://books.google.com/books?id=UjpRAAAAMAAJ

Campbell, B. T., & Orr, F. M., Jr. (1985). Flow Visualization for CO2/Crude-Oil Displacements. *Society of Petroleum Engineers Journal, 25*(05), 665-678. doi:10.2118/11958-pa

Chambers, D. J. (1994). Foams for Well Stimulation. In *Foams: Fundamentals and Applications in the Petroleum Industry* (Vol. 242, pp. 355-404): American Chemical Society.

Chang, S.-H., & Grigg, R. B. (1999). Effects of Foam Quality and Flow Rate on CO2-Foam Behavior at Reservoir Temperature and Pressure. *SPE Reservoir Evaluation & Engineering, 2*(03), 248-254. doi:10.2118/56856-pa

Chou, S. (1991). *Conditions for generating foam in porous media.* Paper presented at the SPE Annual Technical Conference and Exhibition.

Chou, S., Vasicek, S., Pisio, D., Jasek, D., & Goodgame, J. (1992). *CO2 foam field trial at north ward-estes.* Paper presented at the SPE annual technical conference and exhibition.

Craig, F. F. (1971). *The reservoir engineering aspects of waterflooding* (Vol. 3): HL Doherty Memorial Fund of AIME New York.

Dellinger, S. E., Patton, J. T., & Holbrook, S. T. (1984). CO2 Mobility Control. *Society of Petroleum Engineers Journal, 24*(02), 191-196. doi:10.2118/9808-pa

Derikvand, Z., & Riazi, M. (2016). Experimental Investigation of a Novel Foam Formulation to Improve Foam Quality. *Journal of Molecular Liquids, 224*, 1311-1318. doi:10.1016/j.molliq.2016.10.119

Dooley, J. J., Dahowski, R. T., & Davidson, C. L. (2010). *CO2-driven Enhanced Oil Recovery as a Stepping Stone to What?* Retrieved from

El-Dessouky, H. T. (2002). Fundamentals of salt water desalination. Amsterdam: Elsevier.

Enick, R. M., Olsen, D. K., Ammer, J. R., & Schuller, W. (2012). *Mobility and Conformance Control for CO2 EOR via Thickeners, Foams, and Gels -- A Literature Review of 40 Years of Research and Pilot Tests*. Paper presented at the SPE Improved Oil Recovery Symposium, Tulsa, Oklahoma, USA. https://doi.org/10.2118/154122-MS

Ertekin, T., Abou-Kassem, J., & King, G. (2001). *Basic Applied Reservoir Simulation* (Vol. 7).

Falls, A. H., Hirasaki, G. J., Patzek, T. W., Gauglitz, D. A., Miller, D. D., & Ratulowski, T. (1988). Development of a Mechanistic Foam Simulator: The Population Balance and Generation by Snap-Off. *SPE Reservoir Engineering, 3*(03), 884-892. doi:10.2118/14961-pa

Farajzadeh, R., Andrianov, A., Krastev, R., Hirasaki, G. J., & Rossen, W. R. (2012). Foam-oil interaction in porous media: implications for foam assisted enhanced oil recovery. *Adv Colloid Interface Sci, 183-184*, 1-13. doi:10.1016/j.cis.2012.07.002

Farajzadeh, R., Andrianov, A., & Zitha, P. L. J. (2010). Investigation of Immiscible and Miscible Foam for Enhancing Oil Recovery. *Industrial & Engineering Chemistry Research, 49*(4), 1910-1919. doi:10.1021/ie901109d

Freund, P., Bachu, S., Simbeck, D., Thambimuthu, K., Gupta, M. (2005). Properties of CO2 and carbon-based fuels. In *Carbon Dioxide Capture and Storage*. New York: Cambridge University Press.

Friedmann, F., & Jensen, J. A. (1986). *Some Parameters Influencing the Formation and Propagation of Foams in Porous Media.* Paper presented at the SPE California Regional Meeting.

Gauglitz, P. A., Friedmann, F., Kam, S. I., & Rossen, W. R. (2002). *Foam Generation in Porous Media.* Paper presented at the SPE/DOE Improved Oil Recovery Symposium.

Gozalpour, F., Ren, S., & Tohidi, B. (2005). CO2 EOR and storage in oil reservoir. *Oil & Gas Science and Technology-revue De L Institut Francais Du Petrole - OIL GAS SCI TECHNOL, 60*, 537-546. doi:10.2516/ogst:2005036

Green, D. W., & Willhite, G. P. (1998). *Enhanced oil recovery*. Richardson, TX: Henry L. Doherty Memorial Fund of AIME, Society of Petroleum Engineers.

Grogan, A. T., & Pinczewski, W. V. (1987). The Role of Molecular Diffusion Processes in Tertiary CO2 Flooding. *Journal of Petroleum Technology, 39*(05), 591-602. doi:10.2118/12706-pa

Hanssen, J. E., & Dalland, M. (1994). Gas-Blocking Foams. In *Foams: Fundamentals and Applications in the Petroleum Industry* (Vol. 242, pp. 319-353): American Chemical Society.

Hanssen, J. E., Holt, T., & Surguchev, L. M. (1994). *Foam Processes: An Assessment of Their Potential in North Sea Reservoirs Based on a Critical Evaluation of Current Field Experience.* Paper presented at the SPE/DOE Improved Oil Recovery Symposium.

Heller, J. P. (1994). CO2 Foams in Enhanced Oil Recovery. In *Foams: Fundamentals and Applications in the Petroleum Industry* (Vol. 242, pp. 201-234): American Chemical Society.

Heller, J. P., & Kuntamukkula, M. S. (1987). Critical review of the foam rheology literature. *Industrial & Engineering Chemistry Research, 26*(2), 318-325. doi:10.1021/ie00062a023

Heller, J. P., Lien, C. L., & Kuntamukkula, M. S. (1985). Foamlike Dispersions for Mobility Control in CO2 Floods. *Society of Petroleum Engineers Journal, 25*(04), 603-613. doi:10.2118/11233-pa

Hirasaki, G. J., & Lawson, J. B. (1985). Mechanisms of Foam Flow in Porous Media: Apparent Viscosity in Smooth Capillaries. *Society of Petroleum Engineers Journal, 25*(02), 176-190. doi:10.2118/12129-pa

Holm, L. W. (1986). Miscibility and Miscible Displacement. *Journal of Petroleum Technology, 38*(08), 817-818. doi:10.2118/15794-pa

Holm, L. W., & Josendal, V. A. (1974). Mechanisms of Oil Displacement By Carbon Dioxide. *Journal of Petroleum Technology, 26*(12), 1427-1438. doi:10.2118/4736-pa

Honarpour, M. M., Nagarajan, N. R., Grijalba, A. C., Valle, M., & Adesoye, K. (2010). *Rock-Fluid Characterization for Miscible CO2 Injection: Residual Oil Zone, Seminole Field, Permian Basin.* Paper presented at the SPE Annual Technical Conference and Exhibition.

Hubbert, M. K. (1956). Darcy's Law and the Field Equations of the Flow of Underground Fluids. *Transactions of the AIME, 207*(01), 222-239. doi:10.2118/749-g

IEA. (2021a). *Global Energy Review 2021, IEA, Paris*. Retrieved from https://www.iea.org/reports/global-energy-review-2021

IEA. (2021b). *Net Zero by 2050, IEA, Paris*. Retrieved from https://www.iea.org/reports/net-zero-by-2050

IPCC. (2005). *IPCC Special Report on Carbon Dioxide Capture and Storage. Prepared by Working Group III of the Intergovernmental Panel on Climate Change [Metz, B., O. Davidson, H. C. de Coninck, M. Loos, and L. A. Meyer (eds.)]*. Cambridge, United Kingdom and New York, NY, USA: Cambridge University Press.

Jenkins, R. J. (1966). Accuracy Of Porosity Determinations. *The Log Analyst, 7*(02).

Jian, G., Puerto, M. C., Wehowsky, A., Dong, P., Johnston, K. P., Hirasaki, G. J., & Biswal, S. L. (2016). Static Adsorption of an Ethoxylated Nonionic Surfactant on Carbonate Minerals. *Langmuir, 32*(40), 10244-10252. doi:10.1021/acs.langmuir.6b01975

Kahrobaei, S., Vincent-Bonnieu, S., & Farajzadeh, R. (2017). Experimental Study of Hysteresis behavior of Foam Generation in Porous Media. *Scientific Reports, 7*(1), 8986. doi:10.1038/s41598-017-09589-0

Karakas, M., Alcorn, Z. P., & Graue, A. (2020). *CO2 Foam Field Pilot Monitoring Using Transient Pressure Measurements.* Paper presented at the SPE Annual Technical Conference and Exhibition.

Kent Thomas, L. (2007). Reservoir Simulation Applications. In *Petroleum Engineering Handbook, Vol. 5 - Reservoir Engineering and Petrophysics*.

Kovscek, A. R., & Radke, C. J. (1993). Fundamentals of foam transport in porous media. In: ACS Publications.

Kristiansen, S. M. (2018). *Field Pilot Injection Strategies for CO2 Foam EOR in a Layered Heterogeneous Carbonate Reservoir.* University of Bergen, Bergen.

Lake, L. W. (2010). *Enhanced oil recovery*. Richardson, Tex: Society of Petroleum Engineers.

Lake, L. W., Johns, R., Rossen, B., & Pope, G. A. (2014). Fundamentals of enhanced oil recovery.

Lee, S., & Kam, S. I. (2013). Chapter 2 - Enhanced Oil Recovery by Using CO2 Foams: Fundamentals and Field Applications. In J. J. Sheng (Ed.), *Enhanced Oil Recovery Field Case Studies* (pp. 23-61). Boston: Gulf Professional Publishing.

Lemmon, E., McLinden, M., & Friend, D. (2012). *Thermophysical Properties of Fluid Systems in NIST Chemistry WebBook, NIST Standard Reference Database Number 69, Eds. PJ Linstrom and WG Mallard, National Institute of Standards and Technology, Gaithersburg MD, 20899. In.*

Lien, J. R. (2004). PTEK211 - Grunnleggende reservoarfysikk (Kjerneanalyse og logging). In. Bergen: University of Bergen.

Mangalsingh, D., & Jagai, T. (1996). *A Laboratory Investigation of the Carbon Dioxide Immiscible Process.* Paper presented at the SPE Latin America/Caribbean Petroleum Engineering Conference.

Martin, F., Heller, J., Weiss, W., Tsau, J.-S., Zornes, D., Sugg, L., . . . Kim, J. (1992). *CO2-foam field verification pilot test at EVGSAU injection project phase I: project planning and initial results.* Paper presented at the SPE/DOE Enhanced Oil Recovery Symposium.

Martin, F., Stevens, J., & Harpole, K. (1995). CO 2-Foam Field Test at the East Vacuum Grayburg/San Andres Unit. *SPE Reservoir Engineering, 10*(04), 266-272.

Matthews, C. S. (1989). Carbon Dioxide Flooding. In *Enhanced oil recovery, II: Processes and operations*: Elsevier.

Merchant, D. H. (2010). *Life Beyond 80: A look at Conventional WAG Recovery Beyond 80% HCPV Injection in CO2 Tertiary Floods.* Paper presented at the SPE International Conference on CO2 Capture, Storage, and Utilization.

Metcalfe, R. S., & Yarborough, L. (1979). The Effect of Phase Equilibria on the CO2 Displacement Mechanism. *Society of Petroleum Engineers Journal, 19*(04), 242-252. doi:10.2118/7061-pa

Mirazimi, S., Rostami, B., Ghazanfari, M.-H., & Khosravi, M. (2017). Water film rupture in blocked oil recovery by gas injection: Experimental and modeling study. *Chemical Engineering Science, 161*, 288-298. doi:https://doi.org/10.1016/j.ces.2016.12.043

Mo, D., Yu, J., Liu, N., & Lee, R. (2012). *Study of the Effect of Different Factors on Nanoparticle-Stablized CO2 Foam for Mobility Control.* Paper presented at the SPE Annual Technical Conference and Exhibition.

Muller, T., & Lake, L. W. (1991). Theoretical Study of Water Blocking in Miscible Flooding. *SPE Reservoir Engineering, 6*(04), 445-451. doi:10.2118/20206-pa

Ocampo, A., Restrepo, A., Cifuentes, H., Hester, J., Orozco, N., Gil, C., . . . Gonzalez, C. (2013). *Successful Foam EOR Pilot in a Mature Volatile Oil Reservoir Under Miscible Gas Injection.* Paper presented at the International Petroleum Technology Conference.

Peksa, A. E., Wolf, K.-H. A., & Zitha, P. L. (2015). Bentheimer sandstone revisited for experimental purposes. *Marine and Petroleum Geology, 67*, 701-719.

Perkins, T. K., & Johnston, O. C. (1963). A Review of Diffusion and Dispersion in Porous Media. *Society of Petroleum Engineers Journal, 3*(01), 70-84. doi:10.2118/480-pa

Ragab, A., & Mansour, E. M. (2021). Enhanced Oil Recovery: Chemical Flooding. In *Geophysics and Ocean Waves Studies*: IntechOpen.

Ramirez, W. F., Fathi, Z., & Cagnol, J. L. (1984). Optimal Injection Policies for Enhanced Oil Recovery: Part 1 Theory and Computational Strategies. *Society of Petroleum Engineers Journal, 24*(03), 328-332. doi:10.2118/11285-pa

Ransohoff, T. C., & Radke, C. J. (1988). Mechanisms of Foam Generation in Glass-Bead Packs. *SPE Reservoir Engineering, 3*(02), 573-585. doi:10.2118/15441-PA

Rathmell, J. J., Stalkup, F. I., & Hassinger, R. C. (1971). *A Laboratory Investigation of Miscible Displacement by Carbon Dioxide.* Paper presented at the Fall Meeting of the Society of Petroleum Engineers of AIME.

Rognmo, A. U. (2019). *CO2-Foams for Enhanced Oil Recovery and CO2 Storage.* (Dissertation for the Degree of Philosophiae Doctor (PhD)). University of Bergen, Bergen.

Romero-Zerón, L. (2012). *Introduction to enhanced oil recovery (EOR) processes and bioremediation of oil-contaminated sites*: BoD–Books on Demand.

Rosman, A., & Kam, S. I. (2009). Modeling Foam-diversion Process Using Three-phase Fractional Flow Analysis in a Layered System. *Energy Sources, Part A: Recovery, Utilization, and Environmental Effects, 31*(11), 936-955. doi:10.1080/15567030701752875

Ross, S., & McBain, J. W. (1944). Inhibition of Foaming in Solvents Containing Known Foamers. *Industrial & Engineering Chemistry, 36*(6), 570-573. doi:10.1021/ie50414a019

Rossen, W. R. (1996). Foams in enhanced oil recovery. *Foams: theory, measurements and applications, 57*, 413-464.

Satter, A. (2008). *Practical enhanced reservoir engineering : assisted with simulation software*.

Savitzky, A., & Golay, M. J. E. (1964). Smoothing and Differentiation of Data by Simplified Least Squares Procedures. *Analytical Chemistry, 36*(8), 1627-1639. doi:10.1021/ac60214a047

Schafer, R. W. (2011). What Is a Savitzky-Golay Filter? *IEEE Signal Processing Magazine, 28*(4), 111-117. doi:10.1109/MSP.2011.941097

Schlumberger. (2007). *ECLIPSE Blackoil Reservoir Simulation Training and Exercise Guide*: Schlumberger.

Schlumberger. (2016). *ECLIPSE Industry-Reference Reservoir Simulator Technical Description*: Schlumberger.

Schramm, L. L. (1994). Foam Sensitivity to Crude Oil in Porous Media. In *Foams: Fundamentals and Applications in the Petroleum Industry* (Vol. 242, pp. 165-197): American Chemical Society.

Schramm, L. L., & Wassmuth, F. (1994). Foams: Basic Principles. In *Foams: Fundamentals and Applications in the Petroleum Industry* (Vol. 242, pp. 3-45): American Chemical Society.

Sharma, M. (2017). East Seminole Simulation Study. Technical report, National IOR Centre

of Norway at the University of Stavanger.

Sharma, M. (2019). *CO2 Mobility Control with Foam for Enhanced Oil Recovery and Associated Storage.* University of Stavanger, Stavanger.

Sharma, M., Alcorn, Z. P., Fredriksen, S., Fernø, M., & Graue, A. (2017). Numerical Modelling Study for Designing CO2-Foam Field Pilot. *2017*(1), 1-15. doi:https://doi.org/10.3997/2214-4609.201700339

Sheng, J. J. (2010). *Modern Chemical Enhanced Oil Recovery : Theory and Practice.* Oxford, UNITED STATES: Elsevier Science & Technology.

Sheng, J. J. (2013). Chapter 11 - Foams and Their Applications in Enhancing Oil Recovery. In J. J. Sheng (Ed.), *Enhanced Oil Recovery Field Case Studies* (pp. 251-280). Boston: Gulf Professional Publishing.

Skarestad, M., & Skauge, A. (2012). *PTEK213 Reservoarteknikk* Bergen, Norway: University of Bergen.

Skjæveland, S. M., & Kleppe, J. (1992). *SPOR monograph: recent advances in improved oil recovery methods for North Sea sandstone reservoirs*. Stavanger: Norwegian Petroleum Directorate.

Skjelsvik, E. B. (2018). *Synergy of Nanoparticles and Surfactants for CO2 Foam Enhanced Oil Recovery and CO2 Storage in Carbonates* (MSc). University of Bergen, Bergen.

Soyke, A. (2020). *Combining Nanoparticles and Surfactants to Stabilize CO2 Foam for CCUS.* (MSc). University of Bergen, Bergen.

Stalkup, F. I. (1970). Displacement of oil by Solvent at High Water Saturation. *Society of Petroleum Engineers Journal, 10*(04), 337-348. doi:10.2118/2419-pa

Stephenson, D. J., Graham, A. G., & Luhning, R. W. (1993). Mobility control experience in the Joffre Viking miscible CO2 flood. *SPE Reservoir Engineering, 8*(03), 183-188.

Stone, H. L. (1982). *Vertical, Conformance In An Alternating Water-Miscible Gas Flood.* Paper presented at the SPE Annual Technical Conference and Exhibition.

Suffridge, F. E., Raterman, K. T., & Russell, G. C. (1989). *Foam Performance Under Reservoir Conditions.* Paper presented at the SPE Annual Technical Conference and Exhibition.

Suhling, M., Arigovindan, M., Hunziker, P., & Unser, M. (2004). Multiresolution moment filters: theory and applications. *IEEE Transactions on Image Processing, 13*(4), 484-495. doi:10.1109/TIP.2003.819859

Svorstøl, I., Vassenden, F., & Mannhardt, K. (1996). *Laboratory Studies for Design of a Foam Pilot in the Snorre Field.* Paper presented at the SPE/DOE Improved Oil Recovery Symposium.

Veeningen, D., Zitha, P. L. J., & van Kruijsdijk, C. P. J. W. (1997). *Understanding Foam Flow Physics: The Role of Permeability.* Paper presented at the SPE European Formation Damage Conference.

Warner, H. R. (2015). *The reservoir engineering aspects of waterflooding* (2nd. ed. Vol. vol. 3). Richardson, Tex: Society of Petroleum Engineers SPE.

Wasan, D. T., Koczo, K., & Nikolov, A. D. (1994). Mechanisms of Aqueous Foam Stability and Antifoaming Action with and without Oil. In *Foams: Fundamentals and Applications in the Petroleum Industry* (Vol. 242, pp. 47-114): American Chemical Society.

Yellig, W. F., & Metcalfe, R. S. (1980). Determination and Prediction of CO2 Minimum Miscibility Pressures (includes associated paper 8876). *Journal of Petroleum Technology, 32*(01), 160-168. doi:10.2118/7477-pa

Zekri, A., & Jerbi, K. (2002). Economic Evaluation of Enhanced Oil Recovery. *Oil & Gas Science and Technology-revue De L Institut Francais Du Petrole - OIL GAS SCI TECHNOL, 57*, 259-267. doi:10.2516/ogst:2002018

Zhang, D., & Song, J. (2014). Mechanisms for Geological Carbon Sequestration. *Procedia IUTAM, 10*, 319-327. doi:https://doi.org/10.1016/j.piutam.2014.01.027

Zolotuchin, A. B., & Ursin, J.-R. (2000). *Introduction to petroleum reservoir engineering*. Kristiansand: Høyskoleforl.

Appendix

A. Core Analysis

A.1 Core Saturation

The following procedure was conducted with the purpose of completely saturating the core-plug used in the experimental work with brine. The dry core was placed in a glass container and connected to a vacuum system where the air pressure was lowered to approximately 600 mTorr. The pressure was measured until it stabilized using a vacuum gauge connected to the system. The brine in the glass holder placed on top of the glass cylinder was also vacuumed before being released into the glass cylinder with the core. The glass container was filled until it covered the core completely before being left completely sealed off over night to ensure full saturation. Figure A.1 illustrates the air evacuation apparatus.
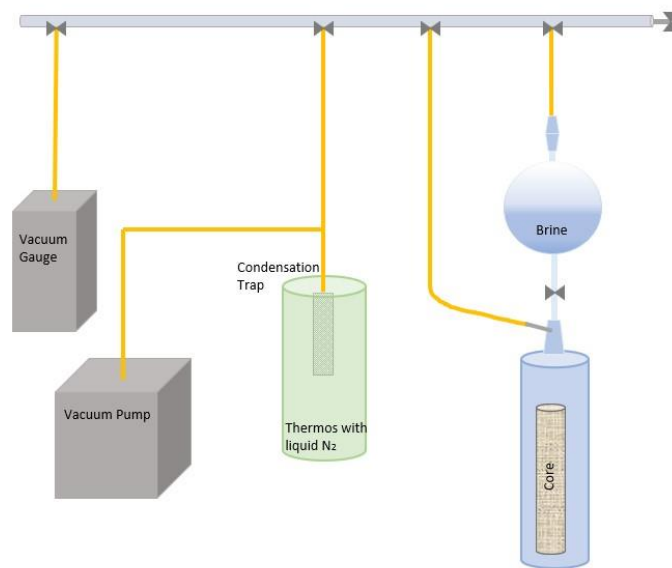
Figure A.1 Air evacuation apparatus used for core saturation.

A.2 Porosity and Permeability Measurements

The porosity of the core was measured using the saturation method. This involves weighing the porous media when completely dry and then after being saturated with brine. The weight difference corresponds to the mass of brine in the core (Barnes, 1936). When dividing the mass difference of the core by the density of the brine, ρ, the pore volume can be calculated by using the equation listed below:

$$V_p = \frac{m_{sat} - m_{dry}}{\rho} \qquad A1$$

Measurements of the absolute permeability of the core plug was done by injecting brine at a constant rate through the core until the differential pressure stabilized. The permeability, K, was calculated using Equation 2.5. The differential pressure was measured at different rates to minimize measurement uncertainties. Brine was injected with a Quizix QX6000 pump and the differential pressure was measured using a differential pressure transmitter. The setup is illustrated in figure 5.1.

B. Permeability Values

Calculation of apparent viscosity is a central measurement of foam strength and is highly dependent on the measured permeability of the porous media. Therefore, between each SAG injection, the effective permeability was measured to check for residual fluid saturation in the core. The

permeability was measured with the highest value being 2.68 D and the lowest value being 1.71 D. The variation in permeability has no pattern and it is assumed that this variation is caused by residual surfactant solution and/or CO_2 in the core. Although, the core was cleaned thoroughly as described in section 5.3.1, there might still have been residual CO_2 trapped in the pores. Trapping can be caused by capillary pressure and dissolution with brine in the porous media (Zhang & Song, 2014).

Table B.1 Measured absolute permeability

Measurement	Permeability [D]	Uncertainty permeability [D]
1	2.00	0.05
2	1.88	0.01
3	1.71	0.02
4	2.25	0.01
5	2.09	0.01
6	2.25	0.01
7	1.90	0.01
8	2.67	0.08
9	2.18	0.05
10	2.68	0.02
11	1.82	0.01

C. Uncertainties

The uncertainty in the laboratory experiments is caused by two sources: uncertainty in instruments, e.g. scales, or uncertainty in methods, e.g. measurement of porosity. The total uncertainty in a measured value depends on the uncertainty of the instruments used in the measurement. The instrumental uncertainties are found in Table C.1. The following equations were used for the uncertainty calculations during the experimental work.

Addition and Subtraction

For several independent variables *x, y, z…, i*, added or subtracted for calculating value *R*, the uncertainty of *R*, is expressed as S_R and is calculated based on the uncertainty of each variable.

$$S_R = \sqrt{\left(\frac{\delta R}{\delta x}S_x\right)^2 + \left(\frac{\delta R}{\delta y}S_y\right)^2 + \left(\frac{\delta R}{\delta z}S_z\right)^2 + \cdots + \left(\frac{\delta R}{\delta i}S_i\right)^2} \qquad C1$$

Multiplication and Division

When calculating value *R*, as the product or quotient of a set variables $a^2x, b^2y, c^2z, …, n^2i$, where *x, y, z,…,i* are variables with an uncertainty $S_x, S_y, S_z, …, S_i$ and $a^2, b^2, c^2, …, n^2$ are constants, the uncertainty S_R can be calculated by:

$$S_R = \sqrt{\left(a\frac{S_x}{x}\right)^2 + \left(b\frac{S_y}{y}\right)^2 + \left(c\frac{S_z}{z}\right)^2 + \cdots + \left(n\frac{S_i}{i}\right)^2} \qquad\qquad C2$$

Standard Deviation

The variations in a set of data, S, can be calculated by the following equation:

$$S = \sqrt{\frac{1}{N-1}\sum_{i=1}^{N}(x_i - \bar{x})^2} \qquad\qquad C3$$

Where N is number if sample values, x_i and $\bar{x}$ is the sample mean.

Table C.1 Instrumental uncertainties for equipment used during the experimental work

Instrument	Parameter	Uncertainty
Scale	Mass [g]	± 0.01
Caliper	Length [cm]	± 0.002
Ruler	Length [cm]	± 0.1
Measuring cylinder	Volume [mL]	± 0.1
ESI pressure transducer	Pressure [% of full range]	± 0.1
Differential pressure transducer	Pressure [% of full range]	± 0.075
EL-FLOW mass flow controller	Rate [mL/h]	± 0.02

D. Python Smoothing Plot

```
1  import pandas as pd
2  import matplotlib as plt
3  from matplotlib import gridspec
4  from matplotlib import figure, pyplot
5  import seaborn as sns
6  from matplotlib import pyplot as plt
7  import numpy as np
8  from numpy import trapz
9  from collections import *
10
11 from scipy.signal import savgol_filter
12
13 fig = pyplot.figure( figsize=(12,8))
14
15 ax1 = fig.subplots()
16
17 sns.set_style('ticks')
18
19 ax2 = ax1.twinx()
20 ax2.set_ylim(0,1)
21 ax2.tick_params(labelcolor='black', labelsize=15, width=1.2)
22
23
24 def plot(file, col, lab): #file = file name, col = color, lab = label
25     df = pd.read_csv(file)
26     df.dropna(inplace=True)
27     smoothed_APPV = savgol_filter(df['korrigert'], window_length = 1001,
28 polyorder = 3)
```

```
29     df['smoothed_APPV'] = smoothed_APPV
30
31
32     df.plot(x = 'PV inj', y = 'smoothed_APPV', label = lab, ax = ax1,
33 color = col, xlim = (0,5))
34
35     ax1.tick_params(labelcolor='black', labelsize=15, width=1.2)
36     ax1.margins(-0.8)
37     ax1.set_ylabel("Apparent Viscosity [cP]", size = 20)
38     ax1.set_xlabel('Pore Volume Injected', size = 20)
39     #ax1.set_xticks(np.arange(0.0,7,1))
40     ax1.set_yticks(np.arange(0,2,0.1))
41     ax1.legend(loc = 1, prop={'size':15},frameon = False)
42
43     sns.set_palette('Paired')
44     df.to_excel('new_sag60.2_smooth.xlsx') #new file : PV inj,
45 Appv_original, Appv_new
46
47


   name1 = 'Sag60.csv'
   file = plot(name1, 'C1', 'SAG_all')
```

E. Numerical Cross-sectional Model

RUNSPEC

--NOSIM

NOECHO

TITLE

HIST CO2 INJECTION AND PILOT WITH POST PILOT INJ

FIELD

OIL

GAS

WATER

COMPS

6 /

COMPW

2 /

START

1 JAN 2018 /

DIMENS

75 1 54 /

WELLDIMS

5 60 4 5 /

UNIFOUT

UNIFIN

MESSAGES

6* 2* 1000000 1000000 /

UDQDIMS

10 10 5* 10 /

UDQPARAM

4* /

TABDIMS

3 /

--*******************

GRID

TOPS

75*5360 /

DX

4050*10 /

DY

4050*50 /

DZ

75*7.45

225*3

225*2.44

75*2.49

150*2.36

75*15.71

375*2.94

150*1.83

75*0.08

150*2.88

150*2.86

75*0.03

150*1.86

75*8.03

150*2.89

150*1.93

75*5.22

150*2.67

150*2.26

150*2.64

75*11.14

300*2.99

75*19.47

450*2.6

75*0.79

75*0.64

75*0.74

75*2.17

/

PORO

75*0

225*0.056

225*0.062

75*0.113

150*0.074

75*0

375*0.109

150*0.188

75*0.11

150*0.132

150*0.094

75*0.075

150*0.103

75*0

150*0.109

150*0.089

75*0

150*0.104

150*0.129

150*0.044

75*0

300*0.065

75*0

450*0.106

75*0

75*0.016

75*0

75*0.023

/

PERMX

75*0

225*0.1

225*0.1

75*21.6

150*2.5

75*0

375*1.9

150*117.8

75*0.7

150*15.9

150*1.8

75*0.9

150*0.1

75*0

150*4.7

150*13.8

75*0

150*4.3

150*8.7

150*0

75*0

300*1.1

75*0

450*5.5

75*0

75*1.6

75*0

75*1.3

/

COPY

PERMX PERMY /

PERMX PERMZ /

/

MULTIPLY

PERMZ 0.16 1 75 1 1   1   1 /

PERMZ 0.6   1 75 1 1   2   4 /

PERMZ 0.16 1 75 1 1   5   7 /

PERMZ 0.6   1 75 1 1   8   8 /

PERMZ 0.6   1 75 1 1   9 10 /

PERMZ 0.16 1 75 1 1 11 11 /

PERMZ 0.6   1 75 1 1 12 16 /

PERMZ 0.6   1 75 1 1 17 18 /

PERMZ 0.16 1 75 1 1 19 19 /

PERMZ 0.6   1 75 1 1 20 21 /

PERMZ 0.6   1 75 1 1 22 23 /

PERMZ 0.16 1 75 1 1 24 24 /

PERMZ 0.6   1 75 1 1 25 26 /

PERMZ 0.16 1 75 1 1 27 27 /

PERMZ 0.6   1 75 1 1 28 29 /

PERMZ 0.6   1 75 1 1 30 31 /

PERMZ 0.16 1 75 1 1 32 32 /

PERMZ 0.6   1 75 1 1 33 34 /

PERMZ 0.6   1 75 1 1 35 36 /

PERMZ 0.6   1 75 1 1 37 38 /

PERMZ 0.16 1 75 1 1 39 39 /

PERMZ 0.6   1 75 1 1 40 43 /

PERMZ 0.16 1 75 1 1 44 44 /

PERMZ 0.6   1 75 1 1 45 50 /

PERMZ 0.16 1 75 1 1 51 51 /

PERMZ 0.6   1 75 1 1 52 52 /

PERMZ 0.16 1 75 1 1 53 53 /

PERMZ 0.6   1 75 1 1 54 54 /

/

GRIDFILE

0 1 /

INIT

--MINPV

--1 /

--MINDZNET

--0.05 /

--RPTGRID

--DX DY DZ PORO PORV /

--*********************

EDIT

--*********************

PROPS

NCOMPS

6 /

EOS

PR /

RTEMP

104 /

STCOND

60   14.696 /

CNAMES

CO2 N2C1 H2SC2C3 C4C5C6 PC1 PC2 /

TCRIT

547.6 340.6 610.9 827.1 1374.3 1324.7 /

PCRIT

1069.9 663.8 706.3 509.8 323.0 248.9 /

VCRIT

1.506 1.583 2.625 4.719 8.746 19.607 /

MW

44.01 16.29 36.19 70.01 148.24 374.21 /

ACF

0.2250 0.0086 0.1202 0.2278 0.4133 0.9618 /

OMEGAA

6*0.45723553 /

OMEGAB

6*0.077796074 /

SSHIFT

6*0 /

TBOIL

350.5 206.2 395.1 552.2 866.1 1368.1 /

PARACHOR

78.0 76.3 122.3 217.1 416.4 865.8 /

BIC

0.1029

0.1285 0.0029

0.1156 0.0136 0.0040

0.1001 0.0327 0.0164 0.0044

0.1146 0.0685 0.0447 0.0229 0.0075

/

PEDERSEN

PEDTUNER

0.5120 1.1240 0.9456 0.5832 0.01062 /

DENSITY

1* 62.4 1* /

PVTW

3000 1* 1.6E-6 0.75 /

ROCK

3000 10E-6 /

STONE

SWFN

-- W -> O

0.100   0.000   0

0.101   0.000   0

0.200   0.001   0

0.235   0.007   0

0.270   0.028   0

0.305   0.063   0

0.340   0.112   0

0.375   0.175   0

0.410   0.252   0

0.445   0.343   0

0.480   0.448   0

0.515   0.567   0

0.550   0.700   0

1.000   1.000   0 /

/

/

SGFN

0.000   0.000   0

0.001 0.000 0

0.050 0.000 0

0.100 0.063 0

0.135 0.106 0

0.170 0.150 0

0.205 0.194 0

0.240 0.238 0

0.275 0.281 0

0.310 0.325 0

0.345 0.369 0

0.380 0.413 0

0.415 0.456 0

0.450 0.500 0

0.583 0.667 0

0.717 0.833 0

0.850 1.000 0 /

/

/

-- SORG=5%

SOF3

0.000 0.000 0.000

0.050 0.000 0.000

0.183 0.000 0.157

0.317 0.000 0.314

0.450 0.000 0.471

0.485 0.0003 0.512

0.520 0.003 0.553

0.555 0.009 0.594

0.590 0.021 0.635

0.625 0.041 0.676

```
0.660   0.071   0.718

0.695   0.113   0.759

0.730   0.169   0.800

0.765   0.240   0.841

0.800   0.329   0.882

0.899   0.700   0.999

0.900   1.000   1.000  /

/

/


--SOR

--0.05 /

--0.05 /


TRACER

GS1 CO2 /

GS2 CO2 /

GS3 CO2 /

WT1 WATER /

WT2 SURFACT /

/


------------------------------------------


WNAMES

WATER SURFACT /


MWW

18.015 18.015 / SURF PROPERTIES = WATER PROPERTIES (ACTS AS TRACER)


PREFW
```

2360 2360 /

DREFW

62.4 62.4 /

CREFW

1.6E-6 1.6E-6 /

VREFW

0.75 0.75

0   0   /

CWTYPE

1* SURFF /

FOAMFRM

0 /

630 /

1200 /

FOAMFSW

0.32 500 /

0.27 100 /

0.22 25 /

FOAMFCN

7.8E-07 0.65 /

7.8E-07 0.65 /

7.8E-07 0.65 /

FOAMFSC

-- lb/stb, ,lb/stb,

0.35 1 0.175 0.20 /

0.35 1 0.175 0.20 /

0.35 1 0.175 0.20 /

FOAMFST

--lb/stb,lbf/in.

0   0.0001616

3.54 0.0000418 /

0   0.0001616

3.54 0.0000418 /

0   0.0001616

3.54 0.0000418 /

FOAMFSO

0.28 1 /

0.28 1 /

0.28 1 /

--*********************

REGIONS

SATNUM

1 74*1

1 74*1 1 74*1 1 74*1

1 74*1 1 74*1 1 74*1

1 74*2

1 74*1 1 74*1

1 74*1

1 74*1 1 74*1 1 74*1 1 74*1 1 74*1

1 74*3 1 74*3

1 74*1

1 74*2 1 74*2

1 74*1 1 74*1

1 74*1

1 74*1 1 74*1

1 74*1

1 74*1 1 74*1

1 74*2 1 74*2

1 74*1

1 74*1 1 74*1

1 74*1 1 74*1

1 74*1 1 74*1

1 74*1

1 74*1 1 74*1 1 74*1 1 74*1

1 74*1

1 74*1 1 74*1 1 74*1 1 74*1 1 74*1 1 74*1

1 74*1

1 74*1

1 74*1

1 74*1

/

--*********************

SOLUTION

PRESSURE

4050*3200 /

---SWAT FROM 1 JAN 2018

INCLUDE

SWAT_XSECTION.INC /

SGAS

4050*0 /

ZMF

4050*0.0247 4050*0.2516 4050*0.1863

4050*0.1277 4050*0.2723 4050*0.1374 /

DATUM

5360 /

RPTRST

'BASIC=2' FOAM FOAMMOB FOAMCNM DENG DENO DENW VGAS VOIL VWAT FLORES PRESSURE SGAS SOIL SWAT AMF XMF YMF ZMF GS1 /

TBLKGS1

4050*0 /

TBLKWT1

4050*0 /

TBLKGS2

4050*0 /

TBLKWT2

4050*0 /

WMF

4050*1

4050*0

/

```
--*********************

SUMMARY

RPTONLY

INCLUDE

'SUMMARYFOAM.INC' /

PERFORMA

COPR

L25 /

/

CGPR

L25 /

/

CWPR

L25 /

/

CWCT

L25 /

/

CGOR

L25 /

/
```

CGIR

L14G /

L14W /

/

WTPRGS1

/

WTPTGS1

/

WTIRGS1

/

WTITGS1

/

CTPRGS1

L25 /

/

CTIRGS1

L25 /

/

WUSCTPT

/

WUSCTPR

/

WTPRWT1

/

WTPTWT1

/

WTIRWT1

/

WTITWT1

/

CTPRWT1

L25 /

/

CTIRWT1

L25 /

/

WTPRGS2

/

WTPTGS2

/

WTIRGS2

/

WTITGS2

/

CTPRGS2

L25 /

/

CTIRGS2

L25 /

/

WTPRWT2

/

WTPTWT2

/

WTIRWT2

/

WTITWT2

/

CTPRWT2

L25 /

/

CTIRWT2

L25 /

/

WTPRGS3

/

WTPTGS3

/

WTIRGS3

/

WTITGS3

/

CTPRGS3

L25 /

/

CTIRGS3

L25 /

CTIRGS3

L25 /

/

--*********************

SCHEDULE

--TUNING

--1 7 0.5 0.5 2 /

--/

--/

RPTRST

'BASIC=2' FOAM FOAMMOB FOAMCNM DENG DENO DENW VGAS VOIL VWAT FLORES PRESSURE
SGAS SOIL SWAT AMF XMF YMF ZMF GS1 /

WELSPECS

L25   PROD 75 1 5360 OIL /

L14W WINJ   1 1 5360 WATER /

L14G GINJ   1 1 5360 GAS /

/

COMPDAT

L25 2* 1 54 OPEN 2* .725 1* 0 1* Z /

L14W 2* 1 54 OPEN 2* .725 1* 0 1* Z /

L14G 2* 1 54 OPEN 2* .725 1* 0 1* Z /

/

--###

WCONINJE

L14W WATER SHUT RESV 1*   0 4000 /

L14G GAS   OPEN RESV 1* 18.9 4000 /

/

WCONPROD

L25 OPEN RESV 4* 17.7 1000 /

/

--###

WELLSTRE

SOLVENT 1 0 0 0 0 0 /

/

WELLSTRW

WATONLY 1.0 0.0 /

WATSURF 0.995 0.005 / 0.5 WT%

/

WINJGAS

L14G STREAM SOLVENT /

/

WINJW

L14W STREAM WATONLY /

/

--WPIMULT

--L14G 0.002 /

--L14W 0.008 /

--/

DATES

2 JAN 2018 /

9 JAN 2018 /

/

UDQ

DEFINE WUSCTPT WTPTGS1 L25 / WTITGS1 L14G /

DEFINE WUSCTPR WTPRGS1 L25 / WTITGS1 L14G /

/

WTRACER

L14G GS1 0.0015 /

/

DATES

10 JAN 2018 /

/

WTRACER

L14G GS1 0 /

/

DATES

11 JAN 2018 /

15 JAN 2018 /

 1 FEB 2018 /

15 FEB 2018 /

28 FEB 2018 /

/

--############# L14: WATER INJ ############

WCONINJE

L14W WATER OPEN RESV 1*   17 4000 /

L14G GAS   SHUT RESV 1*   0 4000 /

/

WCONPROD

L25 OPEN RESV 4* 10.8 1000 /

/

--###

DATES
 1 MAR 2018 /
 2 MAR 2018 /
/

--############# L14: WATER INJ (LOWER RATE) ############
WCONINJE

L14W WATER OPEN RESV 1* 9.5 4000 /

L14G GAS   SHUT RESV 1* 0   4000 /

/

--###

DATES
 3 MAR 2018 /
 5 MAR 2018 /
15 MAR 2018 /
 1 APR 2018 /
15 APR 2018 /
 1 MAY 2018 /
15 MAY 2018 /
 1 JUN 2018 /
15 JUN 2018 /
 1 JUL 2018 /
18 JUL 2018 /

/

--############# L14: HIST CO2 INJ (JULY 19 2018 - NOV 20 2018) #############
WCONINJE
L14W WATER SHUT RESV 1*   0   4000 /
L14G GAS   OPEN RESV 1*   18.9 4000 /
/

WCONPROD
L25 OPEN RESV 4* 17.7 1000 /
/
--###

DATES
 19 JUL 2018 /
 2 AUG 2018 /
 3 AUG 2018 /
 5 AUG 2018 /
10 AUG 2018 /
 1 SEP 2018 /
 1 OCT 2018 /
 1 NOV 2018 /
 20 NOV 2018 /
/

--############# L14: HIST WATER INJ (22 NOV 2018 - 22 DEC 2018) #############
WCONINJE
L14W WATER OPEN RESV 1*   17 4000 /
L14G GAS   SHUT RESV 1*   0   4000 /
/

UDQ

DEFINE WUSCTPT WTPTWT1 L25 / WTITWT1 L14W /

DEFINE WUSCTPR WTPRWT1 L25 / WTITWT1 L14W /

/

WTRACER

L14W WT1 1 /

/

DATES

21 NOV 2018 /

/

WTRACER

L14W WT1 0 /

/

DATES

22 NOV 2018 /

/

DATES

 25 NOV 2018 /

 30 NOV 2018 /

 1 DEC 2018 /

 22 DEC 2018 /

/

--############# L14: HIST WATER INJ (22 DEC 2018 - 4 APRIL 2019 LOW RATE) #############

WCONINJE

```
L14W  WATER  OPEN  RESV  1*  9.5  4000 /
L14G  GAS   SHUT  RESV  1*  0   4000 /
/
```

DATES
```
 23 DEC 2018 /
 1  JAN 2019 /
 1  FEB 2019 /
 28 FEB 2019 /
 1  MAR 2019 /
 30 MAR 2019 /
 4  APR 2019 /
/
```

```
--############# L14: HIST WATER INJ (4 APRIL 2019 - 22 APR 2019 HIGH RATE) #############
WCONINJE
L14W  WATER  OPEN  RESV  1*   20  4000 /
L14G  GAS   SHUT  RESV  1*  0   4000 /
/
```

DATES
```
 5 APR 2019 /
 12 APR 2019 /
 21 APR 2019 /
/
```

```
--############# L14: HIST CO2 INJ (22 APR 2019 - 21 MAY 2019) ##########
WCONINJE
```

L14W WATER SHUT RESV 1* 0   4000 /

L14G GAS   OPEN RESV 1* 9.5 4000 /

/

DATES

 22 APR 2019 /

 24 APR 2019 /

 1 MAY 2019 /

 21 MAY 2019 /

/

--############## L14: HIST WATER INJ (1000 BBL INJ BEFORE PILOT MAY 22 2019) #############

WCONINJE

L14W WATER OPEN RESV 1* 18 4000 /

L14G GAS   SHUT RESV 1* 0   4000 /

/

DATES

22 MAY 2019 /

/

--############## L14: PILOT SAG 10 DAYS SURF, 20 DAYS CO2 (x6) ##########

--########## HM RUN: OBS RATE CONVER = 0.027 BASED UPON XSECTION PV #########

-- ##### CYCLE 1 10 DAYS SURF #####---WATER TRACER 2--

WCONHIST

---------CTRL OIL   WATER GAS

L25 OPEN LRAT 0.70 9.23   24.70 /

/

WCONINJH

L14W WATER OPEN 9.83 3646 6* RATE /

L14G GAS   SHUT 0   4000 6* RATE /

/

WELLSTRE

SOLVENT 1 0 0 0 0 0 /

/

WELLSTRW

WATONLY 1.0 0.0 /

WATSURF 0.995 0.005 / 0.5 WT%

/

WINJW

L14W STREAM WATSURF /

/

WINJGAS

L14G STREAM SOLVENT /

/

UDQ

DEFINE WUSCTPT WTPTWT2 L25 / WTITWT2 L14W /

DEFINE WUSCTPR WTPRWT2 L25 / WTITWT2 L14W /

/

WTRACER

L14W WT2 1 /

/

DATES

23 MAY 2019 /

/

WTRACER

L14W WT2 0 /

/

DATES

24 MAY 2019 /

/

TSTEP

3*3 /

-- ##### 20 DAYS CO2 ##### --CO2 TRACER 2--

WCONHIST

---------CTRL OIL   WATER   GAS

L25 OPEN LRAT 0.57   9.28   21.70 /

/

WCONINJH

L14W WATER SHUT 9.83 3646 6* RATE /

L14G GAS   OPEN 23.86 3574 6* RATE /

/

UDQ

DEFINE WUSCTPT WTPTGS2 L25 / WTITGS2 L14G /

DEFINE WUSCTPR WTPRGS2 L25 / WTITGS2 L14G /

/

WTRACER

L14G GS2 0.0015 /

/

TSTEP

1 /

WTRACER

L14G GS2 0 /

/

TSTEP

1 /

TSTEP

6*3 /

-- ##### CYCLE 2 10 DAYS SURF #####

WCONHIST

---------CTRL OIL   WATER GAS

L25 OPEN LRAT 0.49 8.08   18.27 /

/

WCONINJH

```
L14W  WATER  OPEN  11.61  3661 6* RATE /
L14G  GAS    SHUT  0   4000 6* RATE /
/


TSTEP
1 3*3 /


-- ##### 20 DAYS CO2 #####

WCONHIST
---------CTRL OIL   WATER  GAS
L25 OPEN LRAT 0.55  8.87   19.05 /
/


WCONINJH
L14W  WATER  SHUT  9.83  3646 6* RATE /
L14G  GAS    OPEN  23.34  3581 6* RATE /
/


TSTEP
1 6*3 1 /


-- ##### CYCLE 3 10 DAYS SURF #####

WCONHIST
---------CTRL OIL   WATER  GAS
L25 OPEN LRAT 0.44  6.47   16.09 /
/
```

WCONINJH

L14W WATER OPEN 9.85 3656 6* RATE /

L14G GAS   SHUT 0 4000 6* RATE /

/

TSTEP

1 3*3 /

-- ##### 20 DAYS CO2 #####

WCONHIST

---------CTRL OIL   WATER GAS

L25 OPEN LRAT 0.48 6.17   15.32 /

/

WCONINJH

L14W WATER SHUT 9.83 3646 6* RATE /

L14G GAS   OPEN 22.39 3559 6* RATE /

/

TSTEP

1 6*3 1 /

-- ##### CYCLE 4 10 DAYS SURF #####

WCONHIST

---------CTRL OIL   WATER GAS

L25 OPEN LRAT 0.54 5.11   17.10 /

/

WCONINJH

L14W WATER OPEN 8.825 3663 6* RATE /

L14G GAS   SHUT 0 4000 6* RATE /

/

TSTEP

1 3*3 /

-- ##### 20 DAYS CO2 #####

WCONHIST

---------CTRL OIL   WATER GAS

L25 OPEN LRAT 0.49 5.65   10.16 /

/

WCONINJH

L14W WATER SHUT   9.83 3646 6* RATE /

L14G GAS   OPEN   23.33 3544 6* RATE /

/

TSTEP

1 6*3 1 /

-- ##### CYCLE 5 10 DAYS SURF #####

WCONHIST

---------CTRL OIL   WATER GAS

L25 OPEN LRAT 0.31 4.93   10.36 /

/

WCONINJH

L14W WATER OPEN 10.13 3637 6* RATE /

L14G GAS   SHUT 0 4000 6* RATE /

/

TSTEP

1 3*3 /

-- ##### 20 DAYS CO2 #####

WCONHIST

---------CTRL OIL   WATER GAS

L25 OPEN LRAT 0.34 3.82   8.82 /

/

WCONINJH

L14W WATER SHUT 9.83 3646 6* RATE /

L14G GAS   OPEN 20.69 3469 6* RATE /

/

TSTEP

1 6*3 1 /

-- ##### CYCLE 6 10 DAYS SURF #####

WCONHIST

```
---------CTRL OIL   WATER  GAS
L25 OPEN LRAT 0.25  2.80   6.12 /
/


WCONINJH
L14W  WATER  OPEN   11.05 3641 6* RATE /
L14G  GAS   SHUT  0    4000 6* RATE /
/



TSTEP
1 3*3 /


-- ##### 20 DAYS CO2 #####

WCONHIST
---------CTRL OIL   WATER  GAS
L25 OPEN LRAT 0.27  3.12   6.53 /
/

WCONINJH
L14W  WATER  SHUT  9.83  3646 6* RATE /
L14G  GAS   OPEN  23.22 3560 6* RATE /
/

TSTEP
1 6*3 1 /


-- ##### CYCLE 7 10 DAYS SURF #####
```

WCONHIST

---------CTRL OIL   WATER GAS

L25 OPEN LRAT 0.28 2.95   6.87 /

/

WCONINJH

L14W WATER OPEN   9.64 3667 6* RATE /

L14G GAS   SHUT 0   4000 6* RATE /

/

TSTEP

1 3*3 /

-- ##### 20 DAYS CO2 #####

WCONHIST

---------CTRL OIL   WATER GAS

L25 OPEN LRAT 0.37 3.59   8.37 /

/

WCONINJH

L14W WATER SHUT 9.83 3646 6* RATE /

L14G GAS   OPEN 21.55 3505 6* RATE /

/

TSTEP

1 6*3 1 /

-- ##### CYCLE 8 10 DAYS SURF #####

WCONHIST
---------CTRL OIL   WATER GAS
L25 OPEN LRAT 0.48 4.34   10.67 /
/

WCONINJH
L14W WATER OPEN 11.25 3552 6* RATE /
L14G GAS   SHUT 0   4000 6* RATE /
/

TSTEP
1 3*3 /

-- ##### 20 DAYS CO2 #####

WCONHIST
---------CTRL OIL   WATER GAS
L25 OPEN LRAT 0.23 3.60   7.70 /
/

WCONINJH
L14W WATER SHUT 9.83 3646 6* RATE /
L14G GAS   OPEN 23.12 3378 6* RATE /
/

TSTEP
1 6*3 1 /

-- ##### NO INJECTION PERIOD 22 DAYS (23 FEB - 14 MAR 2020) #####

WCONHIST

---------CTRL OIL   WATER GAS

L25 OPEN LRAT 0.325 3.15   7.75 /

/

WCONINJH

L14W WATER SHUT   0   2953 6* RATE /

L14G GAS   SHUT   0   4000 6* RATE /

/

TSTEP

1 1 5*2 /

-- ##### CYCLE 9 10 DAYS SURF #####

WCONHIST

---------CTRL OIL   WATER GAS

L25 OPEN LRAT 0.34 3.39   8.72 /

/

WCONINJH

L14W WATER OPEN 8.10 3292 6* RATE /

L14G GAS   SHUT   0   4000 6* RATE /

/

TSTEP

1 3*3 /

-- ##### 20 DAYS CO2 (ASSUMED - NO DATA) #####

WCONHIST

---------CTRL OIL   WATER GAS

L25 OPEN LRAT 0.35 3.60   8.70 /

/

WCONINJH

L14W WATER SHUT 9.83 3646 6* RATE /

L14G GAS   OPEN 23.34 3218 6* RATE /

/

TSTEP

1 6*3 1 /

-- ##### CYCLE 10 - 7 DAYS SURF #####

WCONHIST

---------CTRL OIL   WATER GAS

L25 OPEN LRAT 0.34 3.39   8.72 /

/

WCONINJH

L14W WATER OPEN 8.10 3292 6* RATE /

L14G GAS   SHUT 0   4000 6* RATE /

/

TSTEP

1 1 3*2 /

--## FIELD SHUT-DOWN 25 APRIL - 24 JUN 2020 ##--

WCONHIST

---------CTRL OIL   WATER GAS

L25 SHUT LRAT 0.34 3.39   8.72 /

/

WCONINJH

L14W WATER SHUT 8.10 3292 6* RATE /

L14G GAS   SHUT   0   4000 6* RATE /

/

TSTEP

1 2*15 2*15 /

-- ## RESTART WITH 3 DAYS OF SURF INJECTION TO FINISH 10TH SLUG ## --

WCONHIST

---------CTRL OIL   WATER GAS

L25 OPEN LRAT 0.34 3.39   8.72 /

/

WCONINJH

L14W WATER OPEN 8.10 3292 6* RATE /

L14G GAS SHUT 0 4000 6* RATE /

/

TSTEP

1 1 1 /

-- ##### 20 DAYS CO2 (ASSUMED - NO DATA) #####

WCONHIST

---------CTRL OIL WATER GAS

L25 OPEN LRAT 0.35 3.60 8.70 /

/

WCONINJH

L14W WATER SHUT 9.83 3646 6* RATE /

L14G GAS OPEN 23.34 3218 6* RATE /

/

TSTEP

1 6*3 1 /

-- ##### CYCLE 11 - 10 DAYS SURF #####

WCONHIST

---------CTRL OIL WATER GAS

L25 OPEN LRAT 0.34 3.39 8.72 /

/

WCONINJH

151

L14W WATER OPEN 8.10 3292 6* RATE /

L14G GAS   SHUT 0   4000 6* RATE /

/

TSTEP

1 3*3 /

-- ##### 20 DAYS CO2 (ASSUMED - NO DATA) #####

WCONHIST

---------CTRL OIL   WATER GAS

L25 OPEN LRAT 0.35 3.60   8.70 /

/

WCONINJH

L14W WATER SHUT 9.83 3646 6* RATE /

L14G GAS   OPEN 23.34 3218 6* RATE /

/

UDQ

DEFINE WUSCTPT WTPTGS3 L25 / WTITGS3 L14G /

DEFINE WUSCTPR WTPRGS3 L25 / WTITGS3 L14G /

/

WTRACER

L14G GS3 0.0015 /

/

TSTEP

```
1 /


WTRACER
L14G GS3 0 /
/


TSTEP
1 /



TSTEP
6*3 /


--############# POST PILOT ##### --


--############# L25: VRR - 1 ##############


WCONPROD
L25  OPEN  RESV  4*  17.7  1000  /
/


WINJW
L14W STREAM WATONLY /
/


--## 14 DAYS WATER ##--
WCONINJH
L14W  WATER  OPEN  9.83  3346 6* RATE /
L14G  GAS    SHUT 23.34  3218 6* RATE /
/
```

TSTEP

1 1 7*2 /

--## 14 DAYS CO2 ##--

WCONINJH

L14W WATER SHUT 9.83 3346 6* RATE /

L14G GAS   OPEN 23.34 3218 6* RATE /

/

TSTEP

1 1 7*2 /

--## 30 DAYS WATER ##--

WCONINJH

L14W WATER OPEN 9.83 3346 6* RATE /

L14G GAS   SHUT 23.34 3218 6* RATE /

/

TSTEP

1 30*1 /

END